Study on Gas Diffusion Layer and Cell Design for Performance Improvement of Polymer Electrolyte Fuel Cells

A Doctoral Thesis

Presented to

Integrated Graduate School of

Medicine, Engineering, and Agricultural Science

University of Yamanashi

March 2024

Tatsuya Inoue

Contents

Chapter 1 General Introduction

1-1. Background

Recent years, there has been increasing social interest in solving environmental problems such as global warming caused by carbon dioxide emissions, and in ensuring energy security by breaking away from dependence on limited natural gas and fossil fuel resources.[1] Among the automobile industry, a paradigm shift is upcoming by the change of energy sources from internal combustion-engine vehicles (ICE) with fossil fuels such as gasoline, diesel oil, and natural gas, to vehicles with new energy sources, in order to reduce the environmental impact by pollutants and prevent resource depletion.[2,3] On the other hand, electric vehicles are equipped with lithium-ion batteries for a power source, and there are remaining issues in technical aspect such as increasing the cruising range by increasing the energy density of the lithium-ion batteries, and shortening the charging speed of the battery. In addition, there are remaining issues among the infrastructure, such as expanding the spread of electric power infrastructure that enables high-speed charging and securing power generation facilities to meet the rising demand for electricity.[4] For these reasons, some believe that a complete replacement with internal combustion engine vehicles is difficult, or that technological development in a long-term plan is essential.[5,6]

Hydrogen has recently been receiving attention as a next-generation fuel, which can be used as a combustion energy source to generate turbine power, or as an electrochemical energy source to generate electric power via reaction with oxygen in a fuel cell.[7] In the case of mobility applications, fuel cell vehicles (FCVs) have been developed for decades by many researchers.[8] The first FCV of NECAR1 was produced by Daimler in 1994,[8] and the first commercial FCV of Mirai was released by Toyota in 2015.[9] As FCVs were

introduced to the market, the number of hydrogen stations installed was also gradually increasing.[10] There were 553 hydrogen stations worldwide at the end of 2020, 159 in Japan.[11]

A notable advantage of hydrogen as an energy carrier is its high energy density per weight and volume.[12] Another advantage is that hydrogen can be stored in various storage types, such as liquid, compressed gas, or metal hydrate, depending on each application. Table 1-1 shows the power density per weight and volume in various storage types of hydrogen, with references data of gasoline and lithium-ion battery. The energy density per weight of hydrogen is more than twice that of gasoline and more than 100 times that of lithium-ion batteries, except the metal hydrate storage. Since hydrogen is the lightest atm, the energy density per volume in raw hydrogen gas is quite small. When hydrogen is stored in high-pressure cylinder of 700atm, or liquid hydrogen or metal hydrate, energy densities per volume of hydrogen are 3 times or more larger than that of a lithium-ion battery.

On the other hand, metal hydrate has the disadvantage of its heavy weight and requirement for heating or cooling treatment of the cylinder to store or discharge hydrogen for each,[13] while liquid hydrogen requires tough temperature control to keep below 20K.[14] From these technical challenges, high pressure cylinders with 700 atm are currently applied in commercial FCVs.[15] In the case of high-pressure cylinder, to prevent the explosion of the cylinder and hydrogen leakage, dedicated cylinder with hybrid materials, such as carbon fiber and resin or metal have been developed. These complexed cylinders decrease the energy density per weight of hydrogen, but it was still 10 times or more higher than that in lithium-ion battery, in the case of Toyota Mirai.[16] As a result of the advantage in energy density, FCVs achieved a range of 700 to 800 km for a single

Table 1-1. Energy density per weight and volume of hydrogen with various storage type

Energy source	Hydrogen ratio wt%	Hydrogen ratio / g cm^{-3}	Energy density / J g^{-1}	Energy density / J cm^{-3}
Hydrogen (Normal gas)	100	8.9×10^{-5}	143,000	13
Hydrogen (250 atm)	100	0.017	143,000	2,430
Hydrogen (700 atm)	100	0.037	143,000	5330
Hydrogen (Liquid at 20 K)	100	0.070	143,000	10,010
Metal Hydrate (MgH_2)	7.6	0.110	10,870	15,730
Gasoline	-	-	49,000	34,600
Lithium-ion battery	-	-	~700	~1,800

fuel charge, which is equivalent to those of conventional ICVs, as demonstrated by the Toyota Mirai,[9] the Honda Clarity,[17] and the Hyundai NEXO.[18]

However, there are still challenges for FCVs to achieve other metrics that would be competitive with those for ICVs, including further improvements in power density and durability, as well as cost reduction. From the "Technology Development Roadmap of Fuel Cells for FCV," published in 2017 by the New Energy and Industrial Technology Development Organization (NEDO) of Japan, to realize FCV mass production by 2040, a power density of 9.0 kW/L, which is about 3 times higher than the present value, and a system cost of 2,000 yen/kW FC, which is 1/5 of the present value, are required.[19]

1-2. Principal of fuel cell and challenges for performance improvement

A fuel cell is defined as a device to generate electric energy from chemical reactions of fuels. [20] The basic structure of a fuel cell is centered around a liquid or solid electrolyte, with a cathode as a positive electrode and an anode as a negative electrode on both sides. Fuel such as hydrogen or methanol is supplied to the anode to cause an hydrogen oxidation reaction (HOR), while oxygen is supplied to the cathode to cause an oxygen reduction reaction (ORR). In the case of fuel cell type that protons are the carrier, such as Polymer electrolyte fuel cells, equations of HOR and ORR are shown below.

HOR at anode:

$$H_2 \rightarrow 2H^+ + 2e^- \quad (1\text{-}1)$$

ORR at cathode:

$$\frac{1}{2}O_2 + 2H^+ + 2e^- \rightarrow H_2O \quad (1\text{-}2)$$

Charges are generated at the anode and diffuse to the cathode through external electrical circuits, while protons are generated at the anode or ions generated at the cathode diffuse to the opposite electrode through the electrolyte. As a result, the entire fuel cell has a simple reaction formula in which hydrogen and oxygen react to produce water, as shown below.

$$H_2 + \frac{1}{2}O_2 \rightarrow H_2O \quad (1\text{-}3)$$

Fuel cells are classified into many types depending on the electrolyte and carrier (protons or ions).[20] Table 1-2 lists shows the characteristics of four major types of fuel cells: alkaline fuel cells (AFCs), phosphoric acid fuel cells (PAFCs), solid oxide fuel cells (SOFCs), and polymer electrolyte fuel cells (PEFCs).

AFCs has been developed for space applications since the 1960s, like PEFCs described below. AFCs operate at relatively low temperatures and have high efficiency. On the other

Table 1-2. Types and characteristics of fuel cells

Type	Alkaline Fuel Cell (AFC)	Phosphoric Acid Fuel Cell (PAFC)	Solid Oxide Fuel Cell (SOFC)	Polymer Electrolyte Fuel Cell (PEFC)
Electrolyte	Kalium hydroxide solution	Phosphoric acid solution	Stabilized zirconia plate	Polymer ion exchange membrane
Carrier	OH^-	H^+	O^{2-}	H^+
Operating Temperature	50~150˚C	190~200 ˚C	600~1000˚C	80~120 ˚C
Efficiency (HHV)	60%	35~42%	40~65%	30~40%
Efficiency (LHV)	70%	39~46%	44~72%	33~44%

hand, there is a problem in that the alkaline electrolyte is easily degraded by carbon dioxide which is contained in hydrogen and air. Therefore, the application of AFCs is limited by use of pure hydrogen and pure oxygen currently.

PAFCs have an acidic electrolyte, so they are more resistant to CO_2 than alkaline types, and because they operate at relatively high temperatures, the cooling system is simple and it is easy to use waste heat for cogeneration. On the other hand, there is a problem in that cell components are easily corroded due to both high temperature operation and the strong acidity of phosphoric acid. Therefore, it is necessary to achieve both durability improvement and cost reduction of materials. PAFCs are currently developed as on-site co-generation system of 50 to 500 kW[21,22].

SOFCs have the advantage of being highly efficiency and no requirement for expensive catalysts such as platinum for HOR and ORR such as PAFCs and PEFCs because of its high temperature operation close to 1000°C. However, when applied to automobiles, the high temperature operation offers a long time to start and stop of vehicles, and ceramic electrolytes such as yttria-stabilized zirconia (YSZ) are so fragile that is easily broken

during mechanical shock and vibration from the road running. In 2016, Nissan announced a range extender FCEV equipped with SOFC, but it has not been put into practical use yet.[23]

PEFCs, although have lower efficiency than other fuel cells as showed in table 1-2, they operate at relatively low temperatures and are easy to downsize and increase power density, so it has attracted attention as a power source for stationary devices, mobile devices, and automobiles, and progress has been made in its developments and practical applications.[20,22,24,25]

Figure 1-1 shows the schematic diagram of a PEFC. Hydrogen and oxygen supplied from the outside are distributed evenly within the plane of the cell through the anode and cathode separators, respectively. Separators are generally made of graphitized conductive carbons or metal such as stainless steel or titanium,[26,27] with flow channels formed on the surface by precise machining processing. Hydrogen and oxygen supplied through the separator reach the anode and cathode catalyst layers, respectively, through the gas diffusion layer (GDL). GDL is mainly composed of carbon fibers and contains pores with diameters of several tens to hundreds of micrometers. To reduce the electrical contact resistance at the interface between GDL and the catalyst layer, which is mainly composed of carbon black supporting catalyst metals such as Pt, a microporous layer (MPL) is often formed on the GDL surface in contact side with the catalyst layer by deposition of carbon black.[28] The MPL is also effective for discharging liquid water from the MEA to channels by capillary force. Hydrogen supplied to the anode catalyst layer is separated to protons and electrons as HOR supported by the catalyst activity. Electrons diffuse to cathode catalyst layer through GDLs, separators and electric cables outside, while protons diffuse to cathode catalyst layer through polymer electrolyte in the catalyst layer and the

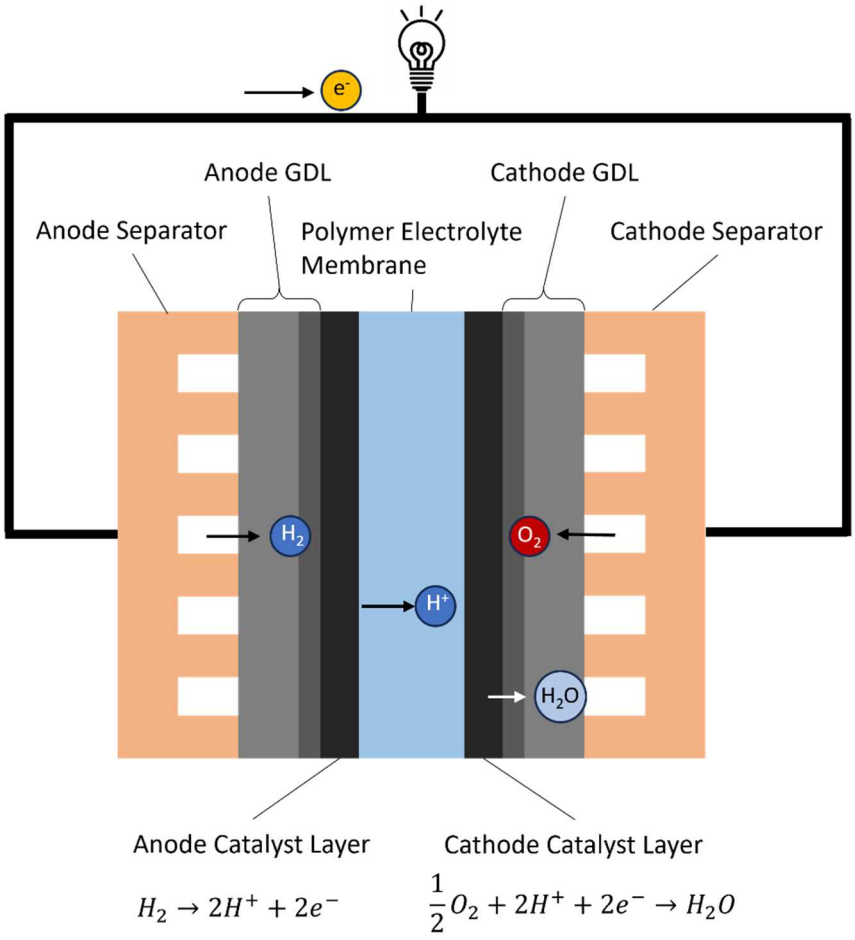

Figure 1-1. Schematic diagram of the PEFC

membrane. For the electrolyte membrane that separates the anode and cathode catalyst layers, perfluorosulfonic acid polymers such as Nafion from Chemours are generally used.[29] In cathode catalyst layer, supplied oxygen and protons and electrons causes ORR and generate water around the three phases interface which consist of a catalyst particle, a polymer electrolyte and gas phase.

The theoretical voltage of a PEFC is 1.23 V, but the actual voltage of PEFCs is limited about 1.0 V because of several factors for voltage decrease which are so called Nernst loss.[29] When the load current from a PEFC increased, the voltage loss increases depending on the current density.[30,31] The voltage loss is generally classified to three overvoltages as shown in figure 1-2: the activation overvoltage, the resistance overvoltage and the

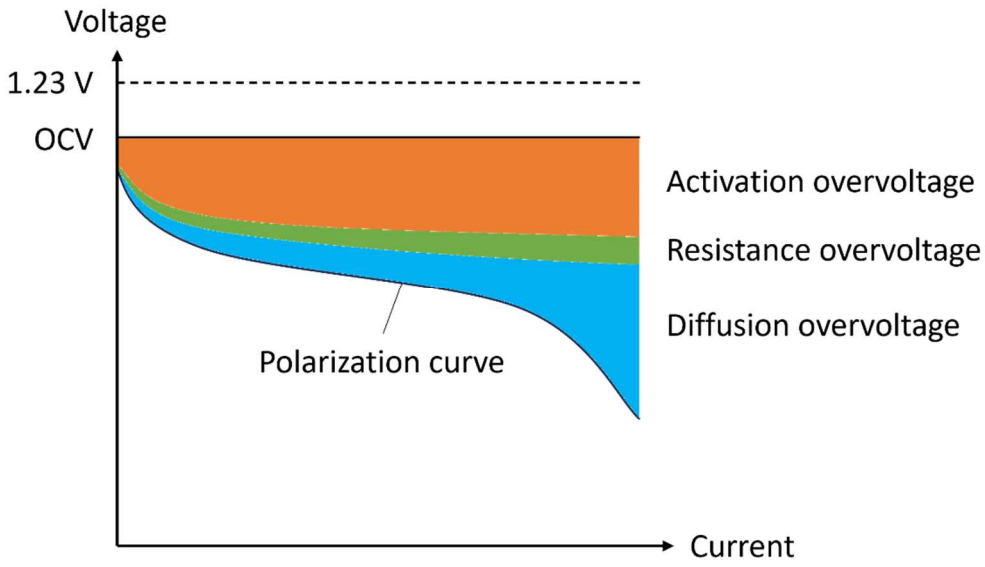

Figure 1-2. Polarization curve and overvoltage of a PEFC

diffusion overvoltage.

The activation overvoltage is caused by the energy loss on both anode and cathode reaction, and energy loss by cathode ORR is generally larger than anode HOR. The activation overvoltage accounts for the highest ratio in total voltage drop especially in lower current density. To decrease the activation overvoltage, many researchers have tried to enhance the activity of catalyst, for example, micronizing and high dispersion in carbon support of platinum nano-particle, and developing platinum alloy catalyst such as platinum-cobalt.

The resistance overvoltage is caused by the energy loss in both protons and electrons diffusion. The energy loss in electrons diffusion depends on the conductivity of cell materials such as the separator and the GDL, as well as the contact resistances at heterogeneous interface between the separator and the GDL, the GDL and the catalyst layer. The energy loss in protons diffusion depends on the conductivity of polymer electrolyte contained in both the catalyst layer and the membrane. Since protons diffuse as H_3O^+ in the polymer electrolyte, the membrane and the catalyst layer should contain a

level of water contents for protons diffuse sufficiently.

The diffusion overvoltage is caused by energy losses during supplied hydrogen and oxygen diffuse to the catalyst layer in anode and cathode respectively. When the current density increases, the consumption of hydrogen and oxygen also increase. Oxygen is generally supplied to cathode as a mixed gas with nitrogen by air compressor, so the partial pressure of oxygen is lower than nitrogen and it causes the increase of the diffusion overvoltage. In addition, existence of generated water in diffusion passes such as pores in the GDL and channels in the separator interrupt hydrogen and oxygen diffusion, so called flooding. Since water is generated in cathode catalyst layer, flooding is often caused in cathode. When the consumption of oxygen exceeds the oxygen supply as the current density increases, a cell voltage drastically decreases as shown in figure 1-2. Therefore, to increase a cell voltage at higher current density and extend current limit, discharging excess water in the cell is necessary, as well as the sufficient supply of oxygen.

In the case of vehicle applications, the higher performance at higher current density is required compared with the case of stationary applications because of the requirement for the scale down of fuel cell system to fit into vehicle packages, and for vehicle driving conditions such as acceleration and climbing up slopes. Therefore, reducing the diffusion overvoltage at high load current is rather important for vehicle use.[32]

To reduce the diffusion overvoltage in cathode channels and the GDL, designs of the flow channel and the GDL play important roles.

1-3. Requirement for GDL design to decrease diffusion overvoltage

Most of the commercialized GDL consists of the high-temperature treated carbon-fiber

and the resin, pores with diameter of several dozen to hundred micro meters connected for each are dispersed in. The requirement for the GDL design consists of five points below:

1) Reactant transport: The lower resistance of gas diffusion from channels to the catalyst layer is required for sufficient supply of the reactant.

2) Water transport: To prevent flooding inside the GDL, water as ORR reaction product should be smoothly discharged from the GDL. Vapor is generally discharged by diffusion along the gradient of partial pressure, while liquid water moves to the surface of the GDL by capillary force in micro pores.

3) Electron transport: The higher electrical conductivity and lower contact resistance at interfaces between the separator and the GDL, as well the GDL and the catalyst layer are required.

4) Thermal management: The appropriate value of the thermal conductivity should be determined on each cell design to prevent both the heat spot emerge which accelerate the catalyst degradation and the carbon corrosion, and alleviate flooding by excessively low cell-temperature.

5) Mechanical support: The mechanical strength of the GDL is required for mechanical support to protect the MEA from damage during assembly and to maintain lower interfacial contact resistance at separator/GDL and GDL/MEA interfaces.

Among these requirements, 1) and 2) are necessary to be improved for decrease of the gas diffusion resistance and diffusion overvoltage. Project from the New Energy and Industrial Technology Development Organization (NEDO) set 16 sec m^{-1} or lower value of the gas diffusion resistance to achieve the performance target of FCV in 2040.[33]

The gas diffusion resistance, which is also affected by the design of flow channels as

described later, is considered to be decreased with thinner GDL because of shorter diffusion passes for gases and liquid water. Based on this theory, a GDL composed full of the MPL without carbon-fiber substrate is suggested and being developed. The GDL without substrate, whose thickness is expected to under 50 μm, enables to shorten diffusion passes of gases and liquid water, as well as avoid water accumulation in the GDL substrate. However, thin GDL has issues on the difficulty of gas diffusion to the MEA of the area under channel ribs than thicker GDL, as well as its brittleness.

1-4. Development of flow channel design to decrease diffusion overvoltage

Currently, practical designs for gas flow channels are generally based on two types, one being the parallel flow geometry, which consists of multiple channels running in the same direction, and the second being the serpentine flow geometry, which consists of a single channel going from the inlet to the outlet of the gas manifold. Mixtures of these two designs have also been examined.[34]

The main advantage of parallel flow channels is that the length from the inlet to the outlet of each channel is short, so the pressure drop from the channel inlet to outlet can be reduced. This lower pressure drop enables the demand for compressor power which enhance the pressure of the supplied gas smaller, as well as decreases local power density at the outlet side of the flow path. On the other hand, since the gas supplied from the cell inlet is distributed to multiple channels, the gas flow rate per channel is smaller than the single flow-channel design. This lower gas flow rate makes it more difficult to discharge the liquid water existing in the channel, so flooding within the channel will likely occur under high load-current conditions.[35]

The main advantage of serpentine flow channels is that the number of flow channels is smaller than that of parallel flow channels, so the gas flow rate and flow rate per channel can be increased. Therefore, diffusion overvoltage at high load currents can be suppressed compared to parallel flow channels. On the other hand, the pressure drops of the supplied gas increases, so the demand for the power of the compressor which enhance the pressure of supplied gas increases especially on the cell with larger active area such as for vehicle applications.

In addition to each issue on these two flow-channel designs, one of the common issues of both these flow shapes is gas diffusion blockage in the GDL by accumulated water under the ribs, which are located between neighboring channels. The amount of accumulated water grows larger as the current density increases.[36,37] To avoid water accumulation under the ribs, a separator of 3D fine-mesh structure was developed by Toyota and applied to the FC cell for 1st generation Mirai released in 2015.[9] However, these designs lead to increased pressure loss due to the narrow or complex-shaped channel spaces, they require a high-power compressor to introduce the feed gases at a high inlet pressure, resulting in decreased net FC system power. Furthermore, there is a problem of increased cell cost due to the increased demands on the processing accuracy of separators that form such complex flow channels. As a result, the channel design of cathode was replaced to the partially narrowed flow-channel with 2nd generation Mirai released in 2020. This partially narrowed flow-channel causes turbulent flow in channels which enhance the gas diffusion in and water discharge from the GDL.[38] However, the partially narrowed flow-channel has wider ribs than 3D fine-mesh separator, as conventional two flow-channels, so the issue of gas diffusion under ribs is expected to become apparent especially when collaborated with thinner GDLs described in Chapter 1-3.

Nguyen et al. proposed another flow design, i.e., interdigitated channels formed on the separator,[39,40] in which the channels on the inlet and outlet sides are not directly connected, so that the gas from the inlet is forced to flow into the flat GDL in order to reach the outlet side as shown in figure 1-3. The gas that flows in the GDL is essentially under forced convection, resulting in enhanced mass transport to the catalyst layer and enabling water discharge from the GDL in a more efficient manner compared to that for the conventional designs. The interdigitated shape of the gas flows channel contributes to a higher cell power output compared to that for the parallel arrangement,[39,40,41] as well as more efficient fuel consumption by maintaining high cell performance at low air flow rates, since a smaller air compressor is required.[42] The interdigitated channels alleviate the decrease of net power in a fuel cell system when the active area of the cell increases, while serpentine channels lead to a decrease in net power because of the further increase

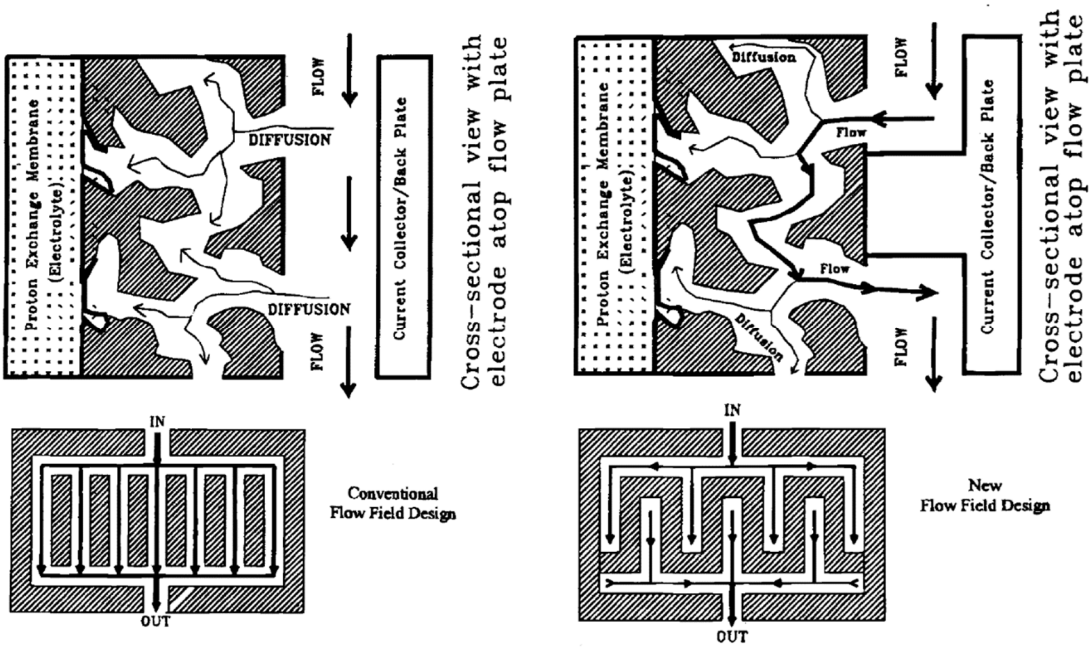

(a) Parallel flow channel (b) Interdigitated flow channel

Figure 1-3. Schematic images of (a) parallel flow channel and (b) interdigitated flow channel

of the gas pressure drop, depending on the active area increase.[43] Zhou et al.. pointed out two issues of interdigitated channels: one is the nonuniform gas flow that occurs as a result of water accumulation in the GDL; the other is the acceleration of cell dry-out due to forced convection in the GDL under low humidity gas conditions; both lead to decreased power.[44] Nguyen et al. pointed out another issue, which is that, as a result of nonuniform gas flow in a certain cell, the pressure drop increases and fuel starvation in the certain cell can occur, because each cell is connected in parallel.[45]

1-5. Innovative design to achieve targets on cell performance

M. Watanabe et al. proposed a new gas flow design, which consists of a flat metal separator and a GDL with gas-flow channels on its surface, while conventional flow channel designs consist of a flat GDL and metal or graphited carbon separator with gas-flow channels on its surface.[46] This new design has been integrated into a single-cell stack and compared its performance as a polarization curve with a conventional cell which consists of a serpentine flow channel and a flat GDL. The new design cell has showed higher cell voltage at the polarization curve than the conventional serpentine flow cell across all current density from 0 to 3.0 A cm^{-2}. This new design has another advantage on its lower cost expectation. The channel formed GDL is fabricated in integrated molding process without high temperature treatment over thousand degrees, furthermore, the flat separator eliminates multi-press forming for conventional separators.

I focused on this performance improvement with newly designed cell with interdigitated flow-channels on the GDL compared to the conventional serpentine cell, because previous research from G. Advani et al. showed that a cell with serpentine flow-

channels on the separator showed higher performances than a cell with interdigitated flow-channels on the separator.[40,45] Although there are differences in the cell design used in these two researches, such as the active area of the cell, MEA (membrane electrode assembly), and GDL materials, it is noteworthy that the new design of a cell with interdigitated flow channel showed higher performance than a cell with serpentine flow channel which showed higher performance than a cell with conventional design of the interdigitated flow channel. I proposed that this performance improvement with the newly designed cell was due to the effect of the ribs being porous when flow channels are formed on the GDL. However, it is necessary to elucidate both the detailed contribution to the improvement of cell performance and the mechanism to validate the proposal.

If this newly designed flow-channel is clarified to overcome issues of conventional interdigitated flow-channels, its potential to achieve the target of FC stack performance in 2040 by overcoming issues on GDL and flow-channel design is also expected.

1-6. Objective and structure of this research

As mentioned above, the newly designed cell with interdigitated channels on the GDL has a potential to overcome issues of the conventional interdigitated cell with channels on the separator which is the performance decrease at high load current and high humidity conditions caused by water accumulation in the GDL pores. Therefore, the objective of this study was set on clarifying advantages on the performance and the mechanism to improve the performance.

At first, in Chapter 2, I prepared two cells with 3.0 × 9.7 cm active area: one had interdigitated flow-channels on the GDL of cathode; the other had serpentine flow-

channels on the separator of cathode. These two cells are the same design as cells tested in previous research by M. Watanabe et al. In this study, to clarify differences in behavior of cells during operating conditions with excess water existence in cathode, two cells are operated in conditions with variations of cathode air-flow rate. I compared the drop down of cell voltages and the increase of cathode pressure drops during the decrease of the air flow rate, then compared the recovery of cell voltages and the decrease of cathode pressure drops during the decrease of the air flow rate. Furthermore, I designed and constructed four cells with 1.0 × 1.0 cm active area. The cell size was designed as the partially extracted model of full-size fuel cells to investigate local performances and its distributions. The flow channel design of four cells consisted of the combination of two flow-channel shapes and two flow-channel positions. Shapes of flow channel are interdigitated and parallel, while positions of flow channel are on the GDL and on the separator. These four cells are operated in conditions with variations of the current density, the oxygen percentage in cathode gas, the air flow rate and the relative humidity of air, and the characteristics of cells including cell voltages, diffusion overvoltages, ohmic resistances and pressure drops are compared in these cells. At the end of this chapter, I clarified advantages of a newly designed cell with interdigitated flow channel on the GDL on its performance, furthermore, I proposed the mechanism that the newly designed cell obtained such advantages compared with the conventionally designed cell.

Next, in Chapter 3, to validate the mechanism of the newly designed cell which proposed in Chapter 3, I constructed a method to clarify the distribution of liquid water, temperature and gas flux in the GDL and temporal changes of these factor by combining experimental and numerical analysis. As the experimental analysis, I used X-ray imaging to visualize liquid water inside the cell during operation, and as the numerical analysis, I

used a combination of fluid dynamics and electrochemical calculations to determine temperature distributions and gas flux in the GDL during cell operation.

Next, in Chapter 4, I designed and constructed four cells with 1.0 × 10 cm active area. This cell size was designed as the extended model of the cell tested in Chapter 3 along the gas flows direction, to verify whether advantages of the newly designed cell with interdigitated flow-channel on the GDL on its performances was available also in cells with larger cells such as for vehicles. These cells are operated in conditions with variations of the current density and the relative humidity, and cell characteristics in each cell including cell voltages, diffusion overvoltages, ohmic resistances and pressure drops are compared for each.

Finally, in Chapter 5, I summarized results of Chapter 2, 3, 4 and 5, resulting in clarifying advantages of the newly designed cell with interdigitated flow-channel on the GDL compared with conventional cells, as well future prospects including challenges on applying to practical cells.

1-7. References

1. N. Abas, A. Kalair and N. Khan, Review of fossil fuels and future energy technologies, *Futures*, Vol. 69 (2015) 31-49
2. H. C. Frey, Trends in onroad transportation energy and emissions, *Journal of the Air & Waste Management Association*, Vol. 68 (2018) 514-563
3. X. Zhao, S. Wang and X. Wang, Characteristics and Trends of Research on New Energy Vehicle Reliability Based on the Web of Science, *Sustainability*, Vol. 10 (2018) 3560

4. F. Un-Noor, S. Padmanaban, L. Mihet-Popa, M. N. Mollah and E. Hossain, A Comprehensive Study of Key Electric Vehicle (EV) Components, Technologies, Challenges, Impacts, and Future Direction of Development, *Energies*, Vol. 10 (2017) 1217
5. A. Ajanovic, The future of electric vehicles: prospects and impediments, *Willey Interdisciplinary Review: Energy and Environment*, Vol. 4, Issue 6 (2015) 521-536
6. M. P. Mills, Electric Vehicles for Everyone? The Impossible Dream, *blazing cat fur*, (2023)
7. H. Fayaz, R. Saidur, N. Razali, F. S. Anuar, A. R. Saleman, M. R. Islam, An overview of hydrogen as a vehicle fuel, *Renewable and Sustainable Energy Review*, Vol. 16 (2012) 5511-5528
8. N. Qin, A. Raissi and P. Brooker, Analysis of Fuel Cell Vehicle Development, Report by *Electric Vehicle Transportation Center*, (2014) https://www.fsec.ucf.edu/en/publications/pdf/FSEC-CR-1987-14.pdf
9. T. Yoshida and K. Kojima, Toyota MIRAI Fuel Cell Vehicle and Progress Toward a Future Hydrogen Society, *The Electrochemical Society Interface*, Summer (2015)
10. D. Apostolou and G. Xydis, A literature review on hydrogen refuelling stations and infrastructure. Current status and future prospects, *Renewable and Sustainable Energy Reviews*, Vol. 113 (2019) 109292
11. Fuel Cell Works, Record Number of Newly Opened Hydrogen Refuelling Stations in 2020 https://fuelcellsworks.com/news/record-number-of-newly-opened-hydrogen-refuelling-stations-in-2020/
12. I. P. Jain, Hydrogen the fuel for 21st century, *International Journal of Hydrogen*

Energy, Vol. 34, Issue 17 (2009) 7368-7378

13. S. Chaudhuri and J. T. Muckerman, First-Principles Study of Ti-Catalyzed Hydrogen Chemisorption on an Al Surface, *The Journal of Physical Chemistry*, Vol. 109, Issue 15 (2005) 6952-6957
14. G. Arnold and J. Wolf, Liquid Hydrogen for Automotive Application Next Generation Fuel for FC and ICE Vehicles, *TEION KOGAKU*, Vol. 40, No. 6 (2005) 221-230
15. S. W. Jorgensen, Hydrogen storage tanks for vehicles: Recent progress and current status, *Current Opinion in Solid State and Materials Science*, Vol. 15, Issue 2 (2011) 39-43
16. Yamashita A., Kondo M., Goto S. and Ogami N., Development of High-Pressure Hydrogen Storage System for the Toyota "Mirai", *SAE Technical Paper,* 2015-01-1169 (2015)
17. S. Tanaka, K. Nagumo, M. Yamamoto, H. Chiba and K. Yoshida, Fuel cell system for Honda CLARITY fuel cell, *The Electrochemical Society Transportations,* Vol. 3 (2020) 100046
18. B. K. Hong and S. H. Kim, Recent Advances in Fuel Cell Electric Vehicle Technologies of Hyundai, *The Electrochemical Society*, Vol. 86, No. 13 (2018) 3-11
19. NEDO, Technology Development Roadmap of Fuel Cells for FCV https://www.nedo.go.jp/content/100944012.pdf
20. L. Carrette, K. A. Friedrich and U. Stimming, Fuel cells: principles, types and applications, *ChemPhysChem*, Vol. 1, Issue 4 (2000) 162-193
21. JC. Yang, YS. Park, SH. Seo, HJ. Lee and JS. Noh, Development of a 50 kW PAFC power generation system, *Journal of Power Sources*, Vol. 106 (2002) 68-75

22. F. Alcaide, P. L. Cabot and E. Brillas, Fuel cells for chemicals and energy cogeneration, *Journal of Power Sources*, Vol. 153 (2006) 47-60
23. Nissan Motor Corporation, Nissan Announces Development of the World's First SOFC-powered Vehicle System that Runs on Bio-ethanol Electric Power https://newsroom.nissan-global.com/releases/160614-01-e
24. M. Yamauchi, T. Fujii and K. Sugiura, Development of a Metallic Separator for a Micro-PEFC, *The Electrochemical Society Transactions*, Vol. 42, Issue 1 (2012)
25. C. Bernay, M. Marchand and M. Cassir, Prospects of different fuel cell technologies for vehicle applications, *Journal of Power Sources*, Vol. 108 (2002) 139-152
26. F. Okazaki, K. Sugiura, T. Ito, K. Inukai and M. Utaka, Selection of the Optimized Carbon Material for PEFC Separator, *The Electrochemical Society Transactions*, Vol. 83, Issue 1 (2018)
27. Y. Souma, I. Muto and N. Hara, Electrochemical Properties and Contact Resistance of Titanium in PEFC Separator Environment, *Electrochemical Society Meeting Abstracts*, Vol. MA2008-02 (2008) 1586
28. Y. Aoyama, K. Suzuki, Y. Tabe, T. Chikahisa and T. Tanuma, Water Transport and PEFC Performance with Different Interface Structure between Micro-Porous Layer and Catalyst Layer, *Journal of the Electrochemical Society*, Vol. 163, No.5 (2016) F359
29. A. Saccà, A. Carbone, R. Pedicini, G. Portale, L. D'Ilario, A. Longo, A. Martorana and E. Passalacqua, Structural and electrochemical investigation on re-cast Nafion membranes for polymer electrolyte fuel cells (PEFCs) application, *Journal of Membrane Science*, Vol. 278 (2006) 105-113
30. N. Wagner, W. Schnurnberger, B. Müller and M. Lang, Electrochemical impedance

spectra of solid-oxide fuel cells and polymer membrane fuel cells, *Electrochimica Acta*, Vol. 43, Issue 24 (1988) 3785-3793

31. J. Wu, X. Z. Yuan, H. Wang, M. Blanco, J. J. Martin and J. Zhang, Diagnostic tools in PEM fuel cell research: Part I Electrochemical techniques, *International Journal of Hydrogen Energy*, Vol. 33, Issue 6 (2008) 1735-1746
32. R. K. Ahluwalia and X. Wang, Fuel cell systems for transportation: Status and trends, *Journal of Power Sources*, Vol. 177, Issue 1 (2008) 167-176
33. NEDO, Technology Development Roadmap of Fuel Cells for FCV and HDV https://www.nedo.go.jp/content/100956711.pdf
34. Y. Yu, Z. Zhan, L. Ye, X. Yang, X. Wan, P. C. Sui and M. Pan, Effects of Distribution Zone Design on Flow Uniformity and Pressure Drop in PEMFC, *Journal of Electrochemical Society*, Vol. 168, No.9 (2021) 094505
35. H. Liu, P. Li, D. Juarez-Robles, K. Wang and A Hernandez-Guerrero, Experimental study and comparison of various designs of gas flow fields to PEM fuel cells and cell stack performance, *Frontiers in Energy Research*, Vol. 2 (2014)
36. K. Ito, K. Ashikaga, H. Masuda, T. Oshima, Y. Kakimoto and K. Sasaki, Estimation of flooding in PEMFC gas diffusion layer by differential pressure measurement, *Journal of Power Sources*, Vol. 175, Issue 2 (2008) 732-738
37. H. Li, Y. Tang, Z. Wang, Z. Shi, S. Wu, D. Song, J. Zhang, K. Fatih, J. Zhang, H. Wang, Z. Liu, R. Abouatallah and A. Mazza, A review of water flooding issues in the proton exchange membrane fuel cell, *Journal of Power Sources*, Vol. 178, Issue 1 (2008) 103-117
38. Y. Ma, H. Gyoten, M. Kageyama and M. Kawase, Effects of Partially Narrowed Flow Channel on Performance of Polymer Electrolyte Fuel Cell, *The Electrochemical*

Society Transactions, Vol. 109, No. 9 (2022)

39. T. V. Nguyen, A Gas Distributor Design for Proton-Exchange-Membrane Fuel Cells, *Journal of Electrochemical Society*, Vol. 143, No.5 (1996)
40. D. L. Wood, III, Jung S. Yi. and T. V. Nguyen, Effect of direct liquid water injection and interdigitated flow field on the performance of proton exchange membrane fuel cells, *Electrochimica Acta*, Vol. 43, No. 24, 3795 (1998)
41. D. Spernjak, A. K. Prasad and S. G. Advani, In situ comparison of water content and dynamics in parallel, single-serpentine, and interdigitated flow fields of polymer electrolyte membrane fuel cells, *Journal of Power Sources*, Vol. 195, Issue 11 (2010) 3553-3568
42. W. M. Yan, C. Y. Chen, S. C. Mei, C. Y. Soong and F. Chen, Effects of operating conditions on cell performance of PEM fuel cells with conventional or interdigitated flow field, *Journal of Power Sources*, Vol. 162, Issue2 (2006) 1157-1164
43. N. Limjeerajarus and T. Santiprasertkul, Novel hybrid serpentine-interdigitated flow field with multi-inlets and outlets of gas flow channels for PEFC applications, *International Journal of Hydrogen Energy*, Vol. 45, Issue 25 (2020) 13601-13611
44. A. D. Le, B. Zhou, A generalized numerical model for liquid water in a proton exchange membrane fuel cell with interdigitated design, *Journal of Power Sources*, Vol. 193, Issue 2 (2009), 665-683
45. T. V. Nguyen and M. W. Knobbe, A liquid water management strategy for PEM fuel cell stacks, *Journal of Power Sources*, Vol. 114, Issue 1 (2003) 70-79
46. M. Watanabe, H. Yanai and M. Nasu, Development and Analysis of an Innovative Flat-Metal Separator Integrating the GDL with Gas-Flow Channels as PEFC Components, *Journal of The Electrochemical Society*, Vol. 166, No. 7 (2019) F3210

Chapter 2 Studies on Performance Stability Improvement of a Cell with Interdigitated Flow Channels on the GDL under various operating conditions

2-1. Introduction

As mentioned in 1-2 of Chapter 1, the presence of water in a cell significantly affects the performance of the cell.[1,2] The polymer electrolyte that constitutes the catalyst layer and the membrane is the path for protons generated by HOR at anode to move to cathode, and protons diffuse within the polymer electrolyte as H_3O^+ that pseudo-bonds with water. Therefore, it is desirable that the polymer electrolyte has sufficient water uptake. On the other hand, the liquid water present in the GDL adjacent to the catalyst layer and inside the separator adjacent to the GDL causes flooding that occupies channel space of the separator and pores of the GDL, which are the diffusion paths of hydrogen or oxygen, resulting in fuel shortage. In particular, at the interface between the ribs of the separator, which is a solid material, and the GDL, which is a porous material, generated water that has diffused from the catalyst layer to the GDL is blocked by the rib surface and accumulates, making it difficult for the fuel to diffuse.[3]

The new channel design in which channels formed on the GDL surface, as mentioned in 1-3 of Chapter 1, was proposed and developed by Watanabe et al.[4] to solve this problem of liquid water accumulation at the interface between the rib and GDL. In the case where flow channels are formed on the GDL, the ribs between flow channels are made of porous material, unlike the case where flow channels are formed on the separator. As shown in Figure 2-1, the position of the interface between the solid material and the porous material is located further from the catalyst layer depending on the height of the ribs, this makes

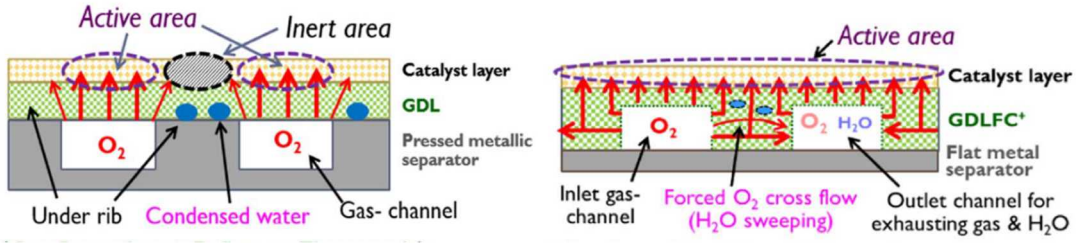

(a) Serpentine channels on the separator (b) Interdigitated channels on the GDL

Figure 2-1. Schematic images of the cross section of cells: (a) Serpentine flow-channels on the separator and (b) Interdigitated flow channels on the GDL

it easier to secure fuel diffusion paths to reach the catalyst layer even if liquid water is condensed near the interface between the separator and the GDL.[4] In addition, since the flow channel design is interdigitated, the channel connecting with the cell inlet and the channel connecting with the cell outlet are adjacent through the ribs, so that the forced convection of the supplied gas makes accumulated water around the interface between the separator and the GDL is easily discharged.[5,6]

In the research by Watanabe et al., the polarization curve was measured at a cell temperature of 80℃, supply air humidification of 100%RH, and a utilization rate of 40%.[4] At higher current densities, increased water accumulation in the cell by cathode reaction is expected. Despite the increased water, the result that the newly designed cell with interdigitated flow channels on the GDL showed higher performance than that of a cell with serpentine flow channels on the separator at all current densities indicates that the interdigitated channels with porous ribs have a potential to overcome the issue of the conventional interdigitated channels with solid ribs as the performance decrease at high humidification conditions. However, to clarify the advantage of newly designed channel on its performance under high humidity conditions, it is more desirable to compare the performance of cells not only in a fixed operating condition but also in variations of the

humidity. In the first half of this chapter, two cells with 3.0 × 9.7 cm active area are operated in conditions with variations of cathode air-flow rate, to control the amount of remaining water in cells in a simple method. Since the force to discharge water from channels and the GDL depends on the gas flows rate, as the air flow rate decreases, the water accumulation in cells increases.

In addition, the conventional interdigitated flow channel on the separator has been known to have issues of performance decrease under low humidity conditions, as well as under high humidity conditions.[7] Assuming that porous ribs contribute to liquid water management based on the performance improvement described above, I focused on the possibility that the newly designed cell with interdigitated flow-channel on the GDL shows higher performance than the conventional cell with interdigitated flow-channel on the separator also under low humidification conditions. The notable advantage of the conventional interdigitated flow-channel on the separator is the lower diffusion overvoltage compared to the parallel flow-channel contributed by the forced convection of supplied gas in the GDL to enhance fuel supply to the catalyst layer.[5,6] In the case that ribs in the interdigitated flow channel are changed from solid to porous materials, it is also necessary to validate whether the advantage on oxygen supply to the catalyst layer would repeat same as the conventional flow design. In the second half of this chapter, I constructed and tested four cells with the combination of different flow-channel shapes and flow-channel positions to investigate these two issues.

2-2. Experimental

2-2-1. Experiment by cells with 3.0 × 9.7 cm active area

First, two cells of different channel designs were used to compare the cell performances. One had the interdigitated shape on the GDL; the other had the serpentine shape on the separator. Both cells had a 3.0 × 9.7 cm active area. Hereafter, the symbols of each channel design will be used as follows: GDL with interdigitated ribs + flat separator, GDL(ID)/SP(F); flat GDL + separator with serpentine ribs, GDL(F)/SP(P).

These cell designs were the same as those used in the research by Watanabe et al.[4] The experimental cell with the active area of 3.0 × 9.7 cm is designed to partially simulate the full-sized FC stack. The length of the 9.7 cm is similar to the actual length of the full-sized stack to mimic the variations of internal conditions in the cell from inlet side to outlet side. In the case of the perpendicular direction, considering that the same flow design is periodically repeated in the full-sized stack, the width of the experimental cell is reduced to 3.0 cm in order to decrease the power requirements but still capture the essential operation of the periodic structure.

The GDL substrates with/without gas-flow channels were produced by use of quality-controlled fabrication processes by Enomoto Co. Ltd. The porosity of the cathode GDL in this study was 61.2%, and the pore diameters were distributed from 2 to 20 μm, obtained by use of a CFP-1100AXL Perm Porometer (Seika Digital Image Corp.). This

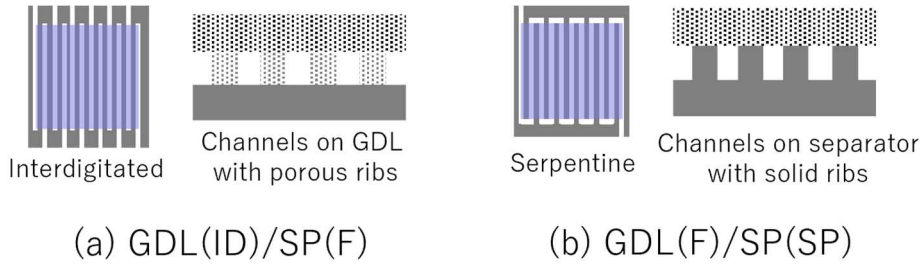

Figure 2-2. Schematic images of each flow channel design and corresponding symbols noted: The aspect ratio of images is different from the actual size of 3.0 × 9.7 cm.

GDL was fabricated in a dedicated process to enable the same structure to be realized in the flat areas of the GDL (roof) and the ribs of the GDL (rib) in the GDL. The GDL used for the cathode did not contain PTFE, but contained an engineering plastic as the binder for the carbon fibers.[16] The water contact angle of the cathode GDL was 128˚, obtained by use of a DMo-501SA contact angle measurement system (Kyowa Interface Science Co., Ltd.). As a reference, the contact angle of a commercial carbon paper from Toray Co., Ltd. was found to be 136˚ by use of the same equipment, so the cathode GDL applied in this study was slightly more hydrophilic than the commercial counterpart. Since the structures of the GDL (roof), grooves and GDL (rib) in the GDL were identical, the contact angles of all parts of the GDL were considered to be the same.

The microporous layer (MPL) treatments were determined to be the same for all of the GDLs, and thus, the different behaviors observed among the cells were judged to be brought about by the differences of the shapes of the channels, including flat surfaces. FIB-SIM images of the GDLs with channels are shown in Figure 2-3.

The evaluation of cell performance with 3.0 × 9.7 cm active area was focused on two

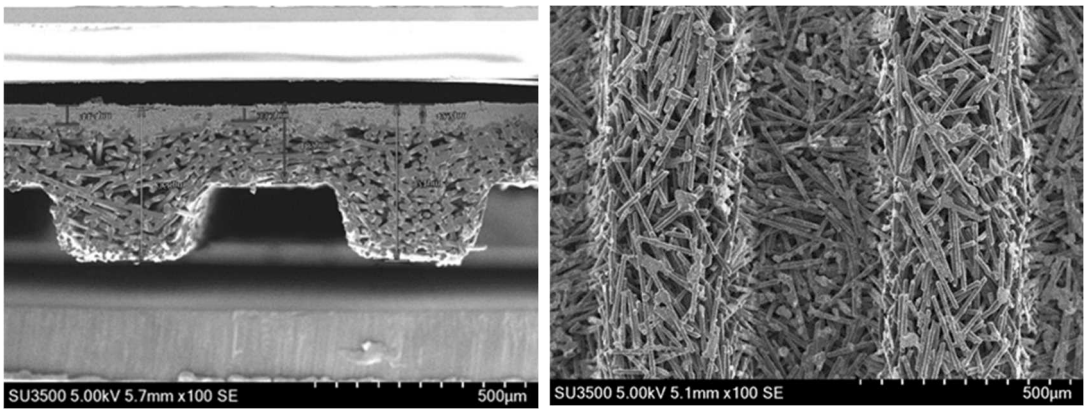

(a) cross-section (b) upper surface

Figure 2-3. FIB-SIM images of the GDL on which channels were formed. (a) Cross-section and (b) top view. The thickness was about 360 µm, including the microporous layer.

features: i) confirmation of repeatability on performances of two cells in polarization curves and on the performance advantage of GDL(ID)/SP(F) against GDL(F)/SP(SP); and ii) the advanced evaluation of cell performance stability during the change of the amount of remaining water in the cell. Before these experiments, both cells operated in conditioning test to enhance the initial performance of cells to a level. Table 2-1 shows the conditions of each experiment, and further details are indicated below.

Table 2-1. Experimental conditions of cells with 3.0 × 9.7 cm active area

Experiment		Polarization	Air flow-rate characteristics
Cell temperature		80 °C	
Current density		From 0 to 1.6 A cm^{-2}	1.0 A cm^{-2}
Anode	Gas	Pure hydrogen	
	Flow rate	Varied to maintain a constant U_{H2} = 70%	
	Relative humidity	80% RH	
	Outlet pressure	0 kPa	
Cathode	Gas	Air	
	Flow rate	Varied to maintain a constant U_{air} = 40%	From 0.6 to 1.2 NL min^{-1}
	Relative humidity	80% RH	
	Outlet pressure	0 kPa	

Conditioning. Anode and cathode were purged with dry nitrogen; then, hydrogen and air were supplied to the anode and cathode, respectively. The current density was increased from 0 to 1.6 A cm^{-2} in 0.2 A cm^{-2} steps and then maintained for 5 hours at 1.6 A cm^{-2}. The conditions of the supplied gases are same as the experiment of polarization as shown

in Table 2-1.

Polarization. After the conditioning was complete, the current density was increased and decreased between 0 and 1.6 A cm^{-2}, in steps of 0.2 A cm^{-2} (0.02 A cm^{-2} under 0 to 0.1 A cm^{-2}), and two complete cycles were carried out. The duration time at each current density was 5 minutes from 0 to 1.0 A cm^{-2}, and 10 minutes from 1.2 to 1.6 A cm^{-2}. During the second cycle, the average voltage of the cell was measured over the final 1 minute of the 5 minutes duration time at each current density and was plotted as the polarization curve.

Air flow-rate characteristics. The flow rate of supplied cathode air was decreased until the cell voltage began to decrease drastically and then increased. The current density was kept at 1.0 A cm^{-2}. The ranges of the air flow rates were 1.2 to 0.6 NL min^{-1}. The duration time at each air flow rate was 1 hour. The average voltage of the cell was measured over the final 1 minutes of 1 hour duration time at each air flow-rate. The cathode air pressure drop was measured simultaneously in order to estimate how much water had accumulated in the cell.

2-2-2. Experiment by cells with 1.0 × 1.0 cm active area

Second, four cells of different channel designs were examined and compared their performances in order to make clear the effect on cell performances depending on the difference in flow-channel shapes and rib materials. These cells had a 1.0 × 1.0 cm active area and included four different combinations of channel design based on the two channel shapes and the two channel locations as shown in figure 2-4. The channel shapes included

parallel and interdigitated, and the channel locations included on the GDL and on the separator. Hereafter, the symbols of each channel design will be used as follows: GDL with interdigitated ribs + flat separator, GDL(ID)/SP(F); flat GDL + separator with interdigitated ribs, GDL(F)/SP(ID); GDL with parallel ribs + flat separator, GDL(P)/SP(F); flat GDL + separator with parallel ribs, GDL(F)/SP(P).

The designs of the 1.0 × 1.0 cm active-area cells were basically the same as those of the JARI standard cell,[8] while the channels were specially designed for this study, as indicated in Table 2-2, with the exception of GDL(F)/SP(P), which was the same as that of the Ex-2B JARI standard cell. Images of the channel designs are shown in Figure 2-4.

The evaluation of cell performance was focused on two features: i) the peak power of the cell under the experimental conditions with sufficiently humidified gases and excess gas flow; and ii) the stability of cell power when experimental conditions were changed.

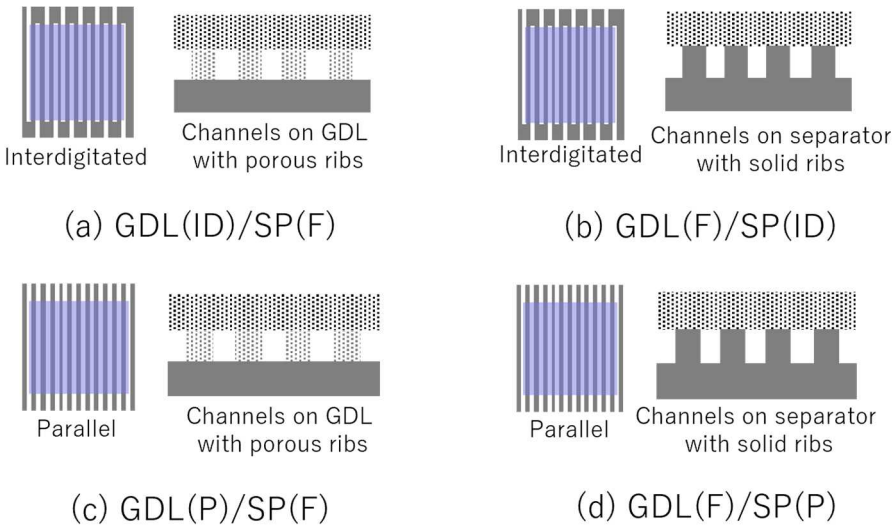

Figure 2-4. Schematic images of each flow channel design and corresponding symbols correlations with the various channel designs under various experimental conditions (e.g., oxygen percentage, relative humidity in the gas and gas pressure). In these cells, it is straightforward to achieve highly uniform distributions of reactants and products in the active area.

Table 2-2. Specifications of experimental cells with 1 × 1 cm active area

Cell type		GDL(F)/SP(P)	GDL(P)/SP(F)	GDL(F)/SP(ID)	GDL(ID)/SP(F)
Anode catalyst	Material	TEC10E50E (Tanaka Kikinzoku Kogyo)			
	Load	0.1 mg-Pt cm^{-2}			
	I/C	0.7			
Cathode catalyst	Material	TEC10E50E			
	Load	0.4 mg-Pt cm^{-2}			
	I/C	0.7			
Membrane	Material	Nafion HP (Chemours)			
Anode GDL	Material	29BC (SGL)			
Cathode GDL	Material	Enomoto Co., Ltd. test sample			
	Thickness	0.20 mm	0.36 mm	0.20 mm	0.36 mm
Flow design	Shape	Parallel		Interdigitated	
	Location	Separator	GDL	Separator	GDL
	Pitch	0.6 mm		0.7 mm	
	Channel width	0.4 mm		0.4 mm	
	Depth	0.2 mm		0.18 mm	
	Channel Number	17	16	16	16
	Channel Area	1.36 mm^2		1.01 mm^2	

The peak power was approximately obtained by carrying out polarization measurements after conditioning, with sufficient water and air supply to minimize both the proton diffusion resistance and flooding. The stability was evaluated in cell operations with changing three experimental conditions: the oxygen percentage, the gas flows rate, and the relative humidity of cathode inlet gas, at a constant current density of 1.0 A cm^{-2}. Details of these experimental conditions are indicated below and Table 2-3 shows a list of parameters in these operations.

Conditioning. Anode and cathode were purged with dry nitrogen; then, hydrogen and air were supplied to the anode and cathode, respectively. The current density was increased from 0 to 1.6 A cm^{-2} in 0.2 A cm^{-2} steps and then maintained for 5 hours at 1.6 A cm^{-2}. The conditions of the supplied gases are shown in Table 2-3.

Polarization. After the conditioning was complete, the current density was increased and decreased between 0 and 1.6 A cm^{-2}, in steps of 0.2 A cm^{-2} (0.02 A cm^{-2} under 0 to 0.1 A cm^{-2}), and two complete cycles were carried out. The duration time at each current density was 5 minutes from 0 to 1.0 A cm^{-2}, and 10 minutes from 1.2 to 1.6 A cm^{-2}. During the second cycle, the average voltage of the cell was measured over the final 1 minute of the 5 minutes duration time at each current density and was plotted as the polarization curve.

Oxygen concentration characteristics. The oxygen percentage of the supplied cathode gas was decreased and increased between 20% and 5% by changing the mixing ratio of oxygen and nitrogen; this cycle was carried out twice at 1 A cm^{-2}. The duration time at each oxygen percentage was 1 hour. This cycle test was repeated for each relative humidity condition of 100, 150, 40 and 15% RH in order (the dew points of the cathode air were 80, 90, 60 and 40 ˚C for each when the cell temperature was fixed at 80 ˚C).

Air flow-rate characteristics. The flow rate of supplied cathode air was decreased until the cell voltage began to decrease drastically and then increased; this cycle was carried out twice at 1 A cm^{-2}. The ranges of the air flow rates were 2.00 to 0.05 NL min^{-1}. The cycle test was repeated on 100 and 150% RH in order. The duration time at each air flow rate was 1 hour.

Table 2-3. Experimental conditions of cells with 1.0 × 1.0 cm active area

Experiment		Polarization	Oxygen percentage characteristics	Air flow rate characteristics	Relative humidity characteristics
Cell temperature		80 °C			
Current density		From 0 to 1.6 A cm^{-2}	1.0 A cm^{-2}		
Anode	Gas	Pure hydrogen			
	Flow rate	0.5 NL min^{-1}			
	Relative humidity	100% RH			
	Outlet pressure	0 kPa			
Cathode	Gas	Air	Nitrogen and oxygen (Oxygen percentage from 5 to 20%)	Air	Air
	Flow rate	2.0 NL min^{-1}	1.0 NL min^{-1}	From 0.05 to 2.0 NL min^{-1}	1.0 NL min^{-1}
	Relative Humidity	100% RH	15, 40, 100 and 150% RH*	100 and 150% RH	15, 40 and 150% RH*
	Outlet pressure	0 kPa			

*90 °C cathode dew point versus 80 °C cell temperature.

Relative humidity characteristics. After the evaluation of the air flow-rate characteristics, conditioning was implemented again to cancel the influence of the evaluation history in the previous stages; then, the relative humidity of the cathode air was varied: 150, 40, 150 and 15% RH at 1 A cm^{-2}. The duration times were 5 hours at 150 and 40% RH, while 20 hours was used at 15% RH because of the time taken to decrease the temperature of the cathode humidifier.

2-3. Results and Discussions

2-3-1. Experiment by cells with 3.0 × 9.7 cm active area

Polarization. Figure 2-5 shows the comparisons of the polarization curves between GDL(ID)/SP(F) and GDL(F)/SP(SP). As the research from Watanabe et al. showed, GDL(ID)/SP(F) showed obviously higher cell voltages across almost all range of current density from 0.1 to 1.6 A cm^{-2} than GDL(F)/SP(SP). Figure 2-5 shows the comparisons of three overvoltages: the activation overvoltage; the resistance overvoltage; and the diffusion overvoltage between GDL(ID)/SP(F) and GDL(F)/SP(SP) at 1.6 A cm^{-2}. Activation overvoltage was obtained as the IR-free Tafel Plot between 0.03 and 0.1 A cm^{-2}, i.e., kinetic region. Resistance overvoltage was calculated by multiplying the ohmic resistance and current density. Diffusion overvoltage was calculated by subtracting the resistance overvoltage from the activation overvoltage.[9] From the comparisons in two cells, GDL(ID)/SP(F) showed lower value in all three overvoltages than GDL(F)/SP(SP) across current density from 0 to 1.6 A cm^{-2}. As a result of these experiments, advantages of GDL(ID)/SP(F) on polarization curve and overvoltage were found to be repeated in this study.

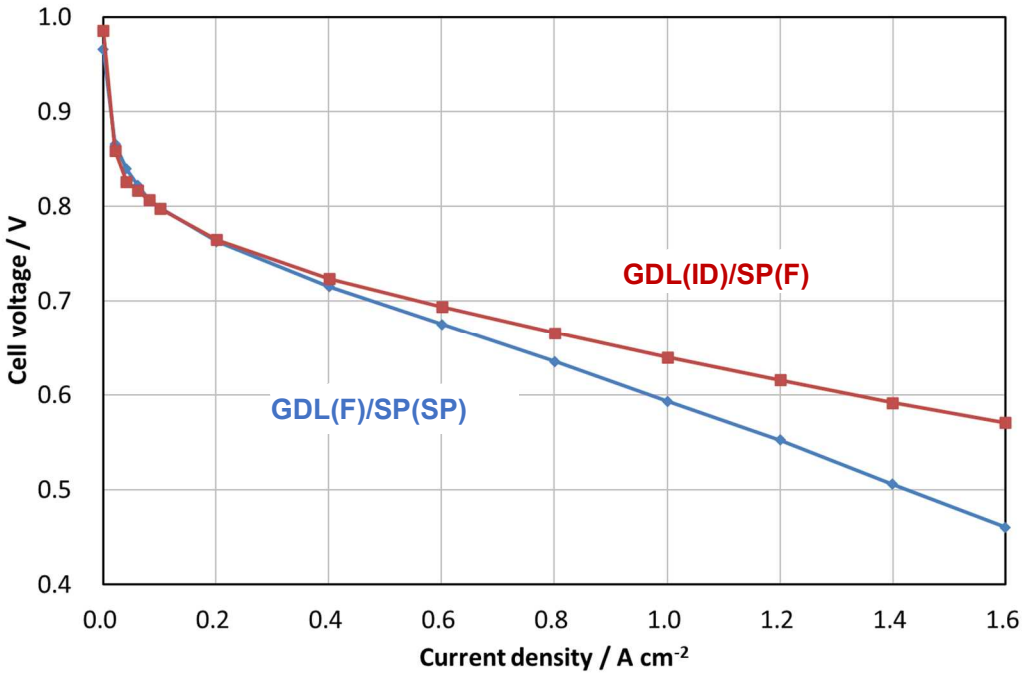

Figure 2-5. Polarization curves of GDL(ID)/SP(F) and GDL(F)/SP(SP) in a 3.0 × 9.7 cm cell obtained at a cell temperature of 65 °C, relative humidity of 80% RH on anode/cathode, hydrogen utilization ratio of 70% and air utilization ratio of 40%.

Air flow-rate characteristics. Figures 2-7 shows the comparisons of the dependences of the IR-included cell voltage and the pressure drop on the air flow rates, or the Uair, between the GDL(ID)/SP(F) and GDL(F)/SP(SP) cells at a constant current loading of 1.0 Acm^{-2}. The data were collected every 1 min before changing the air flow rate stepwise. The solid lines were measured during decreasing air flow rate from 1.2 to 0.6 NL min^{-1}, while the dotted lines were measured during increasing rates from 0.6 to 1.2 NL min^{-1}. The Uair values corresponding to the increase of air flow rate from 1.2 to 0.6 NL min^{-1} were 40 to 80%, respectively.

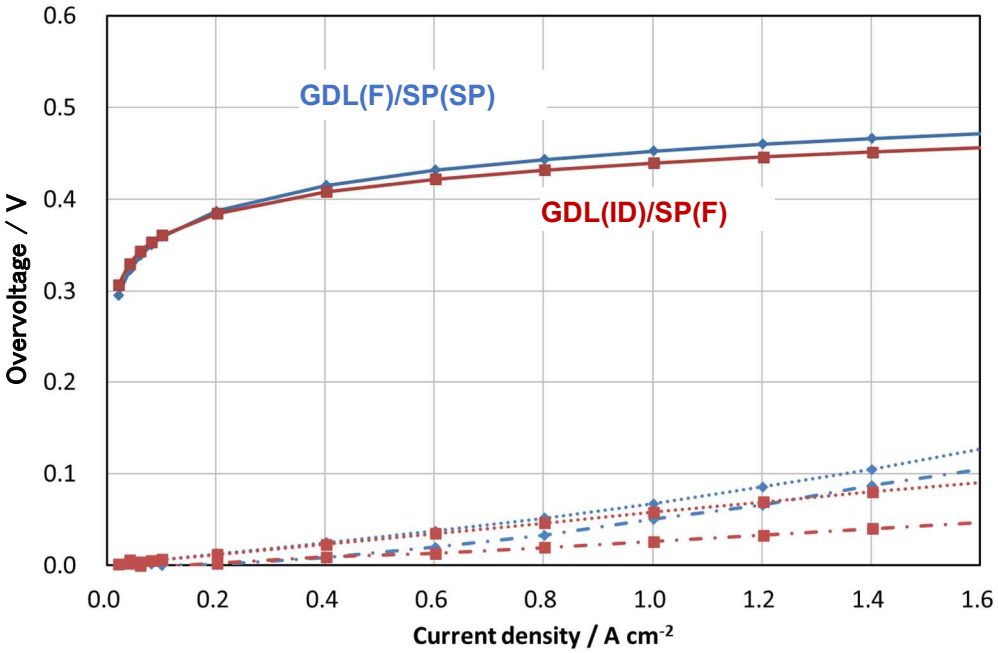

Figure 2-6. Overvoltages of GDL(ID)/SP(F) and GDL(F)/SP(SP) in a 3.0 × 9.7 cm cell calculated from the results of Figure 2-5. Solid lines (-) show activation overvoltage, dotted lines (---) show resistance overvoltage and dot-dashed lines (–·–) show diffusion overvoltage.

As shown in figure 2-7(a), during the phase of air flow-rate decrease from 1.2 NL min^{-1} to 0.6 NL min^{-1}, the cell voltage for GDL(F)/SP(SP) decreased linearly as an air flow-rate decreased, and then decreased steeply for air flow-rate below 0.8 NL/min, dropping to values lower than 0.4 V. However, the voltages for GDL(ID)/SP(F) were maintained above 0.6 V down to 0.8 NL min^{-1}. and then decreased but remained higher than 0.55 V. The voltage at an air flow rate of 1.2 NL min^{-1} for the GDL(ID)/SP(F) was higher by ca. 0.05V than that of GDL(F)/SP(SP) and the voltage differences were much pronounced with decreasing the flow rate, more than 0.25 V at 0.7 NL min^{-1}. Such a robustness of the cell voltage for the former versus the decrease of the flow rate or the increase of U_{air} can be attributed to the enhanced convection of air through the porous ribs compared to

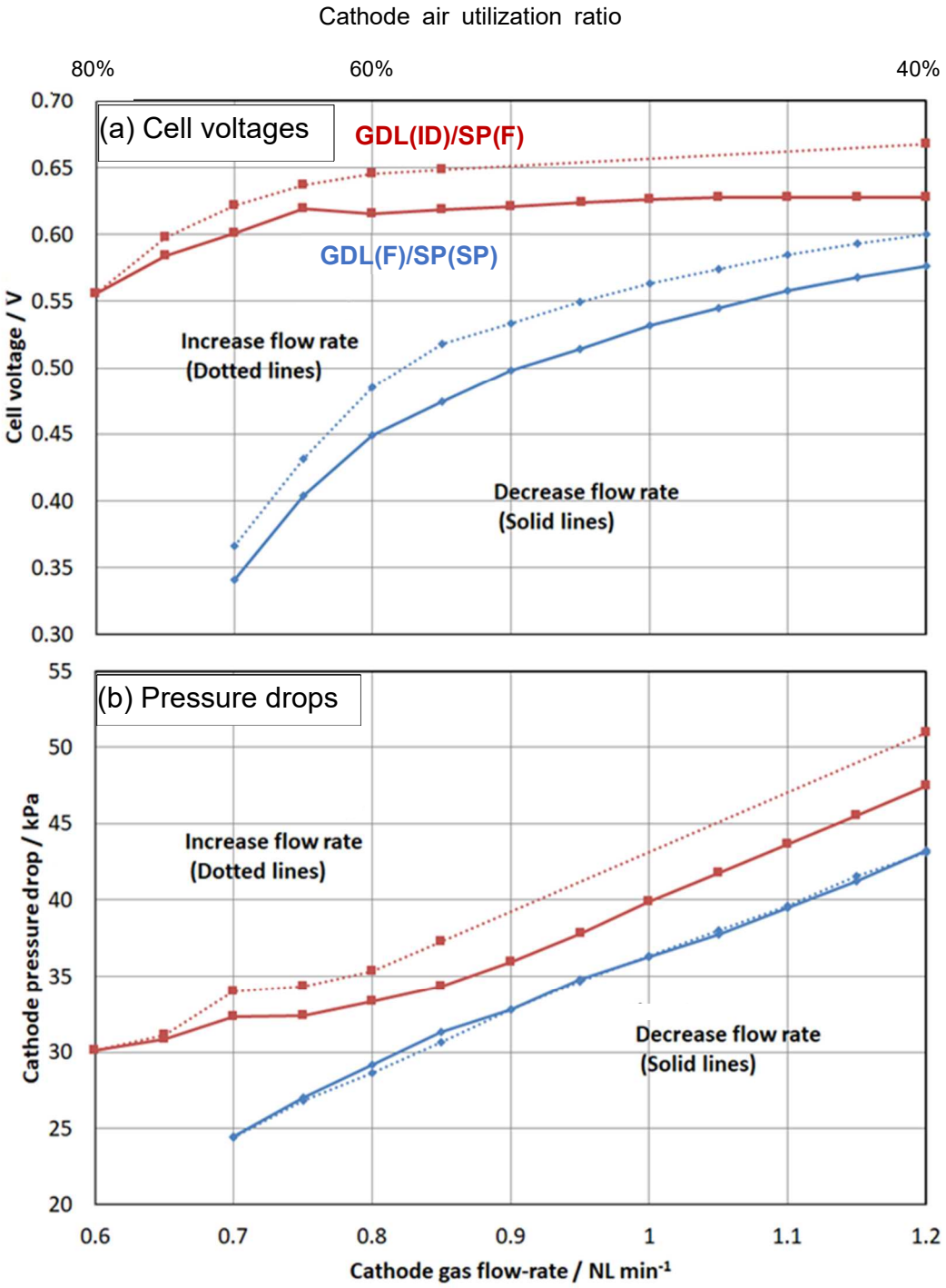

Figure 2-7. Behavior of (a) cell voltages and (b) cathode pressure drops when the air flow rate decreases from 1.2 to 0.6 NL min^{-1} (solid lines) and then increases from 0.6 to 1.2 NL min^{-1} (dotted lines) in cells of GDL(ID)/SP(F) and GDL(F)/SP(SP) with 3.0 × 9.7 cm active area. The current density was maintained at 1.0 A cm^{-2} during the experiment.

GDL(F)/SP(SP). During the subsequent increasing flow-rate phase, the cell voltages of both cells recovered and even exhibited higher voltages than those measured during the decreasing flow-rate phase.

Figure 2-7(b) shows the air pressure-drop behaviors measured at the same time for the increasing and decreasing flow rates. In the case of the GDL(F)/SP(SP) cell, the pressure drops showed a linear dependency upon both increasing and decreasing air flow rates over the range to 0.7 NL/min for the voltage measurement available. However, at 0.6 NL min^{-1}, the voltage dropped rapidly and fell below the lower threshold potential of the evaluation device, making it impossible to acquire data. The flooding of the GDL under the ribs was the most likely cause.

In the case of the GDL(ID)/SP(F) cell, the pressure drops decreased linearly from 1.2 to 0.9 NL min^{-1} depending on the flow rate, similar to that of GDL(F)/SP(SP), i.e., 38 kPa/ NL min^{-1}, and then the slope became smaller from 0.9 to 0.6 NL min^{-1}. The leveling-off of the pressure drop may be caused by an accumulation of liquid water in the porous ribs, generated at the cathode. During the increasing air flow rate phase, the pressure drops of the GDL(ID)/SP(F) maintained higher values than those observed during the decreasing air flow rate phase, unlike GDL(F)/SP(SP) which showed reversible changes. This result indicates that the excess water which accumulated during the low air flow rate remained in the GDL, even when the air flow rate recovered to 1.2 NL min^{-1}. It should be noted, however, that the remaining water in the GDL(ID) did not appear to disturb the air diffusion to the cathode catalyst layer, because the cell voltage during increasing flow-rate phase was higher than that in decreasing flow-rate phase. The measurement of pressure drops is useful for verifying the state of water accumulation.

These results indicate that GDL(ID)/SP(F) had a broader range of cell voltage stability

versus the decrease of the air flow rate or the higher Uair, in other words, higher cell voltage robustness, than GDL(F)/SP(SP).

The accumulated water in the GDL led generally to flooding and to decreasing cell voltage. Actually, the Nguyen-type separator, has been studied by many researchers, but the initial high performance deteriorated gradually and irreversibly when liquid water began to remain in the cell during operation at high current density.[7,10] However, the voltage of the GDL(ID)/SP(F) cell in the increasing air flow rate phase was higher than that in the decreasing air flow-rate phase even in the presence of remaining water accumulated during the lower air flow rate.

To clarify whether this discrepancy resulted from the difference in the channel location and to reveal the mechanism, further experimental verifications were carried out. Using 1.0 × 1.0 cm active area cells, I evaluated the effect of the water accumulation on the robustness of the cell voltage under more detailed experimental conditions, comparing the various channel shapes and channel locations.

2-3-2. Experiment by cells with 1.0 × 1.0 cm active area

Polarization. Figure 2-8 shows the comparisons of the polarization curves and the Ohmic resistances between GDL(P)/SP(F), GDL(F)/SP(P), GDL(ID)/SP(F) and GDL(F)/SP(ID). Figure 4b shows a comparison of the diffusion overvoltages at 1.6 A cm^{-2}, which were calculated as the difference of the IR-free voltage and the voltage obtained by the extrapolation of the IR-free Tafel plots between 0.03 and 0.1 A cm^{-2}, i.e., kinetic region, to 1.6 A cm^{-2}. The cell voltages measured for the interdigitated flow channels formed on

both GDL and separator were higher than those for the parallel flow channels at current densities greater than 0.2 A cm^{-2}. The diffusion overvoltages for the cells with interdigitated flow channels were approximately 15 mV lower than those for the cells with parallel flow channels.

These results indicate that the interdigitated channels contributed to the occurrence of forced convection of air, improving the oxygen diffusion to the catalyst layer, consistent with the results for the 3.0 × 9.7 cm cells. During these experiments, an air flow rate of 2.0 NL min^{-1} was supplied, which was sufficiently high oxygen stoichiometry, and corresponding to a 25 m s^{-1} air velocity in parallel channels, for example, and the air was humidified at 100% RH. In the case of larger cells, such as the cell of 3.0 × 9.7 cm active area, there is a variation of cell experimental conditions in the active area, because the oxygen partial pressure decreases from inlet to outlet by both oxygen consumption and vapor generation.[11] In the case of the 1.0 × 1.0 cm cells, the experimental conditions over the whole active area are more uniform.[12] These results indicate that, under the operating conditions of the large area's inlet region, where the flow velocity was high, the oxygen partial pressure was high, and there was no supersaturated water vapor, the interdigitated channels exhibited higher performance than cells with parallel channels.

Effects of relative humidity and oxygen percentage. In order to understand the cell performances assuming the operating conditions at the inlet to outlet regions of the large-area cathode, the effect on the cell performances for various relative humidity and oxygen percentage values were evaluated. The behavior of the cell voltage, the Ohmic resistance and the pressure drop for 100%, 150%, 40% and 15% RH, with oxygen percentage changing from 5 to 20%, is presented below.

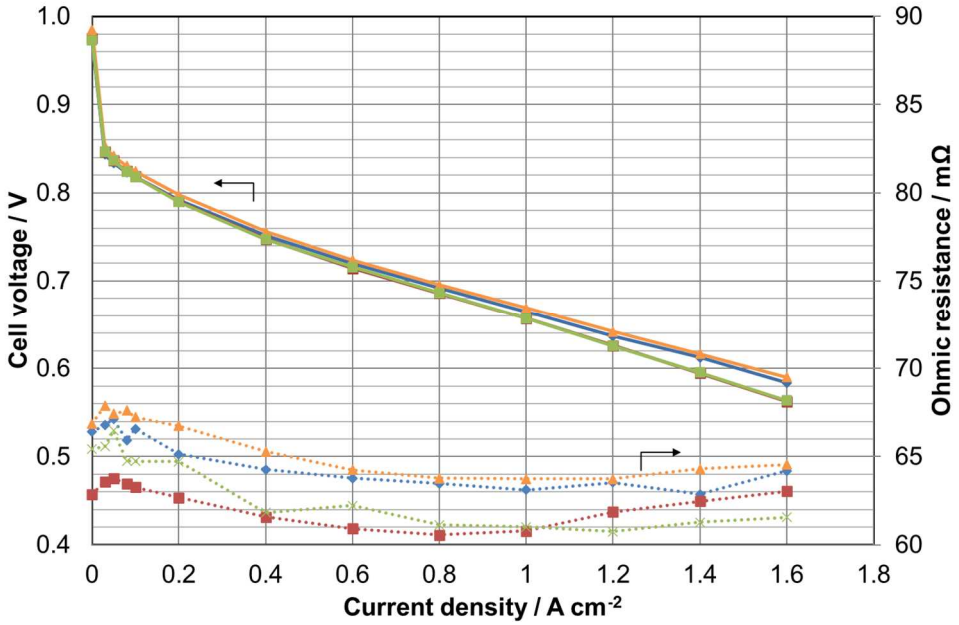

(a) Polarization curves and ohmic resistances

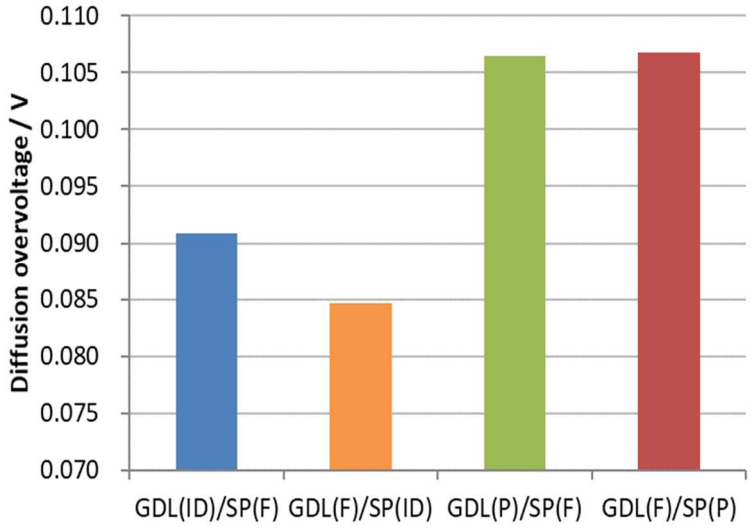

(b) Diffusion overvoltages

Figure 2-8. Comparisons of (a) polarization curves and ohmic resistances from 0 to 1.6 A cm^{-2} and (b) diffusion overvoltages at 1.6 A cm^{-2} among four different cell design in cells of GDL(ID)/SP(F); blue, GDL(F)/SP(ID); orange, GDL(P)/SP(F); green and GDL(F)/SP(P); red, with 1 × 1 cm active area. Each result was averaged from three

Figure 2-9 shows the changes over time in cell voltage, Ohmic resistance, and pressure drop when the oxygen percentage was changed in stages from 20 to 5%. In order to confirm the reproducibility of those data, the oxygen concentration was increased and decreased twice. All cell voltages decreased with decreasing oxygen percentage. In the case of GDL(ID)/SP(F) and GDL(F)/SP(ID), the cell voltages at each oxygen concentration maintained relatively stable values, and the lowest values remained above 0.4 V. In the case of GDL(P)/SP(F) and GDL(F)/SP(P), the values became increasingly unstable and decreased to less than 0.4 V at 5% oxygen percentage. Especially for GDL(P)/SP (F), the cell voltage reached less than 0.3 V, falling below the electronic load threshold to protect the device, and the cell voltage was returned to the open circuit voltage (OCV). These results show that cells with the interdigitated channels were able to maintain a higher cell voltage than cells with the parallel channels at lower oxygen percentages. I propose that the forced convection of air occurring due to the structure of the interdigitated channels is a factor in improving cell voltage stability, similar to the results for the 3.0 × 9.7 cm cells.

Figure 2-10 shows the result of experiments carried out at 150% RH. The cell voltages at each oxygen concentration of GDL(ID)/SP(F) showed relatively stable values, similar to the situation for 100% RH, and the lowest value was also greater than 0.4 V. In the case of GDL(P)/SP(F) and GDL(F)/SP(P), the cell voltages, unlike the results for 100% RH, underwent a steep drop quite often, regardless of the oxygen percentage. The safety control to protect the cells of the evaluation system was frequently activated, and their cell voltages were returned to OCV. In the case of GDL(F)/SP(ID), the safety control was activated less often, but the cell stability was definitely lower than that for the condition of 100% RH. These results under 150% RH conditions showed that the cell voltage

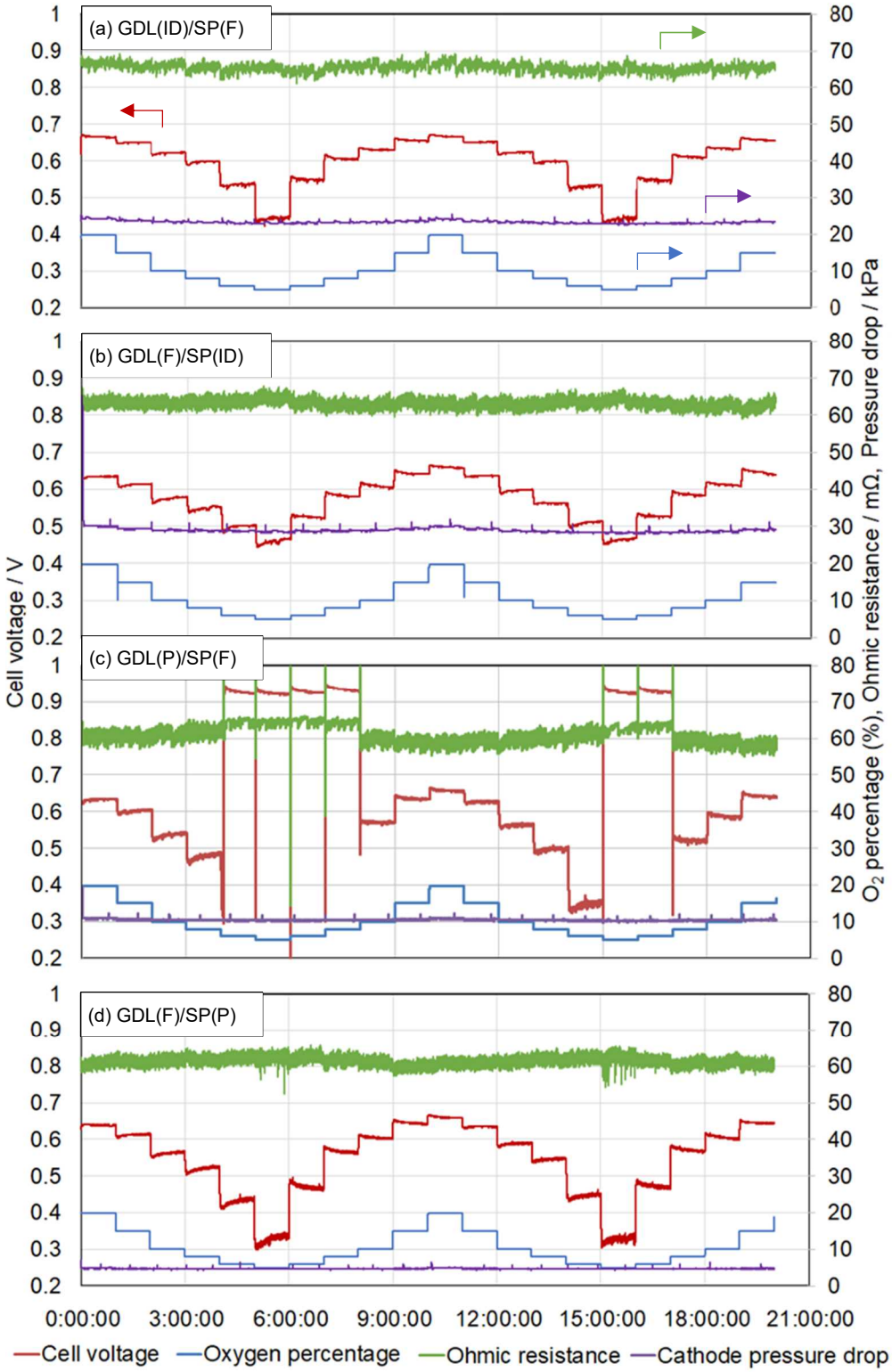

Figure 2-9. Behavior of cell voltages, Ohmic resistances and cathode pressure drops with oxygen percentage change from 20% to 5% at 100% RH and 1 A cm^{-2}. (a) GDL(ID)/SP(F), (b) GDL(F)/SP(ID), (c) GDL(P)/SP(F) and (d) GDL(F)/SP(P).

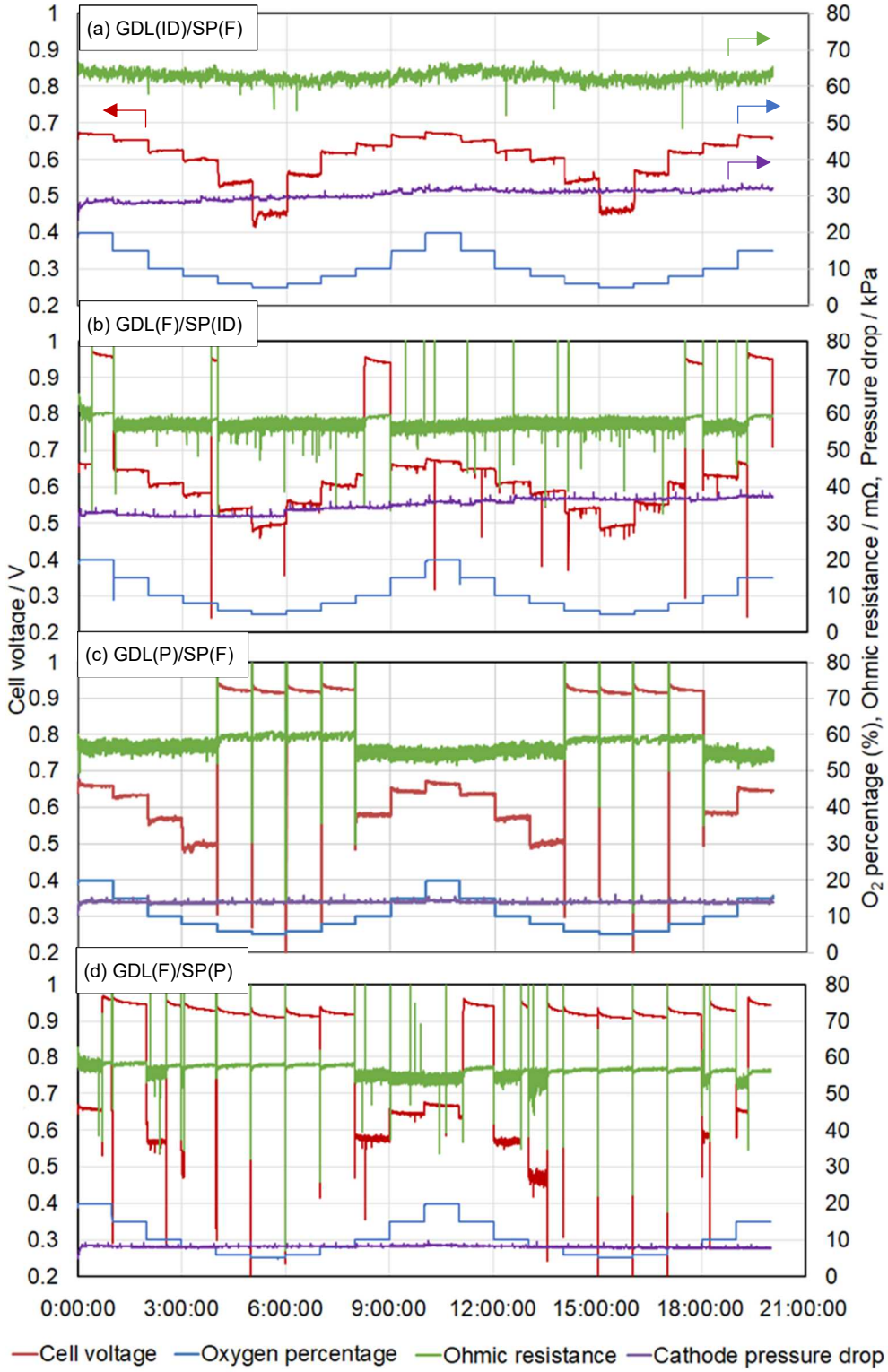

Figure 2-10. Behavior of cell voltages, Ohmic resistances and cathode pressure drops with oxygen percentage change from 20% to 5% at 150% RH and 1 A cm^{-2}. (a) GDL(ID)/SP(F),

stabilities were definitely decreased compared to those for 100% RH, with the exception of GDL(ID)/SP(F). Even with the interdigitated channels, as the GDL(F)/SP(ID) results showed, the cell voltage was less stable when the channels were incorporated on the bipolar-plate side.

At the condition of 150% RH, water vapor-saturated air together with condensed water droplets were supplied to the cathode, because the dew point of the cathode air exceeded the cell temperature. This excess water led to blockage of the oxygen diffusion paths and thus steep voltage drops.[13] Zhou et al. also proposed, even with the interdigitated channels incorporated on the bipolar-plate side, that the excess water in the GDL causes nonuniform air flow and results in the cell voltage drops.[7] On the other hand, GDL(ID)/SP(F) exhibited stable cell voltages in the results for 150% RH, similar to the case for 100% RH. This result indicates that the change in concept of ribs from solid to porous contributed to improve the cell voltage stability even when excess water was supplied to the cathode. I propose that the rib space in the GDL of this design acted as a storage reservoir for excess water, ensuring an effective oxygen supply under excess humidity operation conditions.

Figure 2-11 and 2-12 show results of experiments at 40% and 15% RH. After going through the similar experiment at 150% RH, I proceeded with these evaluations under low humidification conditions in order. A common behavior observed in all cells was that the Ohmic resistance of the cell increased during the reduction of the initial oxygen concentration. Since behaviors of cell voltages, ohmic resistances and pressure drops from experiments at 40% RH is similar to that at 15% RH, I focused the discussed on experimental results at 15% RH as below. The degree of increase (ΔR) was different for each cell, and the values increased in the following order: GDL(ID)/SP(F), ca. 10 mΩ <

GDL(P)/SP(F), ca. 20 mΩ ≤ GDL(F)/SP(P), ca. 25 mΩ << GDL(F)/SP(ID), ca. 50 mΩ, in the case of 15% RH. The increase in cell resistance for GDL(ID)/SP(F) was small, the cell voltage remained stable, and the lowest value at an oxygen concentration of 5% was greater than 0.35 V. In the case of GDL(P)/SP(F) and GDL(F)/SP(P), the cell resistance increased to nearly the same value. The cell voltage frequently fell below the control threshold to protect the cell under conditions of 5% oxygen concentration, and the safety control was activated, returning the cell to the OCV. As the oxygen concentration increased, the cell voltage increased and the stability returned. Similar behavior was shown during the second cycle, demonstrating reproducibility. In the case of GDL(F)/SP(ID), the cell resistance increased to the highest observed value, 140 mΩ in the first cycle of the change in oxygen concentration, compared to other cells. The cell voltage remained higher than the control threshold of 0.3 V. In the second cycle, under the condition of oxygen concentration of 5%, the cell voltage fell below 0.3 V, and the safety control was activated, returning the cell to the OCV.

In these evaluations under low humidification conditions, the cells with the interdigitated channels structure exhibited higher stability in cell voltages. However, in the case of the structure incorporated on the bipolar plates, the cell resistance was the highest value observed. This behavior is presumed to be due to the fact that the forcibly supplied low-humidity gas deprived the membrane and ionomer of water and reduced their water content, as proposed by Zhou et al.[7] In the case of GDL(ID)/SP(F), in which the interdigitated channel structure was incorporated in the GDL, the increase in cell resistance and the decrease in cell voltage were the smallest, and the cell voltage stability was the highest. I propose that this new GDL design was able to maintain high cell performance under the low humidity operation condition by supplying water to the

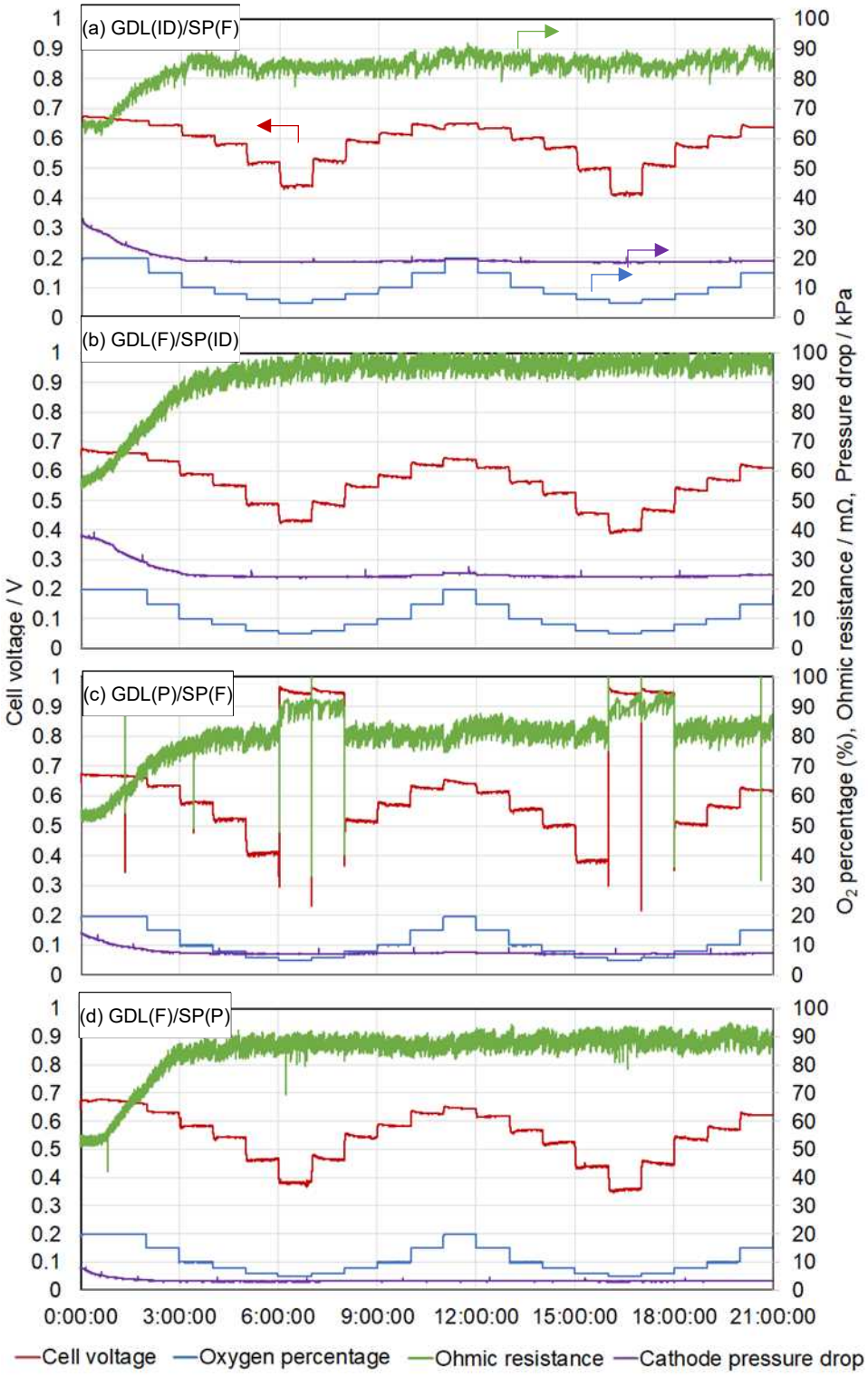

Figure 2-11. Behavior of cell voltages, Ohmic resistances and cathode pressure drops with oxygen percentage changes from 20% to 5% at 40% RH and 1 A cm^{-2}. (a) GDL(ID)/SP(F), (b) GDL(F)/SP(ID), (c) GDL(P)/SP(F) and (d) GDL(F)/SP(P).

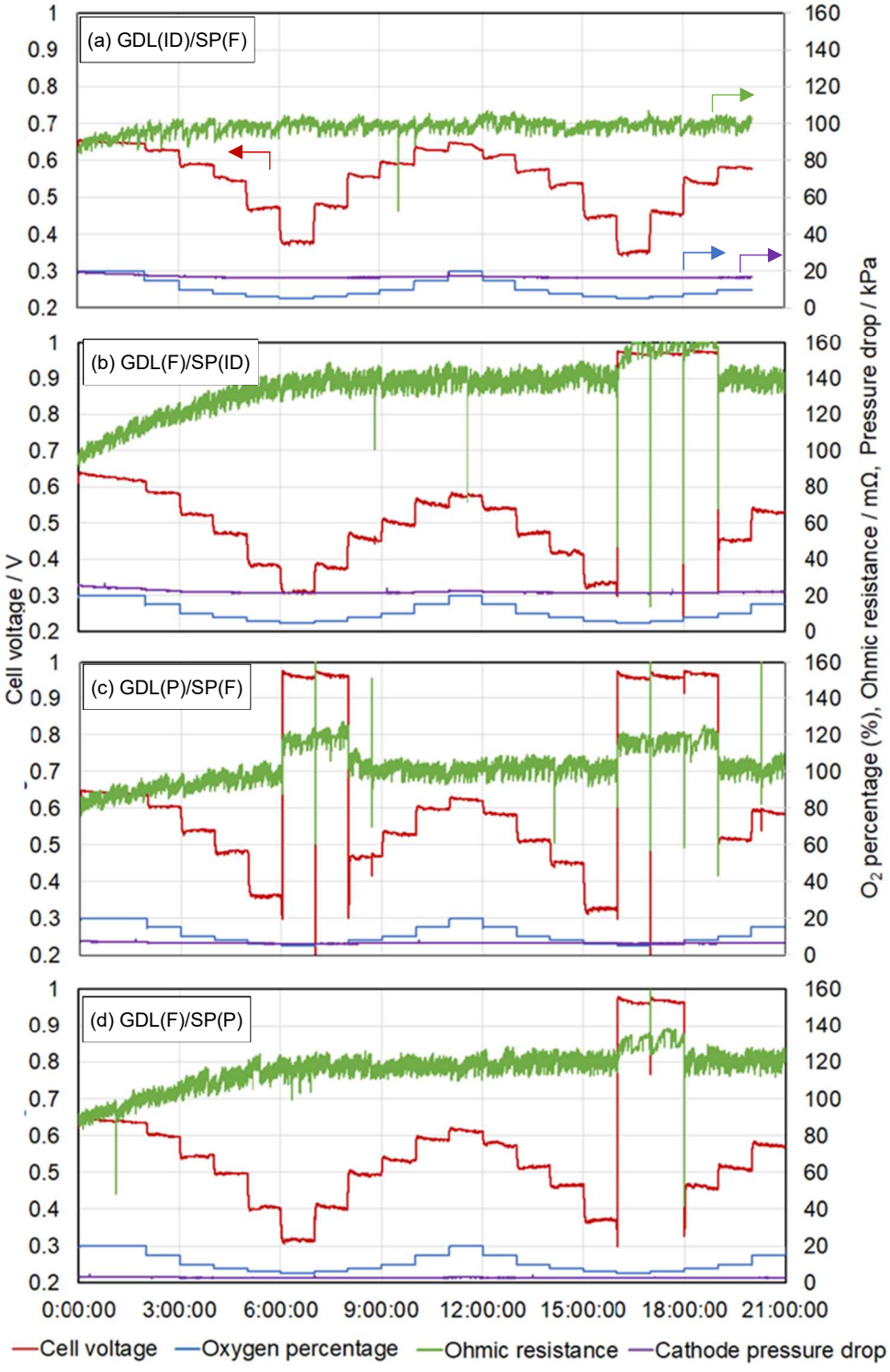

Figure 2-12. Behavior of cell voltages, Ohmic resistances and cathode pressure drops with oxygen percentage change from 20% to 5% at 15% RH and 1 A cm^{-2}. (a) GDL(ID)/SP(F), (b) GDL(F)/SP(ID), (c) GDL(P)/SP(F) and (d) GDL(F)/SP(P).

reaction sites of the catalyst layer from that accumulated in the ribs of the GDL, thus preventing the above-mentioned adverse effects of water deprivation.

Effects of air flow rate. Figure 2-13 shows the changes over time in cell voltage, Ohmic resistance and pressure drop of both cells with interdigitated channels, GDL(ID)/SP(F) and GDL(F)/SP(ID), while the flow rate of the air was varied in stages from 2.0 NL min^{-1} to 0.05 NL min^{-1} at 150% RH. The cycle of the air flow rate was repeated twice, and the second cycle was plotted in order to reduce the impact of conditioning. During of the decreasing phase of the air flow rate, the cell voltage of GDL(ID)/SP(F) was maintained above 0.6 V from 2.0 NL min^{-1} to 0.5 NL min^{-1}. While the cell voltage fell below 0.3 V, the safety control was activated, and the cell was returned to the OCV from 0.4 NL min^{-1} to 0.05 NL/min. During the increasing phase of the air flow rate, after recovered to 0.5 NL/min, the cell voltage of GDL(ID)/SP(F) came stable again and remained above 0.6 V until the air flow rate reached 2.0 NL min^{-1}. During the decreasing phase of the air flow rate, the cell voltage of GDL(F)/SP(ID) frequently fell below 0.3V and the safety control was activated. Also, during the increasing phase of the air flow rate, the cell voltage of GDL(F)/SP(ID) dropped, and the safety control activation occurred during almost all steps of the air flow rate, until it recovered at 2.0 NL min^{-1}. In the case of GDL(F)/SP(ID), the cell voltage was more unstable than that of GDL(ID)/SP(F).

Comparing the pressure drops of the cathode air during the increasing phase of the air flow rate with that of the decreasing phase, it was always higher for the former. In the case of a comparison at 2.0 NL min^{-1}, the pressure drop observed during the increasing phase was 5 kPa higher than that in the decreasing phase, both in GDL(ID)/SP(F) and GDL(F)/SP(ID), where each initial pressure drop was 60 kPa and 70 kPa, respectively, at

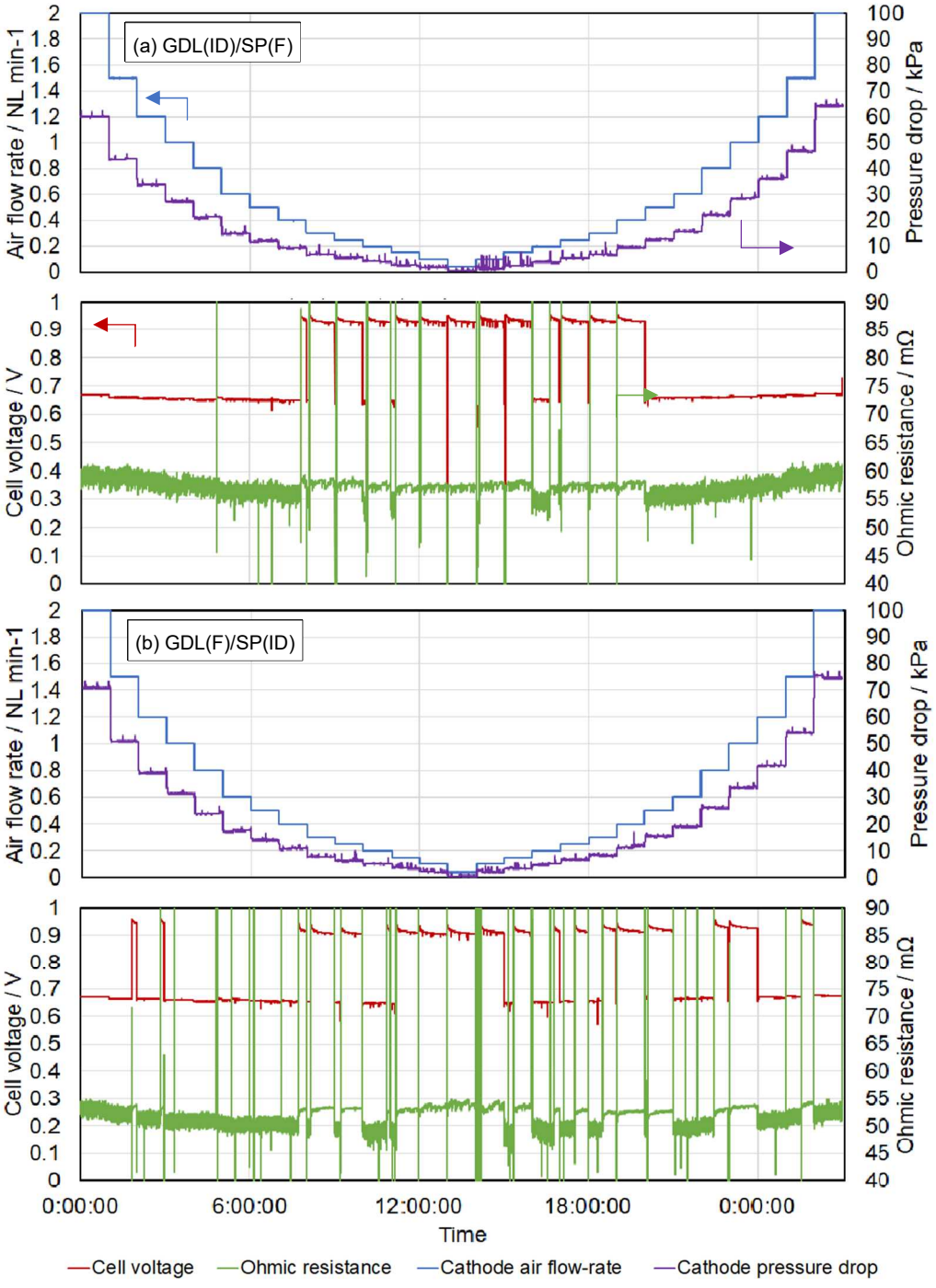

Figure 2-13. Behavior of cell voltages, Ohmic resistances and cathode pressure drops with air flow rate decrease from 2.0 to 0.05 NL min^{-1} and subsequent increase from 0.05 to 2.0 NL min^{-1} at 150% RH and 1 A cm^{-2}. (a) GDL(ID)/SP(F) and (b) GDL(F)/SP(ID).

2.0 NL min^{-1} in the increasing phase. These results indicate that similar amounts of accumulated water were maintained in each of the various types of GDL, regardless of whether the ribs were solid or porous. The cell voltage of GDL(ID)/SP(F) remained stable at flow rates larger than 0.5 NL min^{-1}, in spite of the accumulated water in the GDL, probably due to a larger volume of water-free pores remaining for gas diffusion. Similar to the results of Figure 2-10, which examined the influence of the change of oxygen concentration under 150% RH, the cell voltage of GDL(ID)/SP(F) remained more stable than those of the other cell structures.

In the experiment in which the oxygen partial pressure was varied, shown in Figure 2-10, the total pressure of the supply gas did not change. In this experiment shown in Figure 2-13, the total pressure of the supply gas varied, because the air flow rate was varied. The decrease of the total pressure of the supplied gases weakens the force of convection in the GDL in particular. Therefore, it is expected that a decrease in flow rate will be a more severe condition for cell voltage stability than a decrease in oxygen partial pressure. Even under these harsh test conditions, the fact that the high voltage stability of GDL(ID)/SP(F) was observed clearly shows the superiority of the interdigitated channel structure incorporated in the GDL. These results support my suggestion that the rib space in the GDL of this design acts as a storage reservoir for excess water, ensuring an effective oxygen supply.

Effects of relative humidity. Figure 2-14 shows the changes over time in cell voltage and Ohmic resistance in GDL(ID)/SP(F) and GDL(F)/SP(ID) when the relative humidity conditions of the cathode air were varied rapidly from the intermediate state to the over-humidification state and then gradually to the low humidity state. The relative humidity

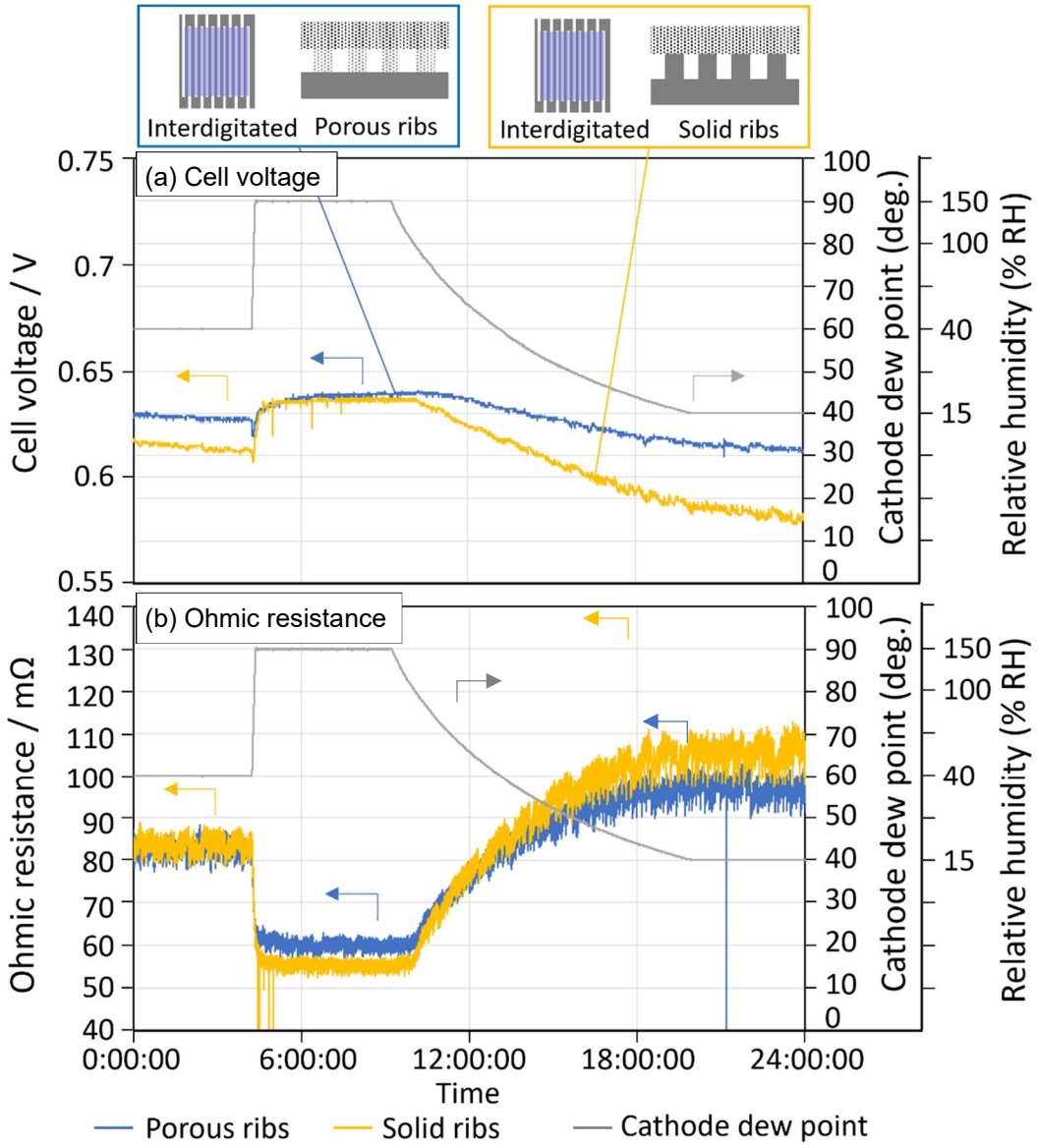

Figure 2-14. Changes over time in (a) cell voltages and (b) Ohmic resistances during relative humidity variations from 60% to 150% and 15% RH in a stepwise fashion. The current density was maintained at 1.0 A cm^{-2} during the experiment.

was varied from 40% RH to 150% RH and then to 15% RH, by changing the dew point of the cathode air from 60 ˚C to 90 ˚C and then 40 ˚C while the cell temperature was maintained at 80 ˚C.

First, when the relative humidity was increased from 40% RH to 150% RH, the Ohmic resistances immediately dropped to ca. 60-57 mΩ, and the cell voltages increased to ca.

0.63 V in both cells. However, while the cell voltage of GDL(ID)/SP(F) remained stable while being held at 150% RH, that for GDL(F)/SP(ID) frequently decreased and became unstable slightly. The comparison results observed under 150% RH conditions, similar to the situation for 150% RH in Figure 2-10 and 2-13, reproduced the result that the GDL(ID)/SP(F), which has the interdigitated channel structure with porous ribs, exhibited a greater ability to prevent performance deterioration due to flooding, because the liquid water generated in the over-humidified state of 150% RH was retained in the porous space of the ribs formed in the GDL.

Next, the details of the changes in the Ohmic resistances and cell voltages of both cells in the gradual decrease from the over-humidification condition of 150% RH to the low humidification state of 15% RH are described. When the humidity started to decrease from 150% RH, the cell voltage of GDL(ID)/SP(F) started to decrease later than that for GDL(F)/SP(ID) whose cell voltage started to decrease immediately. The Ohmic resistances of both cells began to rise after the relative humidity dropped below 100% RH. There was a difference in the rate of increase of the Ohmic resistance of both cells, and the values for GDL(ID)/SP(F) and GDL(F)/SP(ID) at 15% RH reached ca. 95 mΩ and 105 mΩ, respectively. During this time, there was also a difference in the behavior of the cell voltage, and that for GDL(ID)/SP(F) decreased slower than GDL(F)/SP(ID). Upon arrival at 15% RH, the voltage was higher, ca. 0.62V. The cell voltage of GDL(F)/SP(ID) started to decrease lesser than that of GDL(ID)/SP(F) and continued to decrease to 0.58 V or below. In the interdigitated channel structure, gas is forcibly supplied to the GDL and catalyst layer on the contact surface of the ribs.

I suggest that the differences of behavior of both cells were as follows: i) the reason for the delay in the timing to decrease in the cell voltage of GDL(ID)/SP(F) is that, as

suggested in the discussion with experimental result of oxygen percentage characteristics, accumulated water in porous ribs gradually vaporized and diffused to the flat GDL and the catalyst layer at the early stage of humidity decrease, resulting in mitigating the dry out of the cell; ii) the reason why the change in cell voltage and Ohmic resistance of GDL(ID)/SP(F) was gradual is that, in addition to the same mechanism as described in i), since the ribs consist of porous materials, a portion of gas flow from inlet channel to outlet channel diffuse in porous ribs, not diffuse in the flat GDL, which alleviate the discharge of generated water from the flat GDL and the catalyst layer.

2-3-3. Proposed water management mechanisms for solid vs. porous ribs in interdigitated channels

As I suggested in the discussion about effects of relative humidity above, in the case of the GDL(ID)/SP(F) cell, the porosity of the interdigitated ribs causes the gas flows rate to decrease particularly within the GDL region close to the catalyst layer, so it might be expected that the ability to supply oxygen, discharge liquid water and water vapor would weaken. However, I also suggest that this situation is significantly modified in practical operating fuel cells, particularly during high current operation or high humidification conditions, because the porous ribs become effectively less porous due to the presence of accumulated water. The comparison of diffusion overvoltages from polarization results in figure 2-8 is considered to support these suggestions by showing relatively lower diffusion overvoltage with GDL(ID)/SP(F) than cells with parallel flow-channels, despite it was slightly higher than that of GDL(F)/SP(ID).

In addition, a temperature gradient appears unavoidably between the separator and the catalyst layer, because a large amount of heat is generated due to the overpotentials

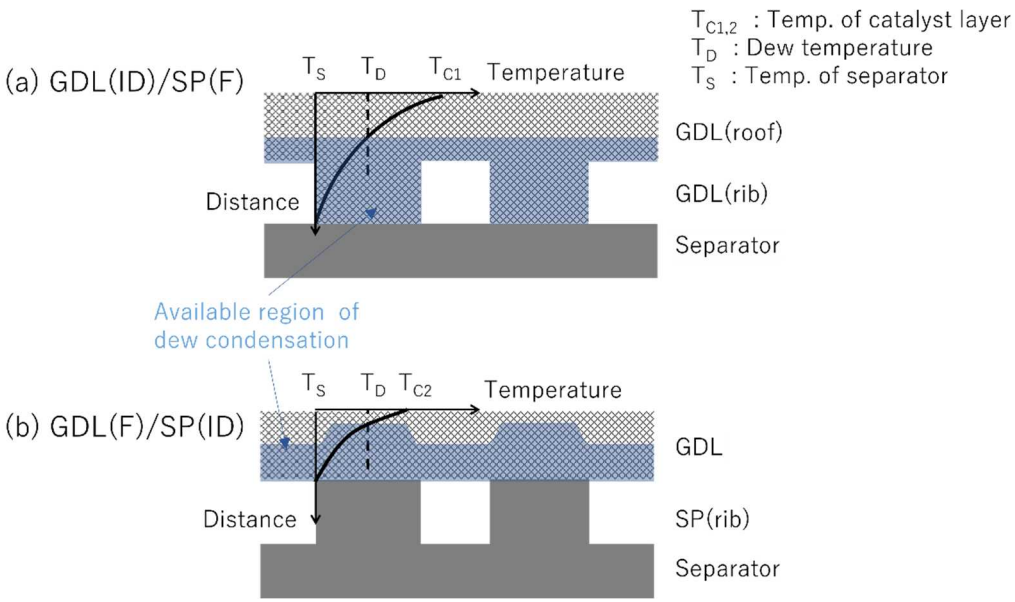

Figure 2-15. Schematic illustrations of predicted dew condensation in the GDL and porous ribs. Solid curves show a temperature gradient along the distance from the interface between the catalyst layer and the GDL to the separator. The blue-colored area of lower temperature than the dew temperature indicates that pores in the GDL and ribs are filled with the accumulated water. The remaining area corresponds to temperatures higher than the dew temperature, so that the water is vaporized in the GDL.

relating to activation, Ohmic resistance and diffusion at the cathode catalyst layer, as shown schematically in Figure 2-15 for GDL(ID)/SP(F) and GDL(F)/SP(ID). It can be assumed that the generated heat becomes large enough to evaporate the generated water or the humidified water into the GDLs, because the thermal conductivity of the GDL was less than 1% of that of the separator material. The temperature (TC1) at the catalyst layer of the GDL(ID)/SP(F) should be higher than that (TC2) of the GDL(F)/SP(ID) at the same current-loading condition, since the former GDL was thicker by a factor of ca. 2, resulting in a smaller cooling effect. The temperature drop for the former is expected to be larger due to the thicker GDL, compared with that of the thinner GDL. As the result, the dew condensation region (below the dew temperature (TD)), for the GDL(ID)/SP(F), would

shift away from the GDL (roof) into the GDL (rib), closer to the separator, thus allowing the GDL (roof) to act as the layer for the reactant/product diffusion. In contrast, a similar amount of dew condensation in the conventional cells such as GDL(F)/SP(P) and GDL(F)/SP(ID) would be expected to occur in their thinner GDLs, resulting in comparatively low gas permeability.

As shown in chapter 2 figure 2-8(b), the diffusion overvoltage of the performance of the GDL(ID)/SP(F) cell was larger than that of the GDL(F)/SP(ID) cell, at 100% RH, examined with the 1.0 × 1.0 cm cell, and also the performance of GDL(ID)/SP(F) was slightly inferior to that of GDL(F)/SP(ID), as shown in figure 2-8(a). However, with the larger-size cells, GDL(ID)/SP(F) is expected to exhibit better performance with smaller diffusion overvoltage than GDL(F)/SP(ID), as shown in previous research by Watanabe et al.[4] Such a superior performance in a practical cell could be obtained as the effects of various operation factors changed along with inlet to outlet.[14] Thus, I was motivated to examine each of the effects independently under different conditions with the partially extracted cell with 1.0 × 1.0 cm active area . The comparison of cell performances with larger-size cells are carried out in Chapter 4.

In this chapter, the appeal of this study is found that not only this good performance by the GDL(ID)/SP(F), but also the improvement of the performance robustness, which was the biggest weakness of the interdigitated structure, considered in general. As an experimental fact, even at 100% RH, as shown in figure 2-9, the cell performance of GDL(ID)/SP(F) was higher than that of GDL(F)/SP(ID). These results can be ascribed to the flooding of the catalyst layer by generated water being suppressed by the accumulation of generated water in the porous ribs of the GDL. The use of decreased oxygen concentration simulates the condition of the downstream flow path in the full-

sized cell. This result indicates that the large electrode suppresses performance degradation even in the downstream stage of the flow channel where the oxygen concentration decreases and improves the uniformity of the reaction distribution in the cell. The above functions are effectively exhibited under the condition of 15% RH shown in Figure 2-12. The conditions at 150% RH in Figure 2-10 clearly contribute to the stability of performance, also. I believe that the reason for this is that the generated water accumulates in the porous ribs of the GDL rather than in the region close to the catalyst layer, thus securing an oxygen supply channel to the latter.

To summarize these results, GDL(ID)/SP(F) demonstrated two advantages compared with GDL(F)/SP(ID), GDL(P)/SP(F) and GDL(F)/SP(P): i) GDL(ID)/SP(F) exhibited lower diffusion overvoltage under polarization, as shown in Figure 2-8, and higher cell voltage at lower oxygen percentage than GDL(P)/SP(F) and GDL(F)/SP(P), as shown in Figure 2-9, while GDL(F)/SP(ID) exhibited similar performances; ii) GDL(ID)/SP(F) exhibited stable cell voltage when supersaturated water vapor was supplied, as shown in Figure 2-10, 2-11 and 2-12, while GDL(F)/SP(ID) exhibited frequent cell voltage drops. Furthermore, GDL(ID)/SP(F) maintained higher cell voltage than GDL(F)/SP(ID) when dry air was supplied.

The first advantage, as previous studies have suggested, [5,6] is considered to be due to the improvement of the oxygen supply to the reaction sites of the catalyst layer by forced convection, which is the unique characteristic of the interdigitated channels. The second advantage is considered to be due to the two mechanisms described below as the result of the change of the ribs from solid to porous. Figure 2-16 shows the predicted water management mechanism for the condition of solid or porous ribs on alternating channels: i) in the case of the conventional interdigitated cell, all of the supplied air passes through

the GDL area under the ribs, while some portion of the air passes through the porous ribs in GDL(ID)/SP(F). As a result, GDL(ID)/SP(F) is able to prevent the dry-out of the GDL and the reaction sites of the catalyst layer; ii) the change in the ribs from solid to porous increases the capacity of the porous structure. This porous structure acts as a storage reservoir when supersaturated water is supplied to the cell, ensuring an effective oxygen supply to the reaction sites. Furthermore, the accumulated water in the porous ribs is supplied to the GDL and the reaction sites under conditions with dry air flow, ensuring the maintenance of high cell performance.

A previous study by M. Nasu et al. is also considered to support the proposed model.[15] In that study, the amount of accumulated water in the porous ribs was larger than that in the flow channels when the newly designed cell was operated under the experimental condition with a current density of 3.0 A cm^{-2} and a relative humidity of 73% RH both in anode and cathode, which was measured by neutron imaging. I have successfully visualized the fact that generated water is accumulated in the porous ribs of the GDL near the exit. These results indicate that the voids in the porous ribs imbibe the liquid water when the excessive water is generated, and this phenomenon is considered to be repeated in the experiments of the present study under the conditions of the supersaturated water supply. In the area where the oxygen concentration near the exit is lower than that near the entrance and flooding is more likely, the water storage function of the porous ribs is demonstrated.

Also, the influence of the temperature distribution inside the cell can be inferred, specifically, that the temperature of the rib part near the separator is maintained low, but that near the catalyst layer is maintained high because the heat conduction of the porous rib part is low. It is thought that this leads to condensation of the generated water in the

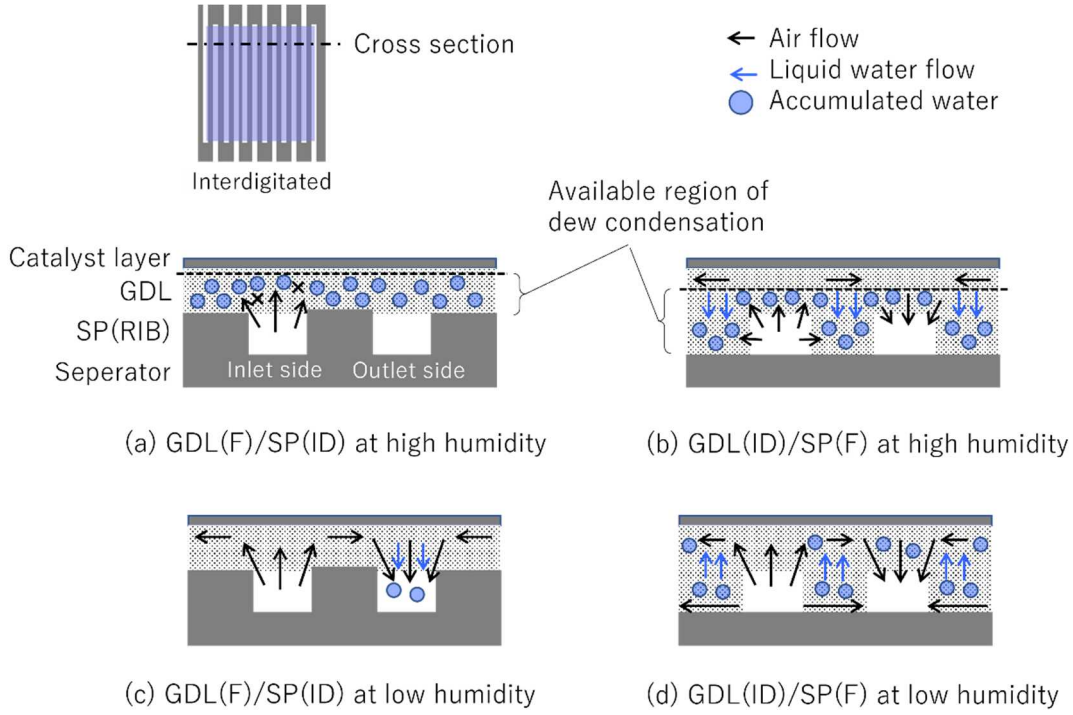

Figure 2-16. Schematic illustrations of predicted behavior of supplied air and liquid water in the GDL and porous ribs to explain the higher cell-performance stability of GDL(ID)/SP(F) by the difference of water management in the porous ribs at high and low relative humidity. (a) GDL(F)/SP(ID) at high humidity, (b) GDL(ID)/SP(F) at high humidity, (c) GDL(F)/SP(ID) at low humidity and (d) GDL(ID)/SP(F) at low humidity.

ribs and accumulation of water. This effect prevents water from accumulating in the porous rib part near the catalyst layer in a high humidity state, and also has the effect of suppressing the drying of the catalyst layer in a low humidity state, contributing to the stability of the cell performance under the severe conditions described above. To prove the validity of these proposed mechanisms, it is necessary to test the model further with imaging and visualization techniques which are carried out and shown in Chapter 3. In any case, as mentioned above, one of the appealing aspects of the new porous ribs concept is the discovery that it leads to significantly improved oxygen supply to the catalyst layer.

2-4. Conclusions

A new gas flow design consisting of a flat metal separator and a GDL with gas-flow channel on its surface was fabricated with interdigitated flow channels and incorporated into single cells. The performance of this newly designed cell was investigated with variations of cell experimental conditions, which included oxygen percentage, air flow rate and relative humidity in the cathode, and compared with conventional-design cells. The results of the experiments clarified the advantages of the newly designed cell from three viewpoints, as follows: i) the newly designed cell recreated the enhanced cell performance of the traditional interdigitated cell, which is higher than that of the parallel flow channel, due to the strong pumping of oxygen to the catalyst layer because of the forced convection in the GDL; ii) the newly designed cell exhibited cell voltage stability under conditions with supersaturated water in the cathode, while a conventional interdigitated cell exhibited frequent cell voltage drops; iii) the newly designed cell was able to maintain its cell performance under conditions with dry air flow, while the traditional interdigitated cell exhibited faster and larger cell-voltage decreases and Ohmic resistance increases. The results of ii) and iii) are proposed to stem from the improved water management within the cell, brought about by the effect of providing a water reservoir in the porous ribs by changing the rib material from solid to porous, eliminating the shortcomings of traditional interdigitated solid flow channels.

In this chapter, cells with an active area of 1.0 × 1.0 cm were adopted to investigate the impact of the variations of detailed experimental conditions on cell performance. The variations of the experimental conditions were established from the actual conditions, based on larger active-area cells, from inlet to outlet. As a result, the newly designed cell exhibited performance superior to that of conventional design cells under all experimental

conditions. As cells with 3.0 × 9.7 cm active area showed in Figure 4, the adaptation of the flow design of GDL(ID)/SP(F) to full-size cells, such as those for vehicles, predict specific advantages compared with the conventional flow design.

In the next Chapter 3, based on these results, I will verify the predicted mechanisms of the newly designed cell to improve performance by visualizing the water distributions and dynamics in the porous ribs and the GDL during cell operation and comparing the results with those for conventional cell designs.

2-5. References

1. K. Ito, K. Ashikaga, H. Masuda, T. Oshima, Y. Kakimoto and K. Sasaki, Estimation of flooding in PEMFC gas diffusion layer by differential pressure measurement, *Journal of Power Sources*, Vol. 175, Issue 2 (2008) 732-738
2. H. Li, Y. Tang, Z. Wang, Z. Shi, S. Wu, D. Song, J. Zhang, K. Fatih, J. Zhang, H. Wang, Z. Liu, R. Abouatallah and A. Mazza, A review of water flooding issues in the proton exchange membrane fuel cell, *Journal of Power Sources*, Vol. 178, Issue 1 (2008) 103-117
3. S. Sakaida, Y. Tabe, T. Chikahisa, K. Tanaka and M. Konno, Study on PEFC Gas Diffusion Layer with Designed Wettability Pattern Tolerant to Flooding, *The Electrochemical Society Transactions*, Vol. 86, No. 13 (2018) 111
4. M. Watanabe, H. Yanai and M. Nasu, Development and Analysis of an Innovative Flat-Metal Separator Integrating the GDL with Gas-Flow Channels as PEFC Components, *Journal of The Electrochemical Society*, Vol. 166, No. 7 (2019) F3210
5. T. V. Nguyen, A Gas Distributor Design for Proton-Exchange-Membrane Fuel Cells, *Journal of Electrochemical Society*, Vol. 143, No.5 (1996)

6. D. L. Wood, III, Jung S. Yi. and T. V. Nguyen, Effect of direct liquid water injection and interdigitated flow field on the performance of proton exchange membrane fuel cells, *Electrochimica Acta*, Vol. 43, No. 24, 3795 (1998)
7. A. D. Le, B. Zhou, A generalized numerical model for liquid water in a proton exchange membrane fuel cell with interdigitated design, *Journal of Power Sources*, Vol. 193, Issue 2 (2009), 665-683
8. H. Tomioka, Y. Hashimasa and N. Yoshimura, JARI Standard Single Cell Testing Protocol, *JARI research journal*, Vol. 28(7) (2006) 247-252
9. W. Vielstich, H. A. Gasteiger, A. Lamm, Handbook of fuel cells fundamentals, technology and applications, Fuel cell technology and applications, *John Wiley & Sons Ltd.*, 3 (2003) 597
10. T. V. Nguyen and M. W. Knobbe, A liquid water management strategy for PEM fuel cell stacks, *Journal of Power Sources*, Vol. 114, 70 (2003)
11. H. Meng and CY. Wang, Large-scale simulation of polymer electrolyte fuel cells by parallel computing, *Chemical Engineering Science*, Vol. 59, Issue 16 (2004) 3331-3343
12. P. Oberholzer and P. Boillat, Local Characterization of PEFCs by Differential Cells: Systematic Variations of Current and Asymmetric Relative Humidity, *Journal of The Electrochemical Society*, No. 161, Issue 1 (2013) F139
13. M. Gerard, J. P. Poirot-Crouvezier, D. Hissel and M. C. Pe´ra, Oxygen Starvation Effects on PEMFC Durability, *Proceeding Paper of International Conference on Fuel Cell Science, Engineering and Technology*, No. FuelCell2010-33173 (2010) 593-660
14. G. Zhang, X. Xie, B. Xie, Q. Du and K. Jiao, Large-scale multi-phase simulation of proton exchange membrane fuel cell, *International Journal of Heat and Mass*

Transfer, Vol. 130 (2019) 555-563

15. M. Nasu, H. Yanai, N. Hirayama, H. Adachi, Y. Kakizawa, Y. Shirase, H. Nishiyama, T. Kawamoto, J. Inukai, T. Shinohara, H. Hayashida and M. Watanabe, Neutron imaging of generated water inside polymer electrolyte fuel cell using newly-developed gas diffusion layer with gas flow channels during power generation, *Journal of Power Sources*, Vol. 530, (2022) 231251

Chapter 3 Validation of the Proposed Mechanisms on the Performance Stability Improvement with newly designed cell

3-1. Introduction

In Chapter 2, I constructed the newly designed cells (1.0 × 1.0 cm active area) with an interdigitated flow channel formed on the GDL and also a conventional interdigitated cell with a channel formed on the separator.[1] The cell of 1.0 × 1.0 cm active area was applied as a partially extracted model, i.e., with a very small variation of operating conditions, in comparison with a practical cell with larger active area, in order to investigate the correlation of the channel design, operating conditions and cell performance in greater detail.[2,3] The performances of these cells were compared under various conditions, including variations of the relative humidity (RH), oxygen percentage and gas flow rate. The experimental results verified the effect of incorporating interdigitated channels in the porous GDL on alleviating the disadvantages of the conventional interdigitated channel design, with the latter formed on the separator, specifically under high and low humidity conditions[4,5,6]. These results showed that the cell with the interdigitated flow channel on the GDL exhibited a more stable voltage than the conventional interdigitated flow channel cell during operation at the high relative humidity of 150% RH, which was calculated from the dew point of the supplied air at 90 °C and the cell temperature of 80 °C, based on the definition of the relative humidity as the ratio of the water vapor pressure to the saturation water vapor pressure over water at the gas temperature.[7,8] Furthermore, there was a smaller decrease of the voltage under dry conditions (15% RH, where the dew point of the supplied air was 40 °C) than that for the conventional cell.

I proposed that the mechanism of the performance stability in the newly designed interdigitated cell derives from the existence of the porous ribs, which prevent both flooding and drying. Specifically, the porous ribs are considered to play different roles in the respective conditions of excess water and insufficient water. Under excess water conditions, (1) the porous ribs take up the excess water, alleviating water accumulation in the flat region of the GDL, which would interrupt oxygen mass transport to the catalyst layer; and (2) the porous ribs allow the temperature to increase in the GDL because of its lower thermal conductivity (less than 1/100 compared to values for solid ribs with graphitic carbon or met al.). Under insufficient water conditions (dry gas supply), (3) the water accumulated in the porous ribs gradually diffuses to the flat region of the GDL and compensates for the low humidity in the catalyst layer and the membrane, and (4) in the porous ribs without accumulated water, a portion of the supplied gas is able to pass through the ribs, which alleviates the removal of water remaining in the flat region of the GDL. To test these predictions, it would be desirable to examine in more detail the internal phenomenon in the porous ribs, as follows: (1) does water accumulate in the porous ribs under excess water conditions; (2) is the temperature of the flat region of the porous-rib-GDL cell higher than that in the conventional cell with solid ribs, and is it higher than the dew point in specific spatial areas; (3) can the amount of water that is accumulated in the porous ribs gradually decrease during a relative humidity decrease; and (4) is the amount of water remaining in the flat region of the porous-rib-GDL more than that in the conventional cell, and is the flow rate of the supplied gas in the flat region of the porous-rib-GDL cell lower than that in the conventional cell.

In another previous study, M. Nasu et al. visualized the water distribution in the newly designed cell with interdigitated flow channels on the GDL by means of neutron imaging,

which was conducted at the Materials and Life Science Experimental Facility (MLF) of the Japan Proton Acceleration Research Complex (J-PARC).[9] The measured water thickness at positions on the ribs was approximately 0.1 mm thicker than that of the channels at the down-stream side of the gas flows with the operating conditions of 73% RH and 3.0 A cm^{-2}. This result indicated the possibility of water accumulating in the porous ribs at high humidity, besides water existence in the porous ribs was not directly observed. As further verification, the direct observation of water accumulation in the porous ribs would be desirable. In addition, since the proposed mechanism is contributed by changing behaviors of the temperature distribution and the gas flows in the GDL, it is also necessary to visualize these behaviors to validate the proposed mechanism. Visualization of temperature distributions in a cell has been desired to understand mechanisms of cell performances, and many researchers have proposed various techniques to reveal them, such as micro scale thermocouples and laser sensing.[10,11,12] However, these techniques are almost unapplicable to this research because the temperature distribution along the distance from the MEA to the separator is hardly measured which is necessary for the validation. On the other hand, the temperature distribution in operating cells is also commonly analyzed by numerical simulations, as well as the gas flows distribution.[13-16]

In this chapter, in order to establish whether the predictions described above, from (1) to (4), actually occur in the operating cell, I analyzed the internal water distribution in the cell under operating conditions by use of the X-ray imaging technique. In addition, I calculated the temperature distribution in the GDL and the gas flows distribution of cathode gas, by means of numerical simulations with a three-dimensional model, and then compared the results for a cell incorporating the new design and a conventional cell.

3-2. Experimental and Numerical Simulation

3-2-1 X-ray imaging

Several operando techniques have been developed to visualize the water distribution inside a fuel cell, including NMR imaging, neutron imaging and soft X-ray imaging.[17-20] Since X-ray imaging has an advantage in terms of the temporal resolution compared to the other technique[19], I focused on this analysis as the most suitable for the observation of water behavior continuously during relative humidity variations. In the present study, X-ray imaging was carried out with an X-ray microscope system which consists of an X-ray source (TX-300, Tungsten target, Mars Tohken Solution) and a detector (C15926-01, Hamamatsu Photonics). The intensity of the transmitted X-ray beam from the source through the sample was measured with the detector. The tube voltage was 60 kV, scan time was 0.5 s, and 10 scans were averaged for each image. This imaging system can generate low-energy X-rays in laboratories, without the need for a large-scale synchrotron source.

Figure 3-1 shows an overview of the cells with interdigitated channels on the GDL with porous ribs (GDL(ID)/SP(F)) and with interdigitated channels on the separator with solid ribs (GDL(F)/SP(ID)) for X-ray imaging. Through-plane observation, which visualizes the membrane-electrode assembly (MEA) in the thickness direction in an X-ray image by X-ray transmission through the MEA, was performed. The MEA was sandwiched by carbon separators and sealed by polypropylene gaskets. These materials were selected from the point of view of their high X-ray transmissivity. The active area of X-ray imaging cells was 0.5 × 0.8 cm, and the length toward the cathode gas flow was 0.5 cm to have sufficient signal intensity from X-ray transmission. The specifications of the X-ray

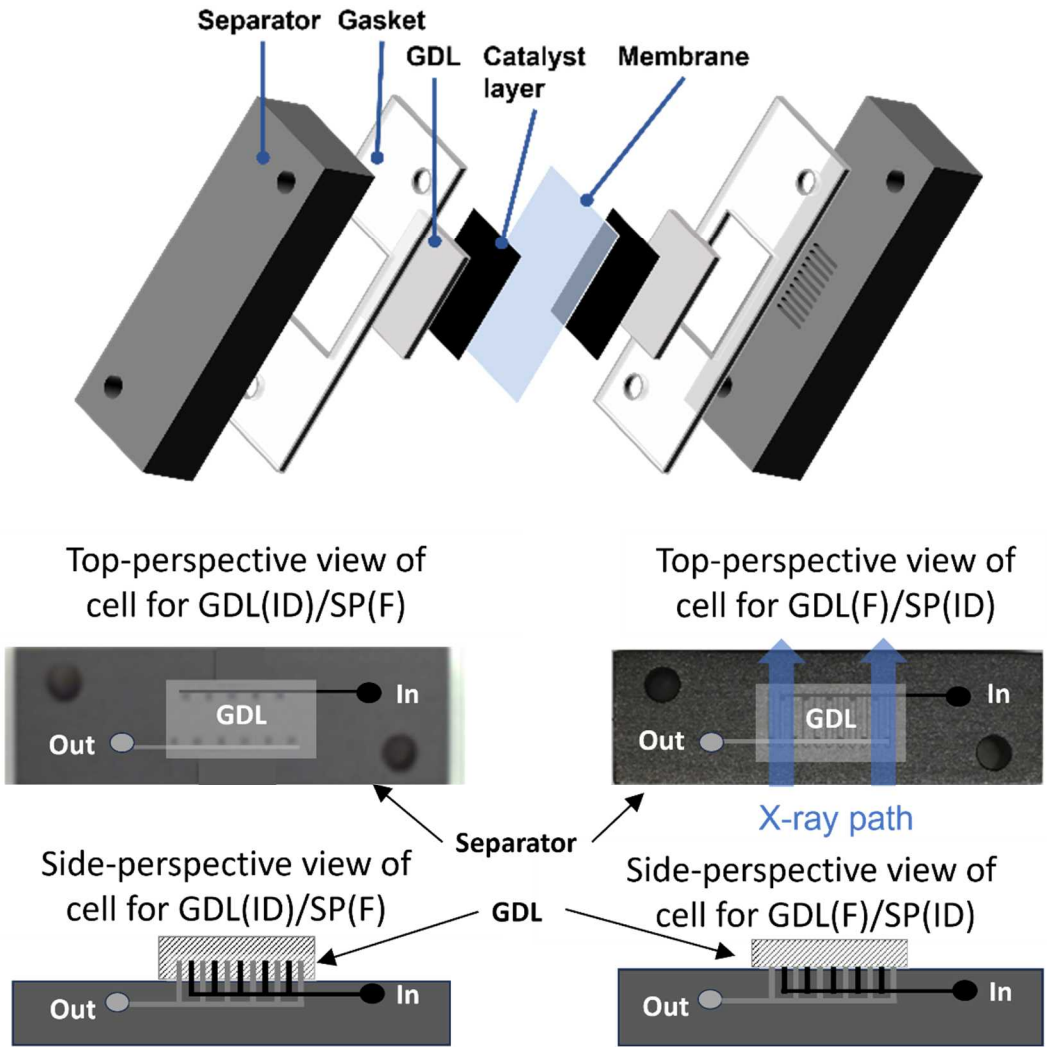

Figure 3-1. Schematic images of X-ray imaging model. GDL(ID)/SP(F) and GDL(F)/SP(ID) were set in each single cell for the visualization of distribution states of liquid water by X-ray imaging. Interdigitated channels consisted of 5 inlet and 6 outlet flow channels with 0.4 mm (W), 0.18 mm (D), forming a rib with a 0.7 mm pitch. Observation area of water distribution images was 0.5 × 0.8 cm side of the cell, vertical to the flow channels.

imaging cells were the same as those for the previously reported experiments with 1.0 × 1.0 cm cells, including the properties of the GDL with porous ribs, as shown in Table 3, with the exception of three points, as follows: (1) all materials were cut to fit the 0.5 × 0.8 cm active area; (2) the membrane was NRE212 (Chemours); and (3) the Pt loading was 0.2 mg cm-2 on both anode and cathode.

Table 3-1 shows the operating conditions of the X-ray imaging cell. To observe the distribution and diffusion of water not only at steady state with high and low humidification conditions but also during transient states with humidification condition changes, the relative humidity in the cell was maintained at 120% RH at first and then was decreased to 40% RH continuously. The relative humidity was calculated from the cell temperature and dew point, as already mentioned above. The oversaturation state of 120% RH was realized by utilizing a lower temperature of the cell than the dew point, similar to the strategy used in the testing of the 1.0 × 1.0 cm cells. During this humidity change, the The cell temperature was raised from 33 to 55 ℃ maintaining a dew point of around 36℃ to change the humidity from 120 to in order to maintain a stable level of 40% RH. X-ray images were obtained repetitively at 6.9 s intervals during the cell operation, which was sufficient time resolution to observe the transient process by relative humidity change conducted in this study.

Table 3-1. Operating conditions of X-ray imaging cell

Current density	0.5 A cm^{-2}
Cell temperature	From 33 to 55 ℃
Relative humidity at inlet (Corresponding dew point /cell temperature)	From 120% to 40% RH (36 ℃ / 33 ℃ at 120% RH, 36 ℃ / 55 ℃ at 40% RH)
Flow rate (Hydrogen /Air)	0.15 / 0.4 NL min^{-1}

Liquid water in the cell absorbs X-ray and the existence of liquid water results in a lower signal intensity in the X-ray image. Therefore, the liquid water content distribution in the cell can be visualized by taking the difference of the signal intensity in each pixel between an image obtained during cell operation and the image in the initial state. This study

focuses on water content in the cathode GDL. Image matching and shifting focused on the cathode GDL were conducted to reduce the effect of image drift caused by membrane swelling under different humidity conditions. In addition, a median filter was used to reduce the effect of noise.

3-2-2 Numerical simulations

As mentioned in the Introduction, the visualizations of the temperature and gas flow distributions in the GDL are required to reveal the mechanism of the performance improvement in the newly designed cell. In-situ measurements of the temperature distribution in operating cells are typically carried out with thermocouples, but the temperature distribution in three dimensions, especially in the GDL, is difficult to measure with this approach. The distribution of the gas flows rate in the GDL pores is also difficult to measure. In the present study, the temperature and the gas flows in the GDL are calculated by numerical simulation of the operating cell.

To calculate the temperature distribution in the operating cell, the computational fluid dynamics (CFD) software package STAR-CCM+ ver. 13.06 was applied by combination with electrochemical solutions. Since it is necessary to simulate the diffusion of both gas flow and liquid flow, a Eulerian multiphase mixture model (EMP) was adopted.[10] In EMP, the equation of the energy conservation between two phases, liquid water and vapor in this study, is described below (see List of Symbols below):

List of symbols

A_s	surface area of droplet, m^2
B	Spalding transfer number
C_p	specific heat, J $(kg\text{-}K)^{-1}$
C_w	concentration of hydronium ion, kmol m^{-3}
D_p	diameter of water droplet, m
D_w	water diffusion coefficient, m^2 s^{-1}
E	total energy, eV
EW	equivalent weight of membrane, kg $kmol^{-1}$
E_{eq}^{ox}	equilibrium potential, V
F	Faraday constant, C mol^{-1}
$\mathbf{f}$	body force vector, m s^{-2}
g^*	mass transfer conductance, kg $(m^2\text{-}s)^{-1}$
H	total enthalpy, J kg^{-1}
h_g (T)	entropy of aphase g at T, J K^{-1}
i	current density, A cm^{-2}
i_0	exchange current density, A/cm^2
i_0^{ref}	reference exchange current density, A/cm^2
k	thermal conductivity, J $(s\text{-}m\text{-}K)^{-1}$
k_{eff}	Effective thermal conductivity, J $(s\text{-}m\text{-}K)^{-1}$
L	heat of evaporation, J kg^{-1}
m_{gl}	mass transfer rate from phase l to phase g, kg s^{-1}
$\dot{m}$	mass transfer rate, kg s^{-1}
N_d	electro-osmotic drag coefficient, m^3 $kmol^{-1}$
P	pressure, Pa
P_0^{atm}	absolute pressure, Pa
Q_{gl}	amount of transferred heat from phase l to phase g, J s^{-1}
$Q_g^{(gl)}$	amount of transferred heat from interface of phase g and phase l to phase g, J s^{-1}
R	gas constant, J $(K\text{-}mol)^{-1}$
S	energy source term, J s^{-1} T temperature, K
V	volume, m^3
$\mathbf{v}$	velocity, m s^{-1}

List of symbols

Greek

α	volume fraction
α^{eff}	charge transfer coefficient
Γ	phase transfer of water
κ	sorption rate, m s^{-1}
λ_{mem}	moisture ratio, m^3 $kmol^{-1}$
ρ	density, kg m^{-3}
μ_t	turbulent viscosity, Pa-s
σ_t	Prandtl number of turbulent heat diffusivity
σ_{mem}	membrane conductivity, S m^{-1}
η	overpotential, V
Φ	potential, V

Subscripts

a	anode
c	cathode
c(g)	vapor
fluid	fluidic regions in fuel cell
g	gas
l	liquid
gl	interface between phase g and phase l
mem	membrane

$$\frac{\partial}{\partial t}\int_V \alpha_{\mathrm{g}}\rho_{\mathrm{g}}E_{\mathrm{g}}dV + \oint_A \alpha_{\mathrm{g}}\rho_{\mathrm{g}}H_{\mathrm{g}}\mathbf{v}_{\mathrm{g}}\cdot d\mathbf{a} = \oint_A \alpha_{\mathrm{g}}k_{eff,\mathrm{g}}\nabla T_{\mathrm{g}}d\mathbf{a} + \oint_A \mathbf{T}_{\mathrm{g}}\cdot\mathbf{v}_{\mathrm{g}}da + \int_V \mathbf{f}_{\mathrm{g}}\cdot \mathbf{v}_{\mathrm{g}}dV + \int_V \sum_{\mathrm{l}\neq\mathrm{g}} Q_{\mathrm{gl}}dV + \int_V \sum_{(\mathrm{g,l})} Q^{(\mathrm{g,l})}dV + \int_V S_{\mathrm{g}}dV + \int_V \sum_{\mathrm{l}\neq\mathrm{g}}\left(m_{\mathrm{gl}} - m_{\mathrm{lg}}\right)h_{\mathrm{g}}\left(T_{\mathrm{gl}}\right)dV \quad (1)$$

Effective thermal conductivity $k_{eff,g}$ is described as follows:

$$k_{eff,\mathrm{g}} = k_{\mathrm{g}} + \frac{\mu_{t,\mathrm{g}}C_{p,\mathrm{g}}}{\sigma_{t,\mathrm{g}}} \quad (2)$$

The hydration of the membrane affects the simulation results such as the conductivity of the membrane and the thermal distribution in the cell. In this study, the amount of water contained in the MEA was represented by the concentration of the hydronium ion C_w. The equation for hydronium ion transport in the MEA is as follows:

$$\frac{\partial c_w}{\partial t} + \nabla \cdot \left(-D_w \nabla c_w + \frac{n_d}{F}\boldsymbol{i}\right) = S \qquad (3)$$

Hydronium ion concentration affects the moisture ratio λ_{mem} and the membrane conductivity σ_{mem}, as follows:

$$\lambda_{mem} = \frac{EW}{\rho_{mem}} c_w \qquad (4)$$

$$\sigma_{mem} = (0.5139\lambda_{mem} - 0.326) exp\left[1268\left(\frac{1}{303} - \frac{1}{T_{mem}}\right)\right] \qquad (5)$$

Phase transfer of water into the membrane by sorption $\Gamma_{ij,w}$ was calculated based on the relationship with the sorption rate κ and phase volume fraction α as follows:

$$\Gamma_{ij,w} = -\kappa_{ij}\alpha_j\left(c_w - c_{ij,eq}\right) \qquad (6)$$

Here, subscript i is species and j is sorption transport into the solid from either the vapor or liquid phase.

Calculations of the electrochemical reactions, including the hydrogen oxidation reaction (HOR) and oxygen reduction reaction (ORR) were based on the Butler-Volmer equation.

$$i = i_0\left[exp\left(\alpha_a^{eff}\frac{F}{RT}\eta\right) - exp\left(-\alpha_c^{eff}\frac{F}{RT}\eta\right)\right] \qquad (7)$$

Overvoltage η and exchange current density i_0 are described as follows.

$$\eta = -\Phi_{solid} - \Phi_{fluid} - E_{eq}^{ox} \qquad (8)$$

$$i_{0,a} = i_{0,a}^{ref} \left(\frac{P_{H2}}{P_0^{atm}}\right)^{0.5} \quad (9)$$

$$i_{0,c(g)} = i_{0,c(g)}^{ref} \left(\frac{P_{O2}}{P_0^{atm}}\right)^{0.5} \left(\frac{P_{H2O}}{P_0^{atm}}\right)^{0.5} \quad (10)$$

Since the evaporation and condensation of water occur in the GDL pores, leading to thermal production and absorption, respectively, the Spalding evaporation / condensation model was adopted in the EMP to evaluate the effect on the temperature in the GDL.[11] In the Spalding model, the mass transfer rate m_g, transference number B and mass transfer conductance g^* are described as follows.

$$\dot{m}_g = -g^* A_s \ln(1 + B) \quad (11)$$

$$B = \frac{C_p(T_g - T_d)}{L} \quad (12)$$

$$g^* = \frac{k_g Nu}{C_{p,g} D_p} \quad (13)$$

From these equations, the temperature at each mesh was calculated as the summation of transferred heat from adjacent meshes, Joule's heat and evaporation or condensation heat at that point.

Figure 3-2 shows the calculation models of the porous ribs and solid ribs. The active area of the model was taken to be 1.0 × 1.0 cm, and the other geometrical dimensions and material properties were determined to match the experimental model described in Chapter 2. Geometrical parameters for the calculations are listed in Table 3-2, and parameters of the cathode flow channel design and operating conditions are shown in Table 3-3. As M. Nasu et al. showed by neutron imaging, water accumulation in the GDL pores tends to concentrate in the area around down-stream side of interdigitated flow-channel. To visualize the temperature and the gas flows distributions and discuss about the correlation of these factors and the cell performance, I focused on the analysis in the

cross-section area of A-A' in figure 3-2 which located around down-stream side of the cell.

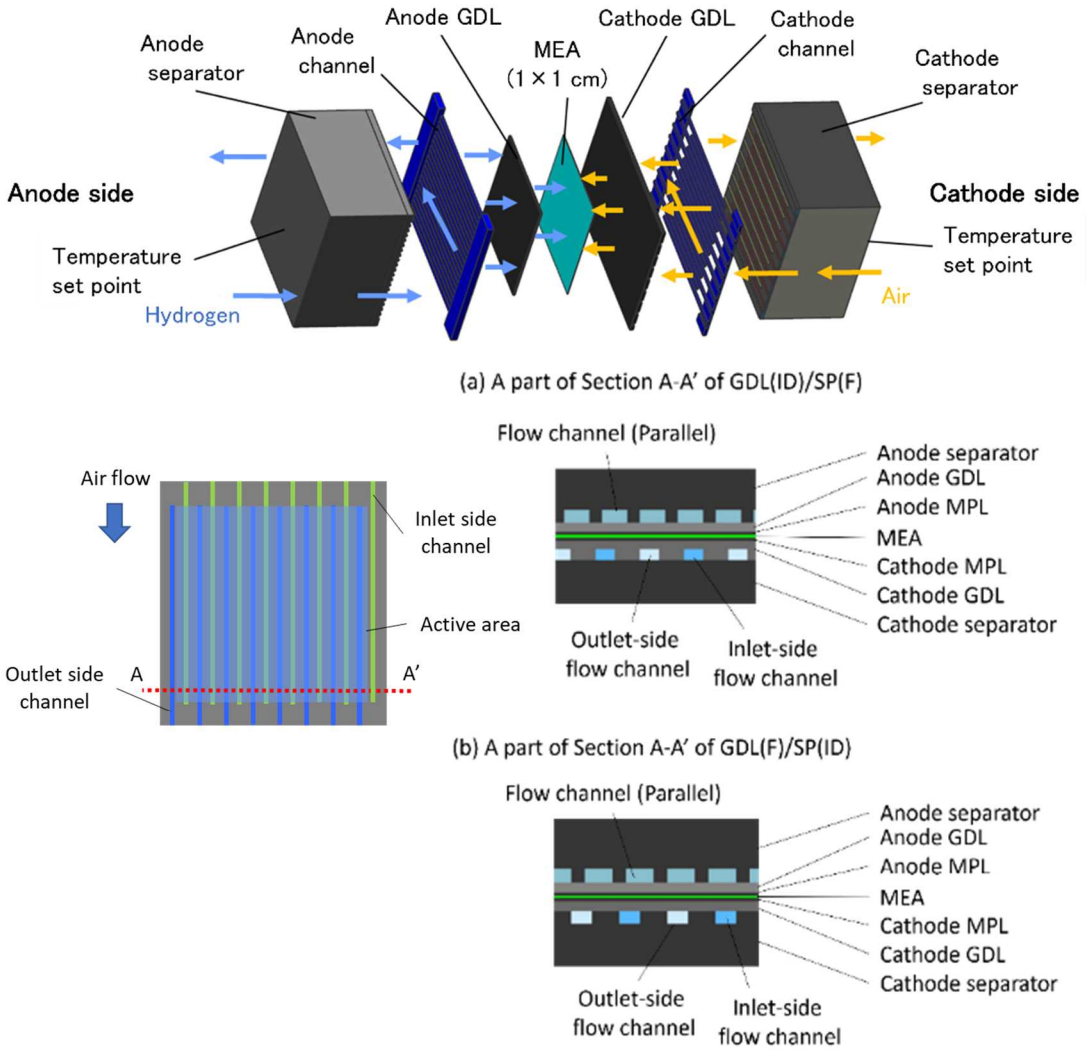

Figure 3-2. Schematic images of simulation model. (a) part of the cross section of A-A' of porous rib of GDL; (b) part of the cross section of A-A' of solid rib of separator.

Table 3-2. Geometrical properties for calculations

Physical properties of parameters	
Equivalent weight, EW	1100 g mol^{-1}
Membrane density	2.00 g cm^{-3}
Exchange current density (Anode / Cathode)	3.18 / 1.00 mA cm^{-2}
Permeability of porous media (Anode / Cathode)	9.00×10^{-6} /5.33 $\times 10^{-6}$ mm^2
GDL substrate porosity (Anode / Cathode)	0.88 / 0.60
MPL Porosity	0.41
Tortuosity factor (Substrate / MPL)	1.2 / 2.0
GDL thermal conductivity	0.5 W $m^{-1}K^{-1}$
Separator thermal conductivity	116 W $m^{-1}K^{-1}$

Table 3-3. Parameters of cathode flow channel design and operating conditions of calculations

Flow channel design	
Channel pitch	0.7 mm (0.4 mm channel width)
Channel depth	0.2 mm
Channel number	16
Operating conditions	
Current density	1.0 A cm^{-2}
Cell temperature	80 ℃
Relative humidity	100% RH (For temperature distributions) 15% RH (For gas flow distributions)
Flow rate (Anode / Cathode)	0.5 / 1.0 NL min^{-1}

3-3. Results and Discussions

3-3-1 X-ray imaging

Figure 3-3 and 3-4 shows time series plots of the relative humidity, the cell voltage and the ohmic resistance, and captured images of the liquid water distribution in the cross-section of the cell obtained from X-ray imaging during cell operation, in which the relative humidity was decreased from 120% RH to 40% RH in the channel structures of GDL(ID)/SP(F) and GDL(F)/SP(ID). Each image at relative humidities of (i) 120% RH, (ii) 80% RH, (iii) 50% RH and (iv) 40% RH was obtained at selected from the time-series images, which correspond to the timing of the corresponding number in the time-series graph. In captured images of the cross-sections of the cells in Figure 3-4, blue dots indicate the existence of liquid water. The brightness of the blue dot indicates the amount of liquid water along a path perpendicular to the cross-sectional plane, and thus the brightness increases with increasing amount of liquid water.

After 1200 seconds of operation under 120% RH condition, both the cell performance and liquid water distribution were in a steady state. In the image of GDL(ID)/SP(F) at the relative humidity of 120% RH in (i) of Figure 3-4(a), an uneven distribution of liquid water was confirmed in the ribs and flat parts of the GDL. In addition, more liquid water was confirmed near the outlet channel than the inlet channel of the GDL. In the flat part of the GDL, the amount of liquid water near the channel was smaller than that in the rib. In the image of GDL(F)/SP(ID) at 120% RH in (i) of Figure 3-4(b), liquid water was present throughout the flat part of the GDL. From the image of liquid water distribution of the porous ribs at 120%RH, it was first confirmed that liquid water was retained inside the ribs and minimized the condensation in the flat region of the GDL in the highly

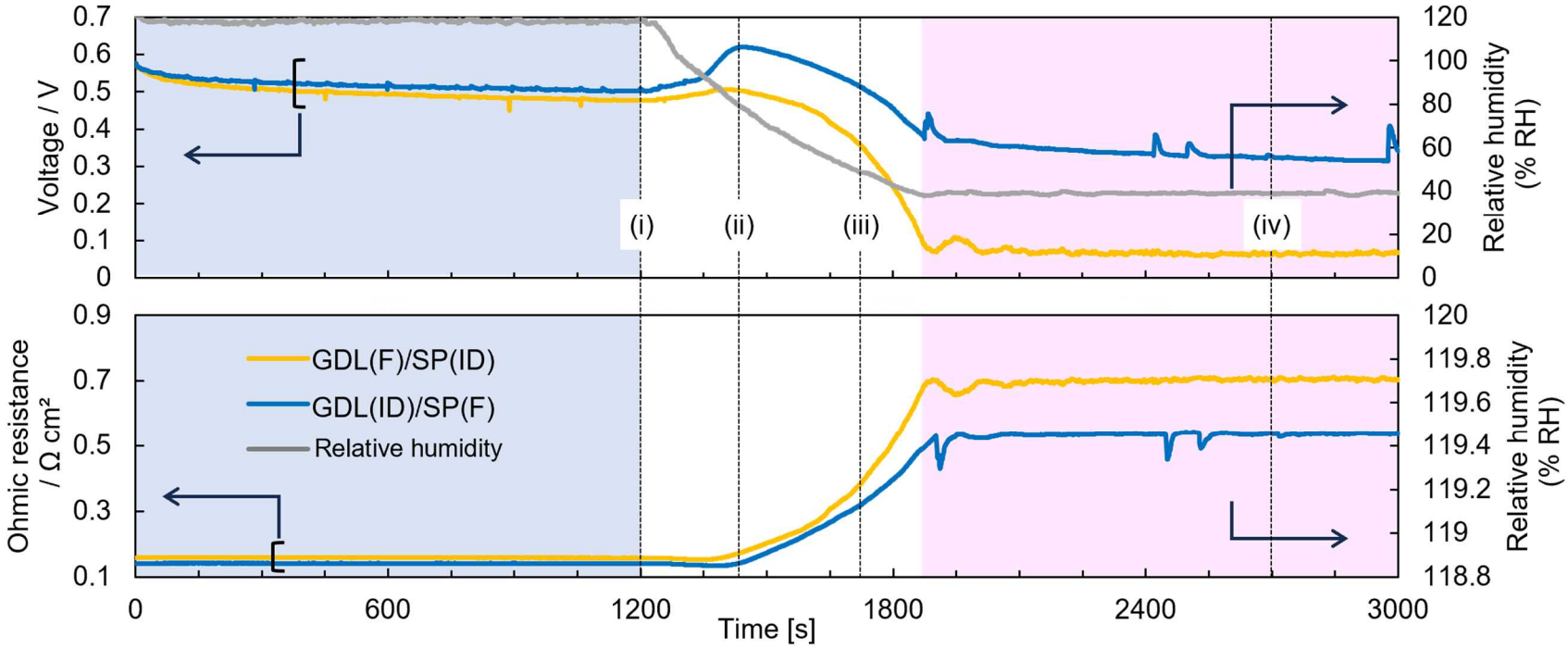

Figure 3-3. Behavior of cell voltages, ohmic resistances obtained from X-ray imaging cell during operation in which the relative humidity was varied from 120% RH to 40% RH. At points from (i) to (iv), Images of liquid water distribution were obtained and shown in figure 3-4.

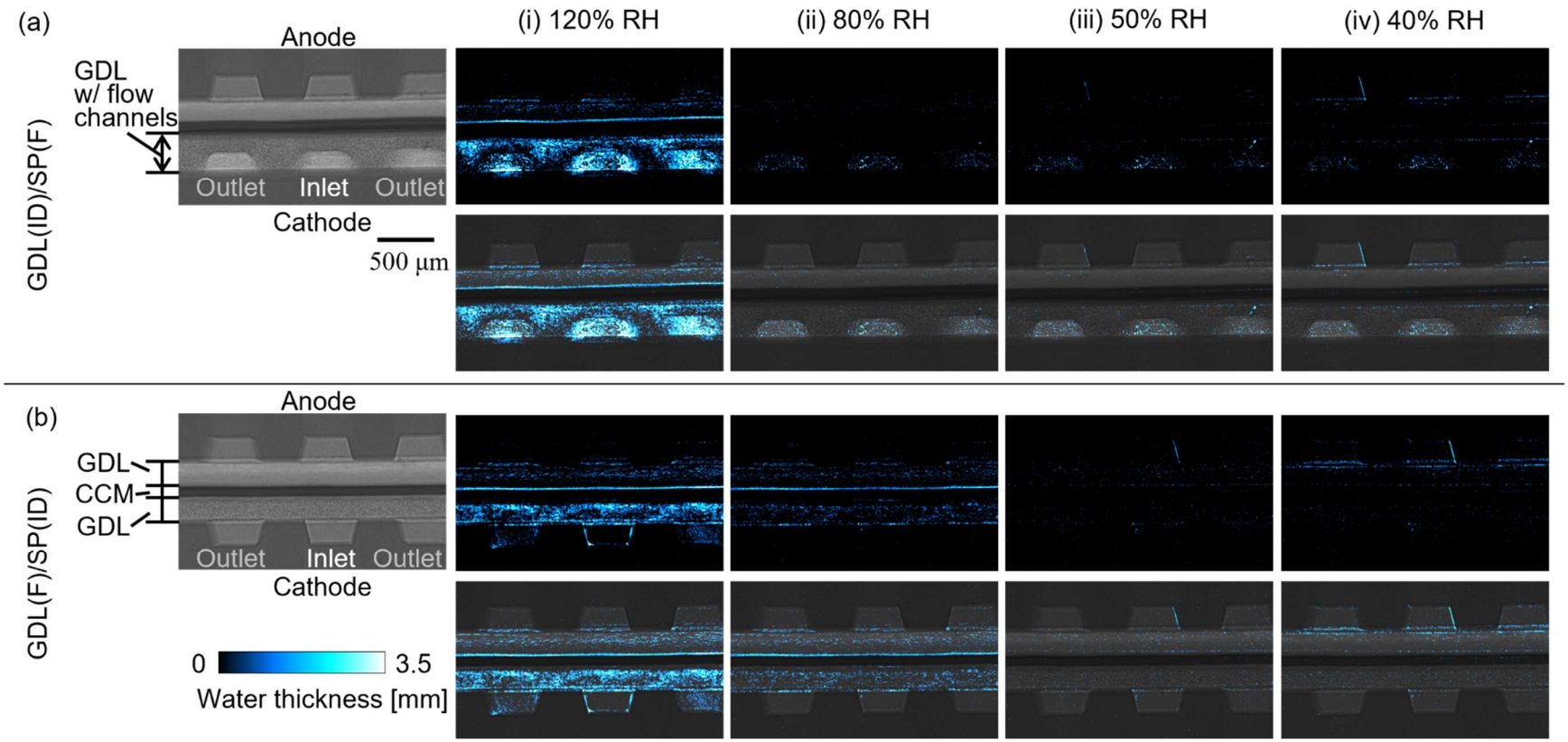

Figure 3-4. Behavior of liquid water distributions in the cross-section of the cell obtained from X-ray imaging during cell operation shown in figure 3-3. Images of liquid water distribution were obtained at each relative humidity: (i) 120% RH, (ii) 80% RH, (iii) 50% RH and (iv) 40% RH, shown in the time course of the figure 3-3. The amount of water along a path perpendicular to the cross-sectional plane, displayed as water thickness, is indicated by the brightness of the dots at each location on pictures in upper side for GDL(ID)/SP(F) and GDL(F)/SP(ID), respectively. And these semitransparent dots have been superimposed on the cross-sectional images of the cell on pictures in lower side for GDL(ID)/SP(F) and GDL(F)/SP(ID), respectively.

humidified condition of 120% RH, supporting the proposed mechanism that the porous ribs take up the excess water. Accumulated liquid water in the cathode GDLs in the 120% RH condition gradually decreased in the transient process to the 40%RH condition. The captured images of (ii) in Figure 3-4 (a) and (b) showed the water distributions of GDL(ID)/SP(F) and GDL(F)/SP(ID) at 80% RH, while (iii) showed the water distributions of GDL(ID)/SP(F) and GDL(F)/SP(ID) at 50% RH, and (iv) showed that at 40% RH. In the image of (ii) in Figure 3-4 (a), almost all of the liquid water in the GDL of GDL(ID)/SP(F) that had existed at 120% RH disappeared, both in flat part and inside the porous ribs. However, when the relative humidity decreased to 50% RH, as shown in (iii) in Figure 3-4 (a), a thin layer of liquid water was slightly evident around the interface between the MPL and the substrate of the GDL. The presence of this liquid water layer became clearer after being maintained for 10 minutes at 40% RH in the image of (iv) in Figure 3-4 (a), indicating that water produced at the cathode can remain in this region without suffering an excess discharge under such a drying atmosphere condition. In the case of GDL(F)/SP(ID), while the relative humidity was decreased from 120% RH to 40% RH, liquid water in the GDL gradually decreased, and finally disappeared at 40% RH as seen in the images at (ii), (iii) and (iv) in Figure 3-4 (b).

From the result that the water remaining in the porous ribs and the flat GDL of GDL(ID)/SP(F) at 120% disappeared at 80% RH, the proposed mechanism that the porous ribs act as a storage reservoir of excess water, which was verified from the difference of the timing to start the cell voltage decrease when the relative humidity started to decrease in Figure 2-14, was considered to be valid only for relative humidities higher than 80% RH.

From the comparison of images (iv) of GDL(ID)/SP(F) and GDL(F)/SP(ID) in Figure 3-4 (a) and (b), respectively, the amount of water around the interface between the MPL and the GDL substrate of GDL(ID)/SP(F) was more than that for GDL(F)/SP(ID), although stored water in the ribs and the flat GDL of GDL(ID)/SP(F) during 120% RH operation disappeared before 80% RH. On the other hand, the capability of GDL(ID)/SP(F) to retain more water in the flat GDL region under low humidification conditions than GDL(F)/SP(ID) was considered to be due to the weakened force to discharge water from the GDL, i.e., the lowered gas flow rate brought about by the splitting of the flow, with part of the flow going through the ribs. This result also

supported the proposed mechanism that a part of the supplied gas of GDL(ID)/SP(F) passes through the porous ribs to alleviate the dry-out of the flat GDL. To confirm the weakened gas flow in porous rib of GDL, the gas flows distributions in the GDL of both cells of GDL(ID)/SP(F) and GDL(ID)/SP(F) were calculated as described in the next section.

3-3-2 Numerical simulations

Figure 3-5 shows the temperature distributions in the cross-sections of the GDLs and the separators at a current density of 1.0 A cm^{-1}. Temperatures along the lines A, B and C in the image of the cross-section were plotted with the corresponding dew point temperatures on each line. Comparing the line profiles of the temperature on the outlet side channel as line C, the temperature of the interface between the MPL and MEA of the cell with porous ribs was 1.2 ˚C higher than that of the solid ribs. From the comparison of the temperature with the dew point temperature at the same position for each, in the case of the porous ribs, all points on the outlet side channel (line C), all points in the MPL and the flat GDL on the rib (line B) and 0.24 mm and higher from the GDL bottom on the inlet side channel (line A), exhibited higher temperatures than the dew points. In the case of the solid ribs, all points on the outlet side channel (line C) and 0.28 mm and higher from the GDL bottom on the rib (line B) showed higher temperatures than the dew point. Comparing the temperatures in the GDL with the dew point temperatures, and also comparing these between the porous ribs and the solid ribs, the area with higher temperature than the dew point temperature in the porous ribs was larger than that in the solid ribs. In particular, on the inlet side channel, more than half of the length in the MPL and the flat GDL of the porous ribs exhibited higher temperatures than the dew point temperatures, while none of the solid ribs showed higher temperatures than the dew point temperatures. The higher temperature of the porous ribs was thought to be due to their porosity, which resulted in their lower thermal conductivity than that of the solid ribs. These results support the proposed mechanism, i.e., that the porous ribs allow the temperature in the GDL to increase, resulting in alleviating the water accumulation in the GDL of the cell with porous ribs, thus improving the oxygen permeability to the catalyst layer.

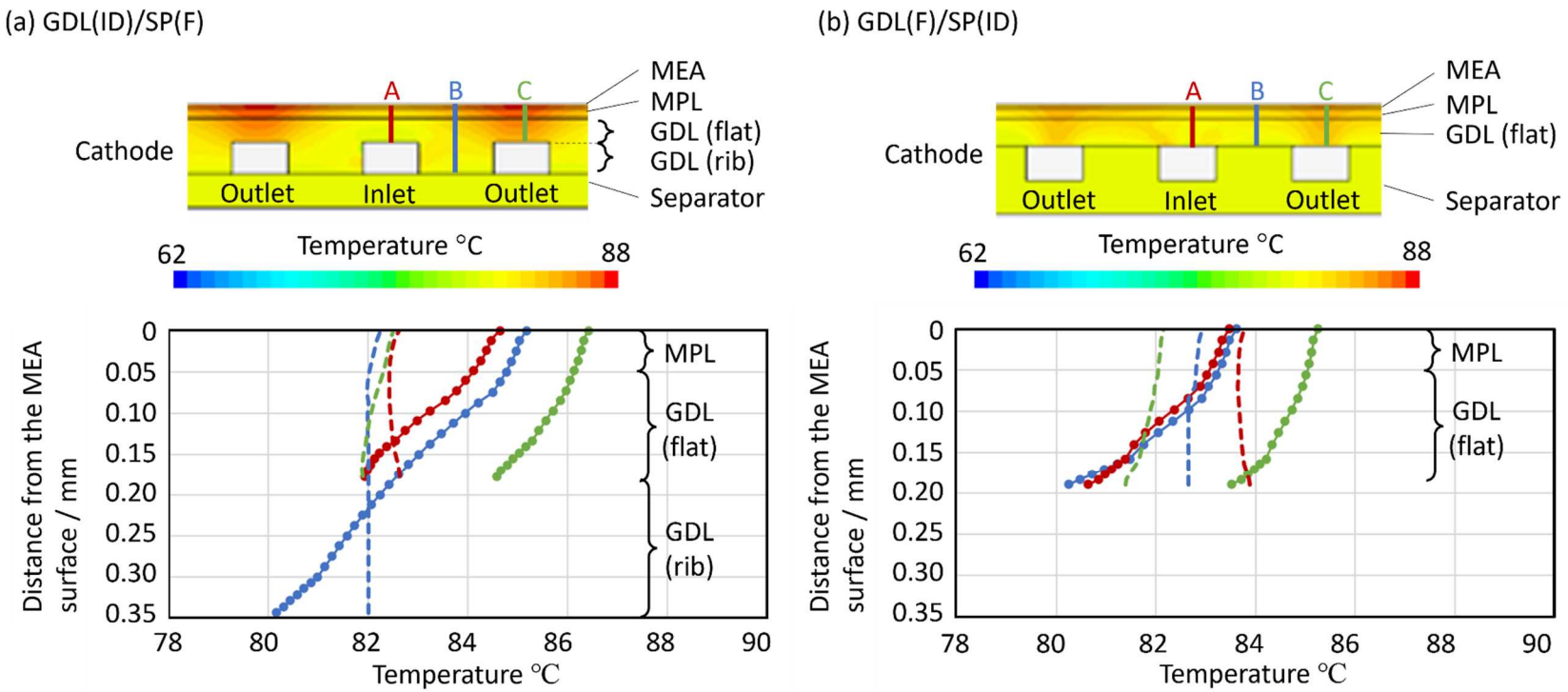

Figure 3-5. Temperature distributions in the cross-section of (a) porous rib of GDL and (b) solid rib of separator obtained by numerical simulations. Line profiles are plots of the temperature distribution along the direction of the GDL width at 3 positions: (line A) on the inlet side channel (red dots); (line B) going through the rib (blue dots); and (line C) on the outlet side channel (green dots). Dew points corresponding to line A, B and C are also drawn with red, blue and green dash lines, respectively, for the same positions.

Figure 3-6 shows the vector distributions of the gas flows in the cross-sections of A-A' in Figure 3-2 at 15% RH. In the case of GDL(ID)/SP(F), gases supplied from inlet side channels diffused to both the flat GDL and porous ribs, and reached to the outlet side channels. In the case of GDL(F)/SP(ID), all gases supplied from inlet side channel diffused to the flat GDL and reached to the outlet side channels. The length and the color of each vector indicates the velocity. At the middle position between the inlet side channel and the outlet side channel, the velocity of the vector in the flat GDL of the porous ribs was 1.83 m s^{-1}, while that in the rib of the cell with porous ribs was 1.49 m s^{-1}, whereas that in the flat GDL of the cell with solid ribs was 3.28 m s^{-1}. The direction of vectors in the middle of the inlet side channel and outlet side channel in both the flat GDL and the ribs was parallel to the direction from the inlet side channel to the outlet side channel.

From these results for the low humidification condition, it can be concluded that the gas flows velocity in the flat GDL of the cell with porous ribs was smaller than that of the cell with solid ribs. The smaller gas flow in the flat GDL of the cell with porous ribs is concluded to be due to the splitting of the gas flows to the porous ribs. This calculation result shows the same trend as the experimental result of X-ray imaging at 40% RH, thus

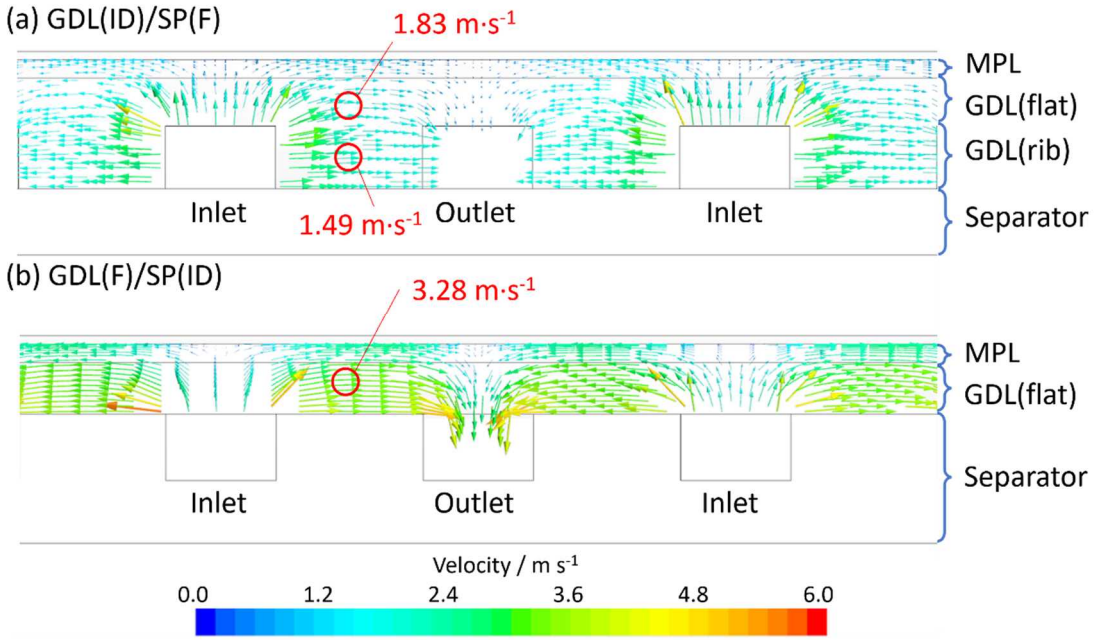

Figure 3-6. Vectors distributions of supplied gas flow from inlet side channels to outlet side channels in (a) porous rib of GDL and (b) solid rib of separator at 15% RH. The color of each vector shows the velocity of the gas flows.

supporting the proposed mechanism, i.e., that a portion of the gas supplied to the cell with porous ribs passes through the porous ribs except the case porous ribs are fulfilled with accumulated water, and this gas splitting alleviates the drying out of the GDL.

3-3-3 Summary of the experimental and simultaneous analysis

To summarize, the mechanism by which the porous ribs increase the performance stability under conditions with both excess water and insufficient water is proposed to be based on the presence of the porous ribs, which play four innovative roles, as shown schematically in Figure 3-7. Under high humidity operating conditions, (i) the supplied liquid water and part of the surplus water generated by the ORR in the cathode diffuse into the porous ribs, and thereby the liquid water saturation in the flat region of the GDL can be mitigated. At the same time, (ii) since the ribs are formed by the same porous

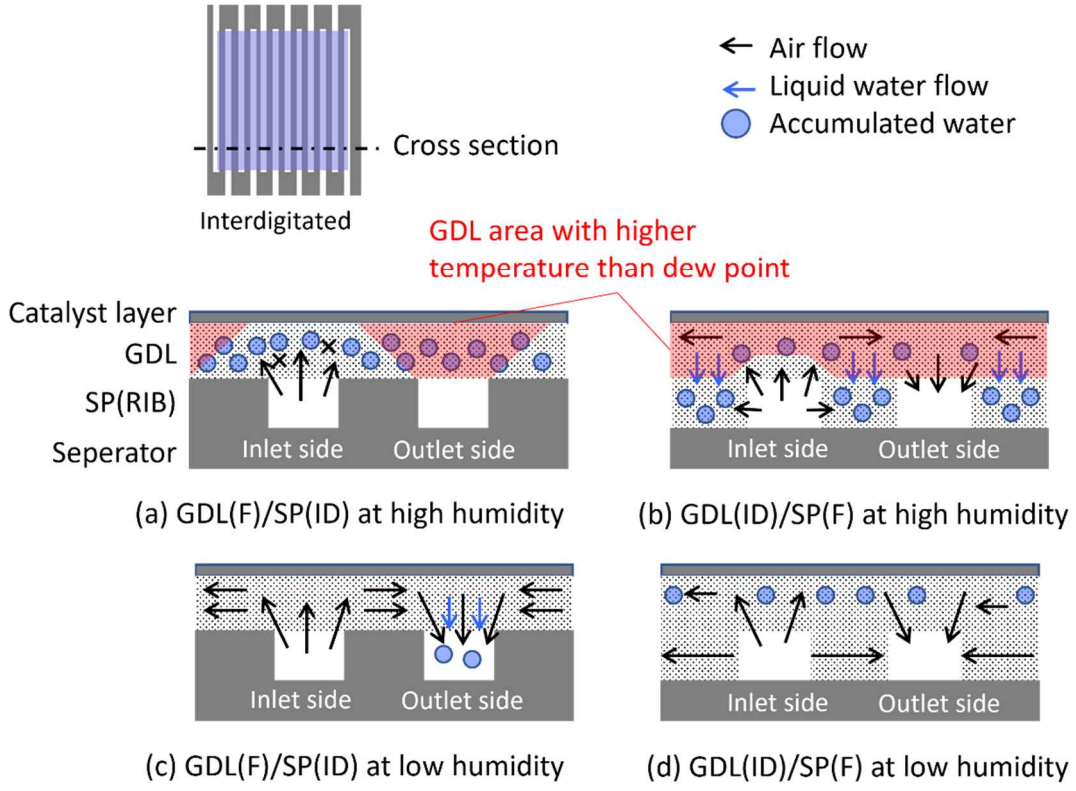

Figure 3-7. Schematic illustrations of the mechanism to explain higher cell-performance stability of porous rib of GDL by the difference of temperature, gas diffusion and water management at high relative humidity. (a) solid rib of separator and (b) porous rib of GDL.

material as the GDL, the thermal conductivity of the ribs is reduced to 1/100 or less than that in the solid ribs, in which the ribs are formed from solid materials such as graphitic carbon or metal. Therefore, the internal temperature of the flat region of the GDL near the interface with the MEA in the cell with porous ribs, which is a heat generating point, is higher than that in the cell with solid ribs. Also, the temperature of the flat region of the GDL in the cell with porous ribs, except for the lower half of the area on the inlet side channel, is higher than the dew point, so water droplets in these areas tend to vaporize. These two mechanisms, (i) and (ii), contribute to alleviating the water accumulation in the flat region of the GDL, thereby facilitating the oxygen transport to the catalyst layer, leading to the increased performance stability. Under low humidity operating conditions, (iii) at the beginning of the relative humidity decrease, before the relative humidity decrease at 80% RH in this study, a portion of the accumulated water in the porous ribs of the cell diffuses to the flat GDL and alleviates the drying out of the GDL and the MEA. After the water droplets disappeared from the porous ribs, (iv) a portion of the gas supplied from the inlet side channel diffuses to the outlet, passing through the porous ribs, lowering the flow rate through the GDL, thus resulting in less drying.

3-4. Conclusions

In the previous chapter, the new design for the interdigitated gas flow channels based on the use of a flat, solid separator and a porous GDL with channels formed on its surface was fabricated and incorporated into single cells. Both the performance and performance stability for this new design cell were found to improve under conditions with excess water compared to those of a conventional interdigitated cell with solid ribs. In addition, this newly designed interdigitated cell showed higher performance under conditions with a low-humidity gas supply than that for the conventional interdigitated cell. In this chapter, to reveal the performance improvement mechanism in the new design, X-ray imaging was applied to clarify the behavior of liquid water in the GDL and ribs during the cell operation under high and low humidification conditions. Furthermore, numerical simulation based on CFD was also applied to clarify and compare the temperature distributions in the GDLs for the new and conventional interdigitated cells. Based on the experimental and the simulation results, the porous ribs in the newly designed cell with

interdigitated flow channels on the GDL were found to play important and functional roles under conditions of both excess water and low-humidity gas supply, as follows: the porous ribs contribute to alleviating water accumulation in the GDL by taking up excess water and increasing the temperature of the GDL in the outlet-side channel, resulting in the performance stability improvement under conditions with excess water; and the porous ribs contribute to alleviating the drying out of the GDL and the MEA by supplying stored water to the flat GDL and allowing a portion of the supplied gas to pass through the porous ribs, resulting in a decrease in the velocity of the dry gas flow in the flat GDL. Based on the clarified mechanisms and improved performances, the newly designed cells with interdigitated channels on the GDL has demonstrated its potential to overcome the principal issues of the conventional cells with interdigitated channels on the separator.

3-5. References

1. M. Watanabe, H. Yanai and M. Nasu, Development and Analysis of an Innovative Flat-Metal Separator Integrating the GDL with Gas-Flow Channels as PEFC Components, *Journal of The Electrochemical Society*, Vol. 166, No. 7 (2019) F3210
2. P. Oberholzer and P. Boillat, Local Characterization of PEFCs by Differential Cells: Systematic Variations of Current and Asymmetric Relative Humidity, *Journal of The Electrochemical Society*, Vol. 161, No. 1 (2013) F139
3. H. Meng and CY. Wang, Large-scale simulation of polymer electrolyte fuel cells by parallel computing, *Chemical Engineering Science*, Vol. 59, Issue 16 (2004) 3331-3343
4. T. V. Nguyen, A Gas Distributor Design for Proton-Exchange-Membrane Fuel Cells, *J. Electrochem. Soc*., Vol. 143, No.5 (1996)
5. D. L. Wood, III, Jung S. Yi. and T. V. Nguyen, Effect of direct liquid water injection and interdigitated flow field on the performance of proton exchange membrane fuel cells, *Electrochimica Acta*, Vol. 43, No. 24, 3795 (1998)
6. A. D. Le, B. Zhou, A generalized numerical model for liquid water in a proton exchange membrane fuel cell with interdigitated design, *Journal of Power Sources*, Vol. 193, Issue 2 (2009), 665-683
7. Vaisala, Humidity Conversions – Formulas and Methods for Calculating Humidity

Parmeters
https://www.vaisala.com/system/files/documents/Humidity-conversion-formulas-Technical-eBook-B210973EN.pdf

8. W. Wagner and A. Pru, The IAPWS formulation 1995 for the thermodynamic properties of ordinary water substance for general and scientific use, *Journal of Physical and Chemical Reference Data*, Vol. 31, Issue 2 (2002) 387-535
9. M. Nasu, H. Yanai, N. Hirayama, H. Adachi, Y. Kakizawa, Y. Shirase, H. Nishiyama, T. Kawamoto, J. Inukai, T. Shinohara, H. Hayashida and M. Watanabe, Neutron imaging of generated water inside polymer electrolyte fuel cell using newly-developed gas diffusion layer with gas flow channels during power generation, *Journal of Power Sources*, Vol. 530, (2022) 231251
10. CY. Lee, FB. Weng, CH. Cheng, HR. Shiu, SP. Jung, WC. Chang, PC. Chan, WT. Chen and CJ. Lee, Use of flexible micro-temperature sensor to determine temperature in situ and to simulate a proton exchange membrane fuel cell, *Journal of Power Sources*, Vol. 196, Issue 1 (2011) 228-234
11. H. Pei, Z. Liu, H. Zhang, Y. Yu, Z. Tu, Z. Wan, W. Liu, In situ measurement of temperature distribution in proton exchange membrane fuel cell I a hydrogen–air stack, *Journal of Power Sources*, Vol. 227 (2013) 72-79
12. R. Sur, T. J. Boucher, M. W. Renfro and B. M. Cetegen, In Situ Measurements of Water Vapor Partial Pressure and Temperature Dynamics in a PEM Fuel Cell, *Journal of The Electrochemical Society*, Vol. 157, Nol. 1 (2009) B45
13. TF. Cao, YT. Mu, J. Ding, H. Lin, YL. He and WQ. Tao, Modeling the temperature distribution and performance of a PEM fuel cell with thermal contact resistance, *International Journal of Heat and Mass Transfer*, Vol. 87 (2015) 544-556
14. A. Nishimura, K. Yamamoto, T. Okado, Y. Kojima, M. Hirota, M. L. Kolhe, Impact analysis of MPL and PEM thickness on temperature distribution within PEFC operating at relatively higher temperature, *Energy*, Vol. 205 (2020) 117875
15. G. Inoue, Y. Matsukuma and M. Minemoto, Effect of gas channel depth on current density distribution of polymer electrolyte fuel cell by numerical analysis including gas flow through gas diffusion layer, *Journal of Power Sources*, Vol. 157, Issue 1 (2006) 136-152
16. Y. Wang and CY. Wang, Simulation of flow and transport phenomena in a polymer

electrolyte fuel cell under low-humidity operation, *Journal of Power Sources*, Vol. 147, Issue 1–2 (2005) 148-161

17. K. Ogawa, T. Sasaki, S. Yoneda, K Tsujinaka and R. Asai, Two-dimensional spatial distributions of the water content of the membrane electrode assembly and the electric current generated in a polymer electrolyte fuel cell measured by 49 nuclear magnetic resonance surface coils: Dependence on gas flow rate and relative humidity of supplied gases, *Journal of Power Sources*, Vol. 444 (2019) 227254
18. N. Pekula, K. Heller, P.A. Chuang, A. Turhan, M.M. Mench, J.S. Brenizer and K. Ünlü, Study of water distribution and transport in a polymer electrolyte fuel cell using neutron imaging, *Nuclear Instruments and Methods in Physics Research Section A: Accelerators, Spectrometers, Detectors and Associated Equipment*, Vol. 542, Issue 1–3 (2005) 134-141
19. T. Sasabe, S. Tsushima and S. Hirai, In-situ visualization of liquid water in an operating PEMFC by soft X-ray radiography, *International Journal of Hydrogen Energy*, Vol. 35, Issue 20 (2010) 11119-11128
20. SJ. Lee, NY. Lim, S. Kim, GG. Park and CS. Kim, X-ray imaging of water distribution in a polymer electrolyte fuel cell, *Journal of Power Sources*, Vol. 185, Issue 2 (2008) 867-870
21. M. Ishii, T. Hibiki, Thermo-Fluid Dynamics of Two-Phase Flow, *Springer* (2011).
22. D. B. Spalding, A standard formulation of the steady convective mass transfer problem, *International Journal of Heat and Mass Transfer*, Vol. 1 (1960) 192-207

Chapter 4 Research on the Repeatability of Performance Stability of a Cell with Interdigitated Flow Channels on the GDL with the Extended Active Area Cell

4-1. Introduction

As the summary of experimental and simultaneous results carried out in Chapter 2 and 3, the newly designed cell with interdigitated flow-channel on the GDL was found to have a breakthrough to have advantages on its performance: one is the repeatability of the lower diffusion overvoltage in the conventional interdigitated flow-channel on the separator than the parallel flow-channel; second is the possibility to mitigate the issue of the conventional interdigitated cell on performance degradation under conditions with existence of excess water or dried air supply.[1-4] These advantages were also found to be caused by the existence of porous ribs which contribute to water management on both alleviating water saturation in the GDL pores close to the catalyst layer and keeping generated water in the GDL and the catalyst layer. As shown in Chapter 2, the diffusion overvoltage of the newly designed cell with interdigitated flow-channels on the GDL at higher current density were slightly larger than that of the conventional cell with interdigitated flow-channels on the separator at 100% RH. This experiment was carried out with the partially extracted cell of 1.0 × 1.0 cm active area to evaluate cell performance locally by minimizing the variation of operating conditions, such as the oxygen density, the gas pressure and the relative humidity.[5] In the case of performance evaluation with larger active-area cells such as practical cell for FCVs, the performance of the cell with interdigitated flow-channels on the GDL is expected to exhibit better than that of the cell with interdigitated flow-channels on the separator, because the cell with interdigitated flow-channels on the GDL showed higher performance stability against variations of cell operating conditions including the relative humidity as described in chapter 2.[6] Experiments with larger size cell of 3.0 × 9.7 cm active area were carried out in Chapter 2, but applied cell design was limited in two type of cells: the cell with interdigitated flow-channels on the GDL and the cell with serpentine flow-channels on the separator to investigate the more detailed performance comparison based on the examined cells by M. Watanabe et al.[4] M. Nasu et al. showed that the cell with interdigitated flow-channels on the GDL showed higher cell voltage at 1.0 A cm^{-2} and

higher current density than the cell with interdigitated flow-channels on the separator. This experiment was carried out with cells of 1.0 × 9.7 cm active area, but the correlation of performances between local area and total in the cell was not mentioned in this research.[7]

In this chapter, To validate whether the performance of GDL(ID)/SP(F) with the larger-size cell is higher than that of GDL(F)/SP(ID), as well as to confirm the repeatability of the robustness on its performance under the humidity variations, I constructed cells with 1.0 × 10 cm active area by extending the cell length of 1.0 × 1.0 cm cell along the direction of flow channel, and compared performances between the difference of the surface flow-channel formed on and the shape of flow channel as carried out with 1.0 × 1.0 cm cell in Chapter 2.

4-2. Experimental

As described in the case of experiments with 1.0 × 1.0 cm cell in Chapter 2, four cells of different channel designs were examined and compared their performances in order to make clear the effect on cell performances depending on the difference in flow-channel shapes and rib materials. These cells had a 1.0 × 10 cm active area and included four different combinations of channel design based on the two channel shapes and the two channel locations as shown in figure 4-1. The channel shapes included parallel and interdigitated, and the channel locations included on the GDL and on the separator. Hereafter, the symbols of each channel design will be used as follows: GDL with interdigitated ribs + flat separator, GDL(ID)/SP(F); flat GDL + separator with interdigitated ribs, GDL(F)/SP(ID); GDL with parallel ribs + flat separator, GDL(P)/SP(F); flat GDL + separator with parallel ribs, GDL(F)/SP(P).

The designs of the 1.0 × 10 cm active-area cells were determined by expanding the length of 1.0 × 1.0 cm cell along the direction of gas flow. Table 4-1 shows materials and flow-channel designs of 1.0 × 10 cm cell. These parameters were almost same as that in 1.0 × 1.0 cm cell except the length of the active area. Designs of cathode channel were also same as 1.0 × 1.0 cm cells, GDL(ID)/SP(F), GDL(F)/SP(ID), GDL(P)/SP(F) and GDL(F)/SP(P).

The evaluation of cell performance was focused on two features: i) the polarization

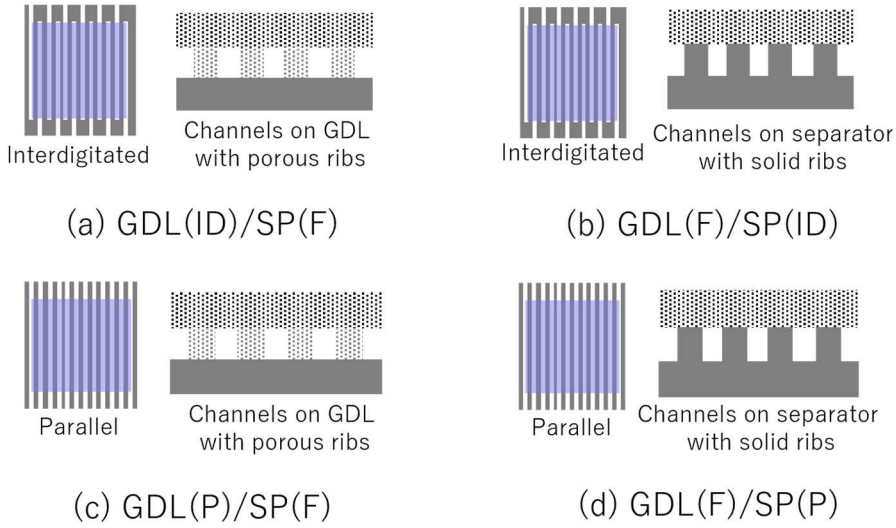

Figure 4-1. Schematic images of each flow channel design and corresponding symbols correlations with the various channel designs under various experimental conditions (e.g., oxygen percentage, relative humidity in the gas and gas pressure). In these cells, it is straightforward to achieve highly uniform distributions of reactants and products in the active area.

characteristics with broader variation of operating conditions including oxygen percentage, pressure and humidity than 1.0 × 1.0 cm cells; and ii) the cell voltage stability when the relative humidity decreased. Table 4-2 shows the conditions of each experiment, and further details are indicated below.

Conditioning. Anode and cathode were purged with dry nitrogen; then, hydrogen and air were supplied to the anode and cathode, respectively. The current density was increased from 0 to 1.6 A cm^{-2} in 0.2 A cm^{-2} steps and then maintained for 5 hours at 1.6 A cm^{-2}. The conditions of the supplied gases are shown in Table 2-3.

Polarization. After the conditioning was complete, the current density was increased and decreased between 0 and 1.6 A cm^{-2}, in steps of 0.2 A cm^{-2} (0.02 A cm^{-2} under 0 to 0.1 A cm^{-2}), and two complete cycles were carried out. The duration time at each current density was 5 minutes from 0 to 1.0 A cm^{-2}, and 10 minutes from 1.2 to 1.6 A cm^{-2}. During the second cycle, the average voltage of the cell was measured over the final 1 minute of the 5 minutes duration time at each current density and was plotted as the polarization curve.

Relative humidity characteristics. After the experiment of the polarization, the relative humidity of the cathode air was varied: 80, 100 and 15% RH at 1.0 A cm^{-2}. The duration times were 5 hours at 80 and 100% RH, while 20 hours was used at 15% RH because of the time taken to decrease the temperature of the cathode humidifier.

Table 4-1. Specifications of experimental cells with 1.0 × 10 cm active area

Cell type		GDL(F)/SP(P)	GDL(P)/SP(F)	GDL(F)/SP(ID)	GDL(ID)/SP(F)
Anode catalyst	Material	TEC10E50E (Tanaka Kikinzoku Kogyo)			
	Load	0.1 mg-Pt cm^{-2}			
	I/C	0.7			
Cathode catalyst	Material	TEC10E50E			
	Load	0.4 mg-Pt cm^{-2}			
	I/C	0.7			
Membrane	Material	Nafion HP (Chemours)			
Anode GDL	Material	29BC (SGL)			
Cathode GDL	Material	Enomoto Co., Ltd. test sample			
	Thickness	0.20 mm	0.36 mm	0.20 mm	0.36 mm
Flow design	Shape	Parallel		Interdigitated	
	Location	Separator	GDL	Separator	GDL
	Pitch	0.6 mm		0.7 mm	
	Channel width	0.4 mm		0.4 mm	
	Depth	0.2 mm		0.18 mm	
	Channel Number	17	16	16	16
	Channel Area	1.36 mm^2		1.01 mm^2	

Table 4-2. Experimental conditions of cells with 1.0 × 10 cm active area

Experiment		Polarization	Relative humidity characteristics
Cell temperature		80 °C	
Current density		From 0 to 1.6 A cm^{-2}	1.0 A cm^{-2}
Anode	Gas	Pure hydrogen	
	Flow rate	0.5 NL min^{-1}	
	Relative humidity	100% RH	
	Outlet pressure	0 kPa	
Cathode	Gas	Air	
	Flow rate	2.0 NL min^{-1}	1.0 NL min^{-1}
	Relative Humidity	80% RH	15, 40 and 100% RH
	Outlet pressure	0 kPa	

4-3. Results and Discussions

Polarization. Figure 4-2 shows the comparisons of (a) the polarization curves and (b) the diffusion overvoltages between GDL(ID)/SP(F), GDL(F)/SP(ID), GDL(P)/SP(F) and GDL(F)/SP(P). Diffusion overvoltages are obtained at 1.6 A cm^{-2}, which were calculated as the difference of the IR-free voltage and the voltage obtained by the extrapolation of the IR-free Tafel plots between 0.03 and 0.1 A cm^{-2}, i.e., kinetic region, to 1.6 A cm^{-2}.[8] The cell voltages of GDL(ID)/SP(F) were higher than other three cells including GDL(F)/SP(ID), which showed slightly higher cell voltage at higher current density with 1.0 × 1.0 cm cells. Also, in the case of comparison in diffusion overvoltages, GDL(ID)/SP(F) showed lower diffusion overvoltage at 1.6 A cm^{-2} than other three cells including GDL(F)/SP(ID) which showed 6 mV lower diffusion overvoltage with 1.0 × 1.0 cm cells.

These results indicate that the superiority and inferiority of the performance in GDL(ID)/SP(F) and GDL(F)/SP(ID) with 1.0 × 1.0 cm cells was reversed in the case with 1.0 × 10 cm cells. As I suggested in Chapter 2 and the introduction of this chapter, the reason to cause this reverse depends on the difference of the variation range of operating conditions in cells with 1.0 × 1.0 cm and 1.0 × 10 cm active areas. Based on the operating conditions shown in table 4-2, the relative humidity at the inlet of cells was 80% RH and the air flow-rate was 2.0 NL min^{-1}, therefore the relative humidity at the outlet of cells was calculated to 93% RH when the current density was 1.6 A cm^{-2}. In the case of 1.0 × 1.0 cm cells, the relative humidity in the outlet of cells was only 1.3% higher than that of the inlet when the current density was 1.6 A cm^{-2}. Because of this broader variation of the relative humidity in 1.0 × 10 cm cells and higher performance stability of GDL(ID)/SP(F) against the variation of operating conditions as shown in Chapter 2, the performance of GDL(ID)/SP(F) was considered to exceed that of GDL(F)/SP(ID). In this experiment, air flow rate was fixed at 2.0 NL min^{-1}, which corresponds to the air utilization ratio U_{air} of 13.3% at 1.6 A cm^{-2}. Since U_{air} of practical cells should be much higher, up to 50%, to suppress the load increase of the air compressor which decrease the net power of the fuel cell system, the advantage of GDL(ID)/SP(F) on its performance is considered to be enhanced with practical cells because GDL(ID)/SP(F) showed higher performances under conditions with lower oxygen percentage in Chapter 2. From the comparison of diffusion

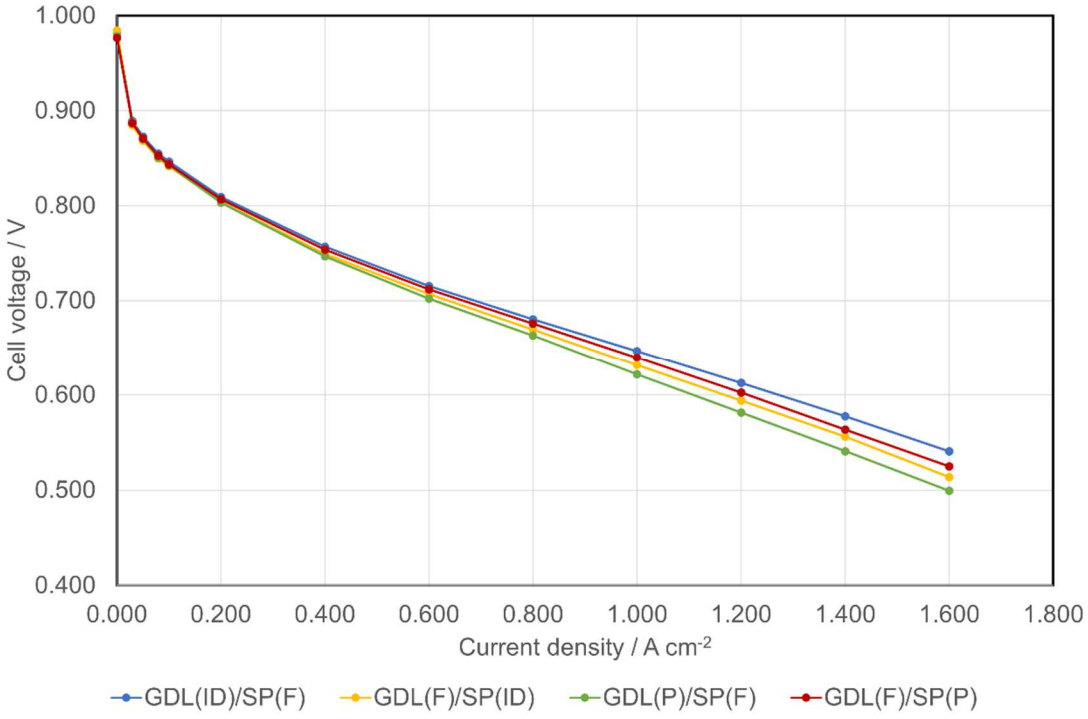

(a) polarization curves

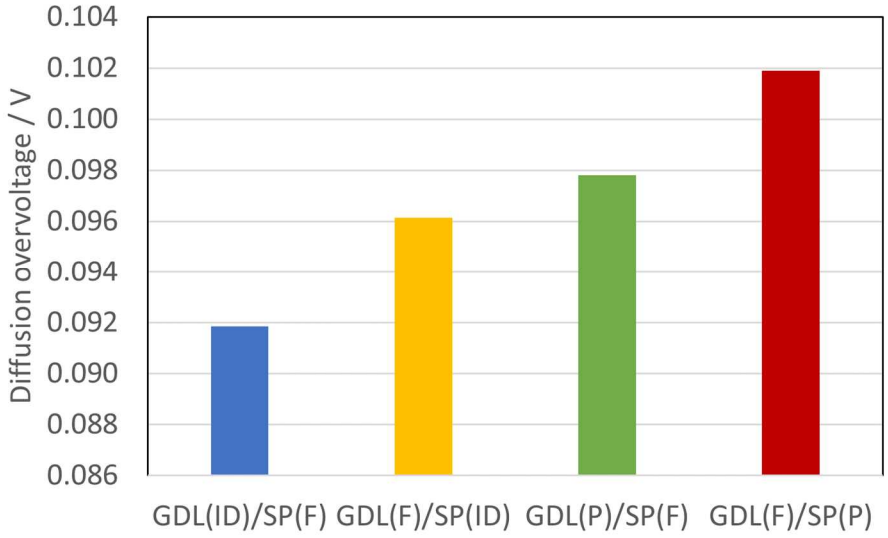

(b) diffusion overvoltages

Figure 4-2. Comparisons of (a) polarization curves from 0 to 1.6 A cm^{-2} and (b) diffusion overvoltages at 1.6 A cm^{-2} among four different cell design in cells of GDL(ID)/SP(F); blue, GDL(F)/SP(ID); yellow, GDL(P)/SP(F); green and GDL(F)/SP(P); red, with 1 × 1 cm active area. Each result was averaged from three cells operated at 80°C and 100% RH.

overvoltages in GDL(ID)/SP(F) and GDL(P)/SP(F) at 1.6 A cm^{-2}, GDL(ID)/SP(F) showed about 0.06 V lower overvoltage than GDL(P)/SP(F). In the case of 1.0 × 1.0 cm cells, as shown in figure 2-8(b), the diffusion overvoltage of GDL(ID)/SP(F) was about 0.16 V lower than that of GDL(P)/SP(F). This result indicates that the advantage of GDL(ID)/SP(F) on oxygen supply efficiency was weakened in 1.0 × 10 cm cells when compared with 1.0 × 1.0 cm cells. I suggest that this result was caused by the weakened gas-flow convection in the GDL, because the forced convection of supplied gas in the GDL with interdigitated channels, which contribute to enhance the oxygen supply to the catalyst layer, is considered to be not uniform and concentrate at the end of inlet side channel. For validation of this suggestion and farther discussion, numerical simulations of CFD to simulate the gas flow distribution in cells were carried out later in this chapter.

Effects of relative humidity. Figure 4-3 shows the changes over time in cell voltage and Ohmic resistance in GDL(ID)/SP(F) and GDL(F)/SP(ID) when the relative humidity conditions of the cathode air were varied 80% RH to 100% RH and then to 15% RH, by changing the dew point of the cathode air from 74 °C to 80 °C and then 40 °C while the cell temperature was maintained at 80 °C.

First, when the relative humidity was increased from 80% RH to 100% RH, the Ohmic resistances decreased and the cell voltages increased in both cells, but the cell voltage of GDL(ID)/SP(F) was kept higher about 20 mV than that of GDL(F)/SP(ID), while the ohmic resistance of GDL(ID)/SP(F) was kept lower about 1 mΩ than that of GDL(F)/SP(ID) at 100% RH. These differences in cell performance were similar to the result of polarization.

When the humidity started to decrease from 100% RH, the cell voltage of both GDL(ID)/SP(F) and GDL(F)/SP(ID) started to decrease immediately, while the decrease ratio of the cell voltage in GDL(ID)/SP(F) was slightly lower than that in GDL(F)/SP(ID). When the experiment completed at 15% RH, the value of cell voltage drop from that in the condition with 100% RH was 70 mV in GDL(ID)/SP(F), while GDL(F)/SP(ID) showed 84 mV cell-voltage drop. These values were calculated from the average in 1 hour because fluctuations of cell voltages were observed.

From these results, the stability of the cell voltage in GDL(ID)/SP(F) was also found to repeat in the extended cells. However, the difference of cell voltage drops from high

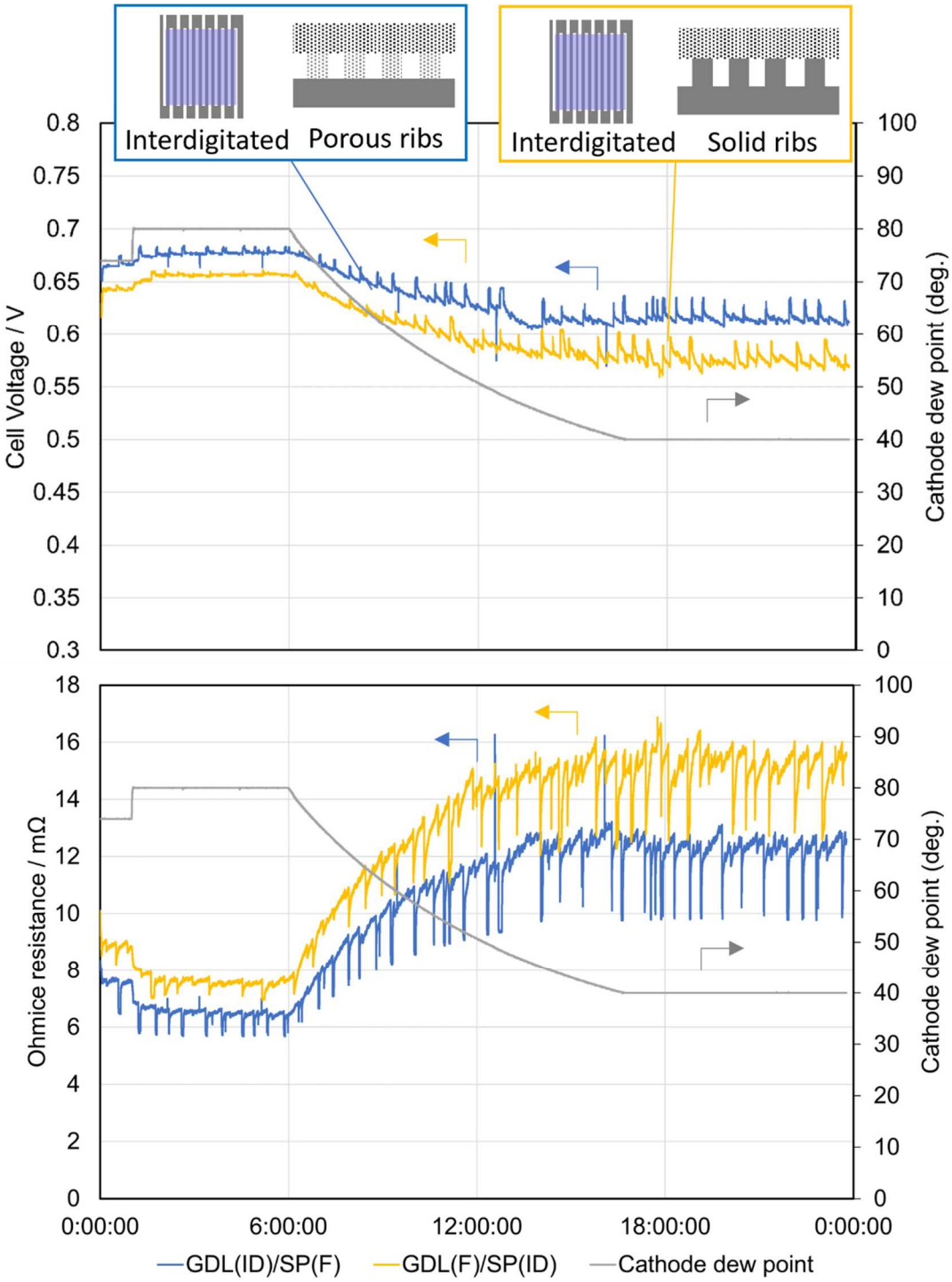

Figure 4-3. Changes over time in (a) cell voltages and (b) Ohmic resistances during relative humidity variations from 80% to 100% and 15% RH in a stepwise fashion. The current density was maintained at 1.0 A cm^{-2} during the experiment.

humidity to low humidity in GDL(ID)/SP(F) and GDL(F)/SP(ID) was 14 mV, and this value is a half smaller in the case of the same comparison in 1.0 × 1.0 cm cells which was around 30 mV from the experimental result shown in figure 2-14. I suggest the reason that the advantage of GDL(ID)/SP(F) on the performance stability in 1.0 × 10 cm cells was mitigated compared to the case in 1.0 × 1.0 cm cells was due to the fact that the forced convection of gas flow in the GDL is concentrated around the end of inlet side channel, as discussed in the result of polarization. As validated in Chapter 3, the cell voltage stability of GDL(ID)/SP(F) under low humidification conditions are obtained by the weakened gas flow in the flat GDL as a result of the short pass of gas flow through porous ribs from inlet side channels to outlet side channels. Since the available area of gas short pass which corresponds to the area the forced convection occurs is considered to be distributed locally at the end of gas flow, at the cell with larger active area, the effect of gas short pass to the total cell performance was considered to be weakened.

4-4. Numerical simulations of gas flow distributions in 1.0 × 10 cm cells

From experimental results in Chapter 4-3, the flow-channel design of GDL(ID)/SP(F) was found to contribute the improvement of the cell performance also in the extended cell with 1.0 × 10 cm active area, but the contribution was weakened compared to the case of cells with 1.0 × 1.0 cm active area. I suggested the reason of the weakened contribution is based on the nonuniform distribution of the forced convection in the active area of interdigitated cells, resulting in decreasing the ratio of the area to the whole active area where the performance stability improvement by the forced convection is effective. To validate this suggestion, the gas flow distribution in the cell was calculated with CFD software package STAR-CCM+ ver. 13.06. Applied equations were same as listed in Chapter 3-2-2, however, to simplify simulations and focus on the behavior of the gas flow, the presence of the liquid water and electrochemical reactions were excluded in simulations.

Figure 4-4 shows schematic images of simulation models. Model 1 in figure 4-4 shows a GDL(ID)/SP(F) cell model which is a same flow-channel design as the experimental cell indicated in Chapter 4-2. Model 2 and 3 are designed to investigate the effect of the flow-channel design on gas flow distributions by splitting the interdigitated flow-channel

to 2 or 3 segments along the gas flow direction. Table 4-3 shows a list of geometrical properties of calculation models and gas flow conditions in calculations.

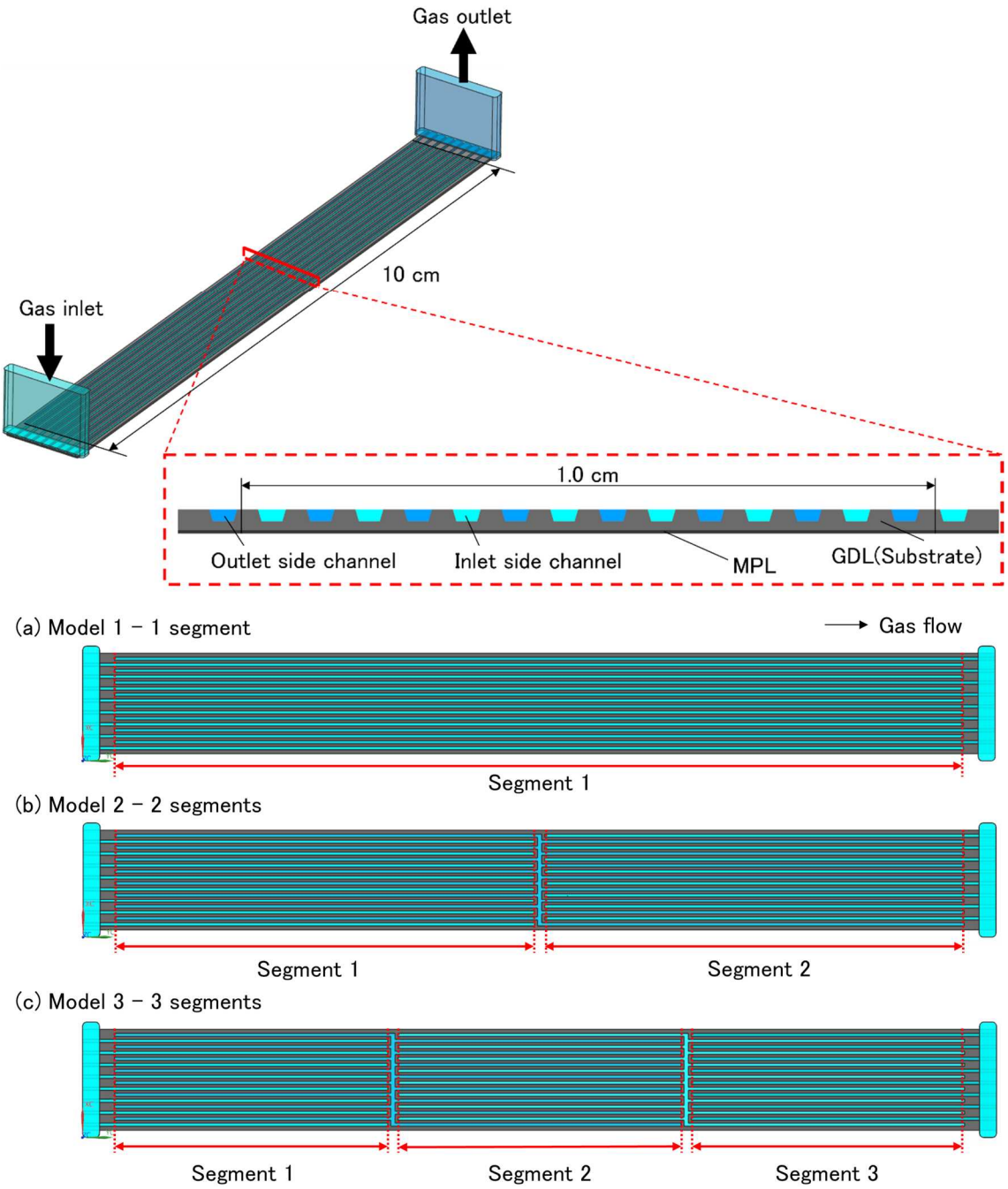

Figure 4-4 Schematic images of simulation model. Pictures in upper side show an overview and a cross section of a simulation model. Pictures in lower side show top views of 3 models with interdigitated flow channel: (a) consists of 1 segment of interdigitated flow channel, (b) was split into 2 segments of interdigitated flow channels and (c) was split into 3 segments of interdigitated flow channels.

Table 4-3. Geometrical properties of calculation models and gas flow conditions

Physical properties of parameters	
Permeability of porous media	5.33 $\times 10^{-6}$ mm^2
GDL substrate porosity	0.60
MPL Porosity	0.41
Tortuosity factor (Substrate / MPL)	1.2 / 2.0
Channel pitch	0.7 mm (0.4 mm channel width)
Channel depth	0.2 mm
Channel number	16
Flow rate	1.0 NL min^{-1}
Outlet pressure	0 kPa

Figure 4-5 and 4-6 shows simulation results of model 1 with 1 segment flow-channel.

Figure 4-5 shows a top view of the cell active-area with the gas-flow vector distributions in whole cell active-area. Gas flow distributions were calculated at the red dotted line in the upper picture in figure 4-5, which is located in the middle of the GDL substrate height, to evaluate the intensity of the forced convection in the flat GDL area. Vectors of the gas flow were colored depending on the velocity of gas flow on each point, while the length of the vector also indicate its velocity for each. Figure 4-5 indicated that the gas flow in the flat GDL was concentrated around the end of the inlet side channel and the gas flow in other area was negligibly small.

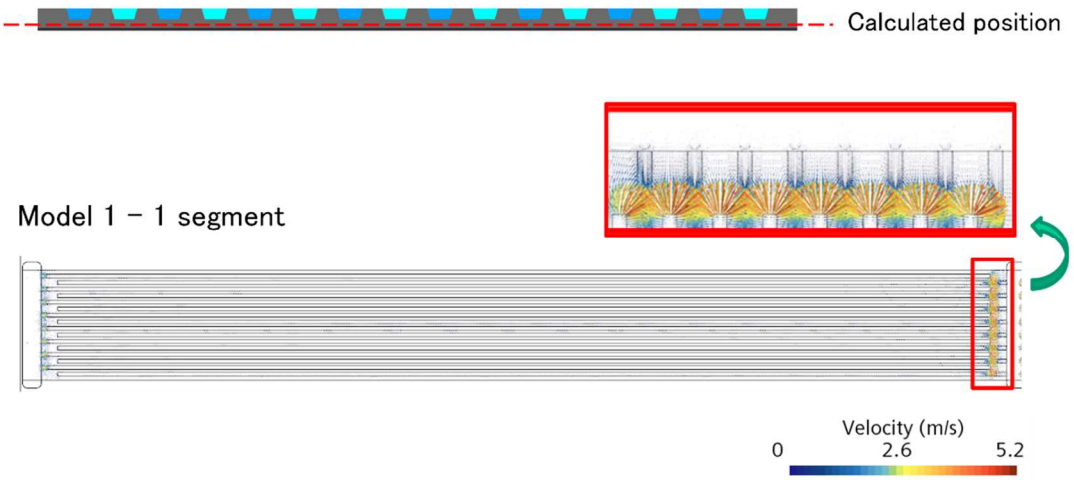

Figure 4-5 Top view of cell active-area with gas-flow vector distribution in model 1. The color and the length of gas-flow vectors indicates the velocity of each vector. Upper picture shows the calculated position of the gas flow which is located in the middle of the GDL substrate height.

Figure 4-6 shows gas-flow distributions in cross sections of the flow channel in model 1. Gas flow vectors in the GDL was calculated at three cross sections, (a) in upper side of gas flow (Line A), (b) down side of gas flow (Line B) and (c) at the end of inlet side channel (Line C). Vectors of the gas flow were colored depending on the velocity of gas flow on each point, while the length of the vector also indicate its velocity for each. In cases of (a) line A and (b) line B, the gas flow across from inlet side channels to outlet side channels was almost not founded, while in the case of (c) line C, the gas flow across from inlet side channels to outlet side channels was found both in porous ribs and the flat GDL.

From these results, it is found that the forced convection derived from the interdigitated flow-channel design concentrated around the end of inlet side channels. This result indicates that almost all the gas supplied from the cell inlet goes through straight channels and runs into the end of inlet channels, resulting in getting into the flat GDL by causing the forced convection locally. This simulation does not incorporate turbulence caused by friction on the channel walls. The pressure drop of supplied gas calculated by this simulation with conditions of 2.0 NL min^{-1} gas flow-rate and 0 kPa outlet pressure was

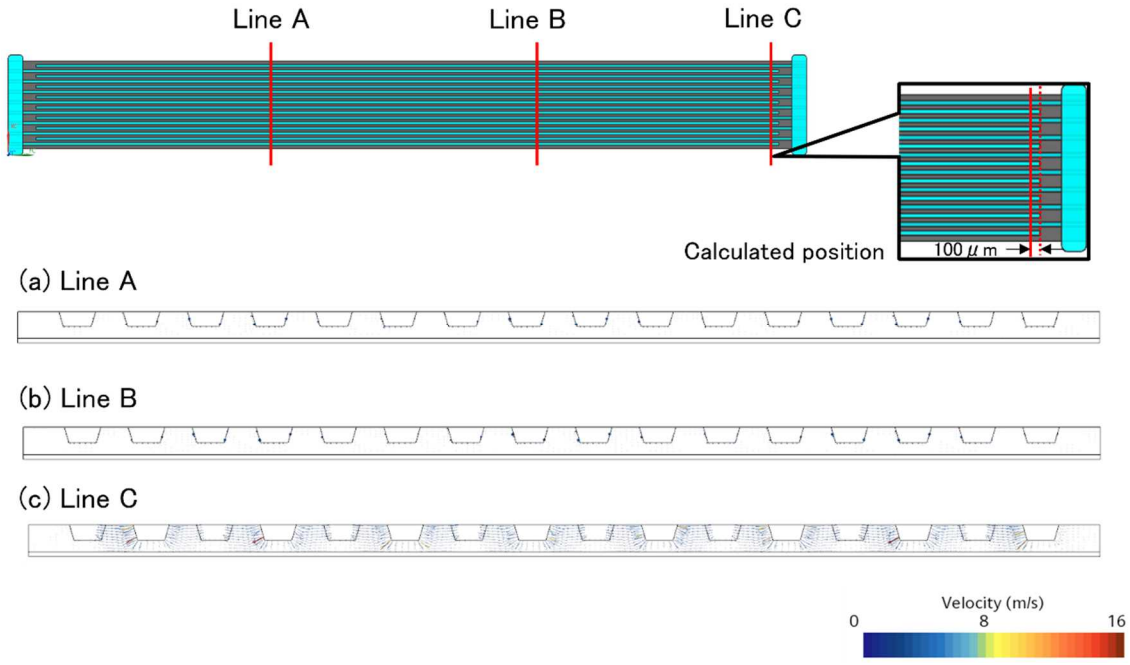

Figure 4-6 Cross section view of gas-flow vector distributions in model 1. Cross sections are positioned in upper side of gas flow (Line A), down side of gas flow (Line B) and at the end of inlet side channel (Line C). The color and the length of gas-flow vectors indicates the velocity of each vector.

48.1 kPa, while measured pressure drop by the experiment carried out in Chapter 4-2 with the same conditions was 100 to 110 kPa. In the case of actual flow channels, turbulence in flow channels is expected to occur and a part of supplied gas may pass through to the outlet side channel, similar to the partially narrowed channel employed in second-generation MIRAI by Toyota Motor Corporation.[9] In any case, the forced convection is considered to occur unevenly at the end of inlet channels. As a result, as shown in the experimental results in Chapter 4-2, it is reasonable to conclude that the contribution to improving performance stability due to the combination of the forced convection and effects by porous ribs discussed in Chapter 2 and 3 decreases relatively as the active area of the cell increases.

To improve contributions by interdigitated flow-channel and porous ribs in larger cells, as M. Nasu et al. applied in their experimental cells,[7] the split design of interdigitated channels along the gas flow direction to several sections is considered to be effective because this design increases the number of spot where the forced convection occurs intensively. Figure 4-7 shows gas-flow distributions on top view of cell active area in models with the variation of segment from 1 to 3. It was commonly found in these results that the forced convection occurs unevenly at the end of inlet channels, and the number of the spot where the forced convection occurs increases depending on the number of the segment. From these simulations, pressure drops of gas flow in conditions with 2.0 NL min^{-1} gas flow rate and 0 kPa outlet pressure were calculated as 48.1 kPa in 1 segment model, 54.4 kPa in 2 segments model and 60.9 kPa in 3 segments model. The pressure drops increased about 6 kPa when a segment increased, while the main part of pressure drops was due to the gas flow resistance during passing through straight flow channels. In other words, it is possible to further increase the number of segments with mitigating the pressure drop increase by reducing the pressure drop during the gas passing through straight channels, for example by extending the cross-section area of channels, resulting in improving performances in larger active-area cells.

4-5. Conclusions

In Chapter 2, the new design for the interdigitated gas flow channels based on the use of a flat, solid separator and a porous GDL with channels formed on its surface was

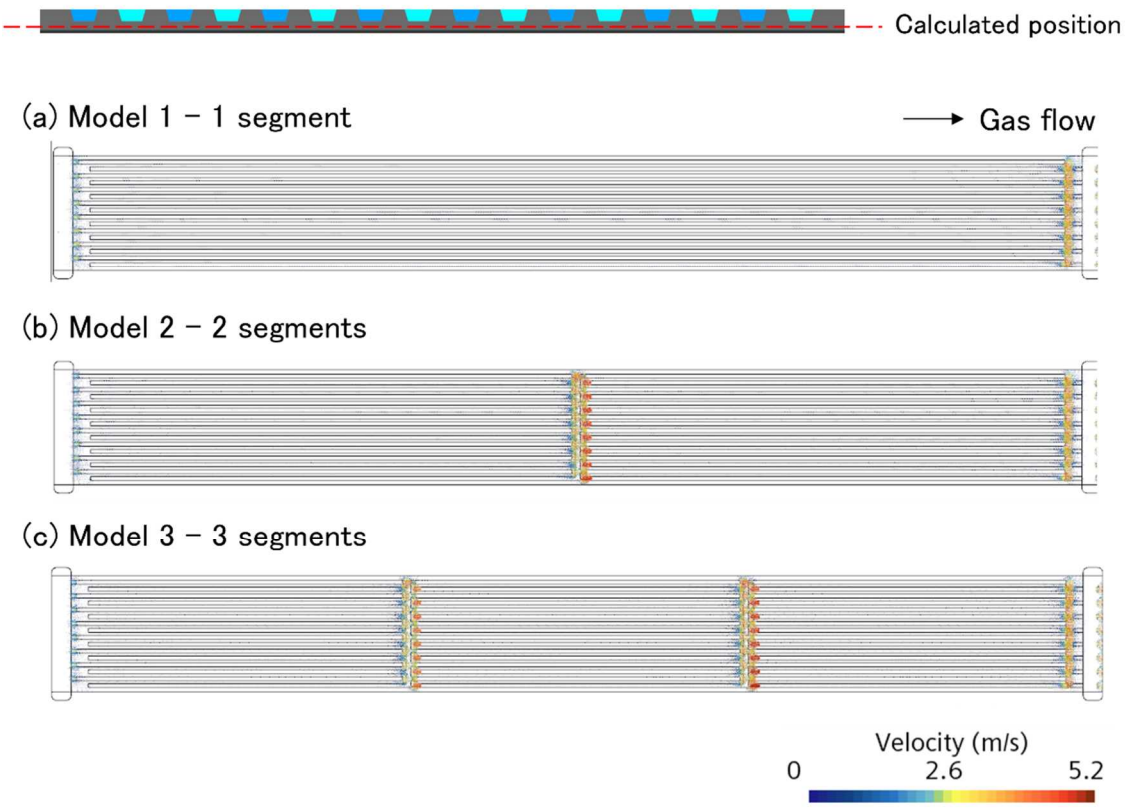

Figure 4-7 Top view of cell active area with gas-flow vector distribution in (a) model 1 of 1 segment, (b) model 2 of 2 segment and (c) model 3 of 3 segment with interdigitated flow-channels. The color and the length of gas-flow vectors indicates the velocity of each vector. Upper picture shows the calculated position of the gas flow which is located in the middle of the GDL substrate height.

fabricated and incorporated into single cells. Both the performance and performance stability for this new design cell were found to improve under conditions with excess water compared to those of a conventional interdigitated cell with solid ribs. In addition, this newly designed interdigitated cell showed higher performance under conditions with a low-humidity gas supply than that for the conventional interdigitated cell.

In this chapter, to validate whether these advantages on performance stability are repeated in larger size cells, cells with 1.0 × 10 cm active area were designed and constructed by extending 1.0 × 1.0 cm cells the length of active area along the direction of gas flow. Experiments of polarization and the characteristics under the relative humidity change were carried out and compared in cells to compare the performance and the performance stability between four channel design including flow-channel shape of interdigitated and parallel, and rib materials of porous state and solid state, as well to

compare these results with experimental results obtained in 1.0 × 1.0 cm. From experimental results, I founded two notable advantages on the cell with interdigitated flow-channel on the GDL: one is the higher performance in polarization than conventional cells which is considered to be contributed by the larger variations of humidification conditions in larger cell size; and the cell performance stability under lower humidification conditions was repeated. However, advantages of the newly designed cell on the performance and the performance stability became smaller compared with the case of 1.0 × 1.0 cm cells. The weakened advantage of interdigitated flow-channels on the GDL is considered to be caused by the decreased ratio of the area where the forced convection and the short pass of gases through the porous ribs are available to the total cell area.

To validate the suggestion above, numerical simulations of CFD were carried out to visualize the gas flow distribution in interdigitated cells with porous ribs. As a result of simulations, the forced convection was found to unevenly occur around the end of inlet side channels. In addition, to enhance the benefit of the interdigitated flow-channel with porous ribs on the performance stability in cells with larger active area, it was found to be effective to split the interdigitated channels to segments along the gas flow direction and increase the number of segments which increase the number of spots where the forced convection intensively occurs. The increase of the segment number also increases the pressure drop of the gas flow, but the increase of the total pressure drop in the cell can be mitigated by decreasing the pressure drop during the gas passing through straight flow channels, for example, by extending the cross-section area of channels.

4-6. References

1. T. V. Nguyen, A Gas Distributor Design for Proton-Exchange-Membrane Fuel Cells, *Journal of Electrochemical Society*, Vol. 143, No.5 (1996)
2. D. L. Wood, III, Jung S. Yi. and T. V. Nguyen, Effect of direct liquid water injection and interdigitated flow field on the performance of proton exchange membrane fuel cells, *Electrochimica Acta*, Vol. 43, No. 24, 3795 (1998)
3. A. D. Le and B. Zhou, A generalized numerical model for liquid water in a proton exchange membrane fuel cell with interdigitated design, *Journal of Power Sources*, 193 (2009), 665-683

4. M. Watanabe, H. Yanai and M. Nasu, Development and Analysis of an Innovative Flat-Metal Separator Integrating the GDL with Gas-Flow Channels as PEFC Components, *Journal of The Electrochemical Society*, 166, 3210 (2019)
5. P. Oberholzer and P. Boillat, Local Characterization of PEFCs by Differential Cells: Systematic Variations of Current and Asymmetric Relative Humidity, *Journal of The Electrochemical Society*, 161 1 (2013)
6. H. Meng and CY. Wang, Large-scale simulation of polymer electrolyte fuel cells by parallel computing, *Chemical Engineering Science*, 59 16 (2004) 3331-3343
7. M. Nasu, H. Yanai, N. Hirayama, H. Adachi, Y. Kakizawa, Y. Shirase, H. Nishiyama, T. Kawamoto, J. Inukai, T. Shinohara, H. Hayashida and M. Watanabe, Neutron imaging of generated water inside polymer electrolyte fuel cell using newly-developed gas diffusion layer with gas flow channels during power generation, *Journal of Power Sources*, 530 (2022), 231-251
8. W. Vielstich, H. A. Gasteiger, A. Lamm, Handbook of fuel cells fundamentals, technology and applications, Fuel cell technology and applications, *John Wiley & Sons Ltd.*, 3 (2003) 597
9. Y. Ma, H. Gyoten, M. Kageyama and M. Kawase, Effects of Partially Narrowed Flow Channel on Performance of Polymer Electrolyte Fuel Cell, *The Electrochemical Society Transactions*, Vol. 109, No. 9 (2022)

Chapter 5 General Conclusions and Future Prospects

5-1. General Conclusions

Fuel cells are recently recognized as next generation power sources because of high energy efficiency and zero CO_x and NO_x emissions.[1] Fuel cell vehicles (FCVs) have been developed by many researchers and commercial FCV have achieved equivalent driving ranges to conventional inner combustion engine vehicles.[2] However, there are still challenges for FCVs to achieve other metrics that would be competitive with those for ICVs, including further improvements in power density and durability, as well as cost reduction. To improve the power density of fuel cells, it is important to decrease the diffusion overvoltage at high current density which is generally caused by the water blockage in gas flow channels including gas diffusion layer (GDL).[3] To deal with this issue and improve cell performances, many researchers have been developed various GDL and flow-channel designs,[4] but the prospect to achieve the target is not clear yet because of difficulties in simultaneously achieving improved gas diffusion especially under the ribs, mechanical stability and cost reduction. Interdigitated flow-channels has a possibility to improve the gas diffusion under the ribs because of the forced convection of the supplied gas in the GDL which enhance mass transport to the catalyst layer.[5] However, interdigitated channels have critical issues on performance decrease under conditions with existence of excess water and dry gas supply.[6] M. Watanabe et al. proposed a new gas flow design, which have interdigitated channels formed on the GDL which are conventionally formed on the separator.[7,8] This newly designed cell showed higher performances compared with conventional design cells. I focused on the possibility of this newly designed cell to overcome the critical issue of conventional interdigitated cells and have a prospect to achieve the future target of the cell performance. In this study, I focused on the feasibility study of the newly designed cell to resolve issues of conventional interdigitated cells, then, focused on revealing the mechanism of higher performance stability of the new cell acquired from experimental result.

In Chapter 2, two sizes of experimental cells with 3.0 × 9.7 cm and 1.0 × 1.0 cm active area were constructed and operated under various conditions. Cells with 3.0 × 9.7 cm size were tested to investigate the performance stability against air flow rate variations.

Experimental results showed that the newly designed cell exhibited higher performance in conditions with excess water existence than the conventional cell. Cells with 1.0 × 1.0 cm size which is simulated to extract the partially from the full-size cell were tested to investigate the performance stability in more detailed conditions including oxygen percentage, air flow rate and relative humidity. From the comparison of these experimental results, I found notable performance stability of the newly designed cell under both high and low humidification conditions. I suggested the mechanism to achieve higher performance stability in newly designed cell that the existence of porous ribs on the GDL effectively manages distributions of liquid water, temperature and gas flow under high and low humidification conditions.

In Chapter 3, the mechanism of higher performance stability in newly designed cell suggested in Chapter 2 was clarified by multiple analysis method. Since it is difficult to visualize all the phenomenon in the cell during operating, I suggested the combination of experimental analysis of X-ray imaging and numerical simulations. Water distribution in the GDL was visualized by X-ray imaging during cell operation, and the change of water distribution during the humidity change from 120% to 40% RH was successfully observed in new and conventional cells and compared. Temperature and gas flow distributions in the GDL were calculated during cell operating simulations by computational fluid dynamics with electrochemical solutions. From these results, the suggested mechanism of the newly designed cell in Chapter 2 was found to be valid. Under high humidification conditions, porous ribs contain excess water in the GDL and increase the GDL temperature around the GDL/MEA (membrane electrode assembly) interface, both contribute to alleviate the blockage of oxygen diffusion to the catalyst layer. Under low humidification conditions, contained water in porous ribs diffuses to the flat area of the GDL to delay the dry out of MEA, then vacant pores in the ribs where water disappeared enable a portion of supplied gas from inlet channel to pass through without diffuse to the flat GDL, resulting in alleviating the dry out of MEA.

In Chapter 4, to investigate whether advantages of the newly designed cell with interdigitated flow-channels on the GDL on performance stability are repeated in larger size cells, I designed and constructed cells with 1.0 × 10 cm active area by extending 1.0 × 1.0 cm cells the length of active area along the direction of gas flow. Experiments of polarization curve and cell operation under variations of the relative humidity change

were carried out and compared in new and conventional interdigitated cells. From experimental results, the advantage of interdigitated flow-channels against parallel flow-channel on oxygen diffusion efficiency repeated in 1.0 × 10 cm cells, but the contribution to the cell performance was weakened compared with that in 1.0 × 1.0 cm cells. Also, the advantage of newly designed cell against the conventional interdigitated cell of the performance stability under dry gas supply was repeated in 1.0 × 10 cm cells, but the contribution to the cell performance was weakened compared with that in 1.0 × 1.0 cm cells. From simulation results of the gas flow distribution in the GDL, these weakened advantages were considered to be caused by the uneven distribution of the forced convection which concentrated around the end of inlet flow channels. Simulation results also indicated that the modification of the interdigitated flow-channel by splitting to several segments along the gas flow direction can increase the spot the forced convection occurs.

As the summary of this study, I focused on the possibility of the newly designed cell with interdigitated channels on the GDL that the existence of porous ribs to resolve critical issued on conventional cells with interdigitated channels on the separator, furthermore, to make a breakthrough on the GDL and the flow-channel design toward the future target for cell performance. To verify advantages of newly designed cell on performances in detail, I suggested and tried the combination of cell operation in variations of conditions including oxygen percentage, air flow rate and relative humidity, resulting in founding the new prospect of newly designed cell to mitigate the conventional issues on interdigitated cells. By focusing on the existence of porous ribs in the newly designed cell, I proposed the new mechanism to improve the performance stability under high and low humidification conditions. To validate the proposed mechanism, I suggested and tried the combination of experimental analysis of X-ray imaging and numerical simulations to clarify distribution of water, temperature and gas flow in operating cells, resulting in successfully validate the proposed mechanism.

5-2. Future Prospects

The newly designed flow channel with interdigitated flow-channel on the GDL is considered to have three significant advantages on the application for vehicles below:

1) Cell performances improvement by enhanced gas diffusion without employing complexed flow-channel design such as 3D fine-mesh which causes the decrease of net FC system power by high-power compressor, and substrate-free GDL which have a lower mechanical strength is expected. Furthermore, the simple design of the separator without flow-channel enables to decrease the cell thickness, resulting in improvement of power density of cells per volume.
2) The cell cost down by eliminating high-cost processes on the separator and the GDL fabrication which are the multi-press forming of the separator and high temperature treatment of the GDL substrate.

To apply this new design of interdigitated flow-channel on the GDL to the commercial FC systems for FCVs, there still remains challenges as below:

1) Modification of the flow-channel design to increase the area the forced convection occurs in the flat GDL, such as split the interdigitated flow-channels to segments with keeping the pressure drop under the proper level, are necessary.
2) Further studies such as on the productivity and cost study of full-size GDL, durability of the GDL, performance feasibility with full-size FC cell, are required.

Although the existence of these remaining challenges, I believe that this research found the new possibility of the interdigitated flow channel design, as well as propose the innovative cell design to overcome issues on conventional and currently developed designs, resulting in helping on accelerating the development of fuel cells toward the achievement of the future targets in fuel cell vehicles and practical application.

5-3. Referencees

1. H. Fayaz, R. Saidur, N. Razali, F. S. Anuar, A. R. Saleman, M. R. Islam, An overview of hydrogen as a vehicle fuel, *Renewable and Sustainable Energy Review*, Vol. 16, Issue 8 (2012) 5511-5528
2. N. Qin, A. Raissi and P. Brooker, Analysis of Fuel Cell Vehicle Development, Report by *Electric Vehicle Transportation Center*, (2014) https://www.fsec.ucf.edu/en/publications/pdf/FSEC-CR-1987-14.pdf
3. H. Li, Y. Tang, Z. Wang, Z. Shi, S. Wu, D. Song, J. Zhang, K. Fatih, J. Zhang, H. Wang, Z. Liu, R. Abouatallah and A. Mazza, A review of water flooding issues in the proton exchange membrane fuel cell, *Journal of Power Sources*, Vol. 178, Issue 1

(2008) 103-117

4. H. Liu, P. Li, D. Juarez-Robles, K. Wang and A Hernandez-Guerrero, Experimental study and comparison of various designs of gas flow fields to PEM fuel cells and cell stack performance, *Frontiers in Energy Research*, Vol. 2 (2014)
5. T. V. Nguyen, A Gas Distributor Design for Proton-Exchange-Membrane Fuel Cells, *Journal of Electrochemical Society*, Vol. 143, No.5 (1996)
6. A. D. Le, B. Zhou, A generalized numerical model for liquid water in a proton exchange membrane fuel cell with interdigitated design, *Journal of Power Sources*, Vol. 193, Issue 2 (2009), 665-683
7. M. Watanabe, H. Yanai and M. Nasu, Development and Analysis of an Innovative Flat-Metal Separator Integrating the GDL with Gas-Flow Channels as PEFC Components, *Journal of The Electrochemical Society*, Vol. 166, No. 7 (2019) F3210
8. M. Nasu, H. Yanai, N. Hirayama, H. Adachi, Y. Kakizawa, Y. Shirase, H. Nishiyama, T. Kawamoto, J. Inukai, T. Shinohara, H. Hayashida and M. Watanabe, Neutron imaging of generated water inside polymer electrolyte fuel cell using newly-developed gas diffusion layer with gas flow channels during power generation, *Journal of Power Sources*, Vol. 530, (2022) 231251

List of publications

1. “Improvement of PEFC Performance Stability under High and Low Humidification Conditions by Use of a Gas Diffusion Layer with Interdigitated Gas Flow Channels”
   Tatsuya Inoue, Daiki Sakai, Kazuhiro Hirota, Koichi Sano, Mitsunori Nasu, Hiroshi Yanai, Masahiro Watanabe, Akihiro Iiyama and Makoto Uchida
   Journal of Electrochemical Society, Vol. 169 (2022), 114504

2. “Analysis of performance stability under conditions of high & low humidity of polymer electrolyte fuel cells with interdigitated gas flow channels formed on a gas diffusion layer: An X-ray imaging and modeling study”
   Tatsuya Inoue, Daiki Sakai, Naoki Hirayama, Mitsunori Nasu, Takahiro Suzuki, Shoji Tsushima, Junji Inukai, Donald Alexander Tryk, Masahiro Watanabe, Akihiro Iiyama and Makoto Uchida
   Journal of Power Sources, Vol. 585 (2023), 233623

Awards

1. EVTeC2023 Young Investigators Award
   The 6th International Electric Vehicle Technology Conference, May 22-24 (2023)
   "A Study on the Performance Stability and Water Management of a PEFC with Interdigitated Gas Flow Channels formed on a Gas Diffusion Layer"
   Tatsuya Inoue, Daiki Sakai, Kazuhiro Hirota, Koichi Sano, Naoki Hirayama, Mitsunori Nasu, Takahiro Suzuki, Shoji Tsushima, Junji Inukai, Masahiro Watanabe, Akihiro Iiyama and Makoto Uchida

Acknowledgment

The present thesis is the summary of work carried out at Suzuki Motor Corporation, Enomoto Co. ltd., Tsushima laboratory in Osaka University, Hydrogen and Fuel Cell Nanomaterials Center and Interdisciplinary Graduate School of Medicine and Engineering in University of Yamanashi from 2019 to 2023.

This research was partially supported by the “Fuel Cells–Yamanashi Frontier for Innovation and Ecosystem (FCyFINE)” program (2017–2021); it was also supported by the Ministry of Education, Culture, Sports, Science and Technology, Japan, and was partially supported by funds for the “Electrolytes, catalysts and catalyst layers with extraordinary efficiency, power and durability for PEFCs to 2030” (ECCEED-GDL) project from the New Energy and Industrial Technology Development Organization (NEDO).

I would like to express my greatest gratitude to Professor Makoto Uchida of University of Yamanashi for providing me this precious study opportunity as a Ph. D. I am grateful for his continued guidance, discussions, valuable suggestions, and warm supports and encouragement through my study.

I also would like to express my sincere gratitude to Professor Masahiro Watanabe, Professor Akihiro Iiyama, Professor Junji Inukai, Professor Katsuyoshi Kakinuma and Associate Professor Koji Toriyama for valuable suggestions, discussions, and guidance through my research. I also would like to express my gratitude to Professor Donald Alexander Tryk for his invaluable suggestions and comments.

I also would like to express my sincere gratitude to Professor Shoji Tsushima and Associate Professor Takahiro Suzuki of Osaka University for carrying out valuable results on X-ray imaging, valuable suggestions, discussions and comments.

I also would like to express my sincere gratitude to Mr. Mitsunori Nasu and all collaborators in Enomoto Co. Ltd. for providing innovative GDL samples, valuable suggestions, discussions and comments.

I would like to express my sincere gratitude to Mr. Takahiro Asakawa for FIB measurement.

I would like to express my sincere gratitude to Mr. Daiki Sakai for carrying out valuable results by numerical simulations, valuable suggestions, discussions and comments. I also would like to express my sincere gratitude to all of my colleagues at Suzuki Motor Corporation for supports including valuable suggestions, discussions and guidance through my research and work.